

Ice-sheet sensitivity to Earth's surface: an assessment of landscape records

Marion McKenzie
Charlottesville, Virginia

B.S. Environmental Studies, Gettysburg College, 2019

A Dissertation presented to the Graduate Faculty
Of the University of Virginia in Candidacy for the Degree of
Doctor of Philosophy

Department of Environmental Sciences

University of Virginia
May 2023



Committee Members:
Professor Lauren M. Simkins
Professor Ajay B. Limaye
Professor Scott Doney
Professor Howard Epstein
Professor Regina DeWitt
Professor Matthew Jull

Abstract.

Understanding drivers of glacier stability is important to consider for future contributions to global sea-level rise. The underlying terrain on which ice sheets, continental-scale amalgamations of glaciers, rest have the ability to modulate ice flow and rates of ice sheet growth and decay, but the influence of subglacial bed conditions is far from straightforward. Difficulties in accessing and studying contemporary subglacial environments leaves gaps in knowledge on the sensitivity of ice sheet behavior across time and space. Deglaciated landscapes that were once covered by ice sheets preserve records in the form of landforms and sediments and provide broad spatiotemporal perspectives on ice-sheet response to subglacial bed conditions. Through the development of a semi-automated mapping tool, 11,628 sedimentary and bedrock streamlined subglacial bedforms, serving as proxies for subglacial processes and ice flow, were mapped across nine sites of varying lithologic and topographic setting in the deglaciated Northern Hemisphere (Chapter 2; McKenzie et al., 2022). A minimum bedform length-width ratio and similarities in bedform metric distribution across bed lithology and topography indicate streamlined bedform synthesis is supported across all bed conditions. High ice-flow velocities based on highly elongate streamlined features occur within confined valley settings. Unconfined topography across sedimentary beds encourage consistency in ice-flow velocity and spatially uniform and organized interactions at the ice-bed interface. Elevated bed topography, or “bumps”, have the potential to slow ice flow or, conversely, increase ice-flow speed through strain heating and subglacial meltwater production. Streamlined subglacial bedforms on and proximal to isolated bumps of variable size across the deglaciated landscape of the Cordilleran Ice Sheet (CIS) of Washington state were assessed to characterize differences in ice flow and sedimentary processes due to the variable topography (Chapter 3; McKenzie et al., *preprint*). Ice flow organization and sedimentary processes (e.g., deformation, erosion, and deposition) are significantly disrupted by bumps greater than 4.5 km³. Landform-building sedimentary processes are most mature downstream of bumps, likely due to increased availability and production of subglacial sediment and meltwater. Additionally, due to direct CIS coverage and high rates of glacial isostatic adjustment (GIA), sediment archives in the Puget Lowland of Washington state record spatial and temporal shifts landscape evolution and ice behavior. As identified through combined sedimentological and geochronological analyses, the late-stage CIS experienced step-wise retreat within a marine environment about 12,000 years B.P., placing glacial ice in the region for about 3,000 years longer than previously thought (Chapter 4; McKenzie et al., *in prep*). Additional rapid rates of vertical landscape evolution support a millennial-long stand still of marine-terminating ice, followed by continued retreat of ice in a subaerial environment. Overall, these works provide novel insight to the role of subglacial bed conditions in influencing ice-sheet behavior from landform and sediment records of deglaciated landscapes in the Northern Hemisphere. With this dissertation, I contribute to process-based knowledge of subglacial processes, landform generation, and controls on ice flow and retreat that are useful for understanding both marine- and terrestrial-based components of the contemporary Antarctic and Greenland ice sheets.

Table of contents

<i>Abstract</i>	2
<i>Table of contents</i>	3
<i>List of tables</i>	5
<i>List of figures</i>	6
<i>Acknowledgements</i>	10
<i>Chapter 1: Introduction</i>	11
<i>Chapter 2: Streamlined subglacial bedform sensitivity to bed characteristics across the deglaciated Northern Hemisphere</i>	15
2.1 Introduction	15
2.2 Methodology	17
2.3 Results	19
2.3.1 Streamlined subglacial bedform identification	19
2.3.2 Bedform morphology	20
2.3.3 Bedform parallel conformity and distribution	21
2.3.4 Bedform morphometric correlations with bed lithology and topography	21
2.4 Discussion	21
2.4.1 Success of semi-automatic mapping streamlined bedforms in deglaciated landscapes	22
2.4.2 Bedform properties across the deglaciated Northern Hemisphere	23
2.4.3 Bedform morphology in relation to bed setting	24
2.5 Conclusions	27
<i>Chapter 3: Differential impact of isolated topographic bumps on glacial ice flow and subglacial processes</i>	39
3.1 Introduction	39
3.1.1 Site Characteristics	39
3.2 Methodology	40
3.2.1 Topographic “Bump” Classification	40
3.2.2 Streamlined subglacial bedform identification	40
3.3 Results and Discussion	41
<i>Chapter 4: Outcrop perspectives on spatial and temporal effects of topography on the marine-terminating Puget Lobe of the Cordilleran Ice Sheet</i>	47
4.1 Introduction	47
4.2 Methodology	48
4.2.1 Sedimentology and Stratigraphy	48
4.2.2 Accelerator Mass Spectrometry Radiocarbon Analysis	49

4.2.3 Optically Stimulated Luminescence	50
4.3 Results	53
4.3.1 Double Bluff	53
4.3.2 Fort Casey	53
4.3.3 Penn Cove	54
4.3.4 West Beach	55
4.3.5 Rocky Point, Cliffside	55
4.4 Discussion and Interpretation	56
4.4.1 Facies interpretation	56
4.4.2 Pre-LGM landscape evolution	57
4.4.3 LGM glacial advance	57
4.4.4 Deglaciation	57
4.4.5 Post-LGM landscape evolution	58
4.5 Conclusions	59
<i>Chapter 5: Concluding Remarks</i>	78
5.1 Summary	78
5.2 Future Directions	79
<i>Appendix A2</i>	81
<i>Appendix A4</i>	84
<i>References</i>	86

List of tables.

Table 2.1. Site descriptions and data information for nine deglaciaded sites across the Northern Hemisphere.

Table 2.2. Bedform data by site, including spatial statistics and bedform metrics.

Table 4.1. Site and sample collection information.

Table 4.2. Radiocarbon sample descriptions and data. Gray rows indicate known-age shells dated to develop MRC.

Table 4.3. OSL measurement sequence.

Table 4.4. Dose measurements, dose rate, and OSL age data. Final sample ages are bolded.

List of figures.

Figure 2.1. Study sites: (A) Puget Lowland, Washington, USA; (B) northwestern Pennsylvania, USA; (C) Chautauqua, NY, USA; (D) M'Clintock Channel, Canada; (E) Prince of Wales Island, Canada; (F) Nunavut, Canada; (G) Bárðardalur, Iceland; (H) northern Norway; (I) northern Sweden.

Figure 2.2. Streamlined subglacial bedforms (gray polygons) at sites (A) Puget Lowland, Washington, USA; (B) northwestern Pennsylvania, USA; (C) Chautauqua, NY USA; (D) M'Clintock Channel, Canada; (E) Prince of Wales Island, Canada; (F) Nunavut, Canada; (G) Bárðardalur, Iceland; (H) northern Norway; (I) northern Sweden. Outlined inset boxes are locations shown in Figure 2.8.

Figure 2.3. Correlation matrix of all 11.628 bedform features, conducted using linear Pearson correlation. Categorical variables were assigned arbitrary values for comparison statistics.

Figure 2.4. Bedform length and width metrics plotted by site: (A) convex hull area of all bedform length and width metrics and (B) scatterplot of the same data as (A); gray areas indicate regions where bedforms are not observed. (C) Convex hull area of all bedform elongation ratio and elevation range metrics; (D) scatterplot of the same data as (C).

Figure 2.5. Frequency (n) of bedform elongation ratios. (A) Composite histograms of elongation frequencies for each site. (B) Individual site elongation frequencies. Site bins were determined using the “nbins” function in MATLAB, assigning each site 15 bins in order to make frequencies comparable.

Figure 2.6. (A) Distribution of bedform surface relief range and (B) distribution of bedform elongation ratios by site characterized by topography and bed substrate. MATLAB code for violin plot visualization sourced from Hoffmann (2015).

Figure 2.7. Cardinal orientations of mapped bedforms. (A) Puget Lowland, Washington, USA; (B) northwestern Pennsylvania, USA; (C) Chautauqua, NY, USA; (D) M'Clintock Channel, Canada; (E) Prince of Wales Island, Canada; (F) Nunavut, Canada; (G) Bárðardalur, Iceland; (H) northern Norway; (I) northern Sweden.

Figure 2.8. Representative bedform elongation ratios at (A) Puget Lowland, Washington, USA; (B) northwestern Pennsylvania, USA; (C) Chautauqua, NY, USA; (D) M'Clintock Channel, Canada; (E) Prince of Wales Island, Canada; (F) Nunavut, Canada; (G) Bárðardalur, Iceland; (H) northern Norway; (I) northern Sweden. Black arrows indicate ice flow direction.

Figure A2.1. Examples of topographically unconstrained topography (A) in northwestern Pennsylvania (Site B) and topographically constrained topography (B) in Bárðardalur, Iceland (Site G). Gray areas in (B) indicate areas of higher topography and generally follow the valley wall boundary.

Figure A2.2. Examples of TPI applied to sites of each bed lithology, orange indicates volcanic bedrock at Site G, blue outline indicates sedimentary rock at Site C, green outline indicates sedimentary bedrock at Site F. Images 1b, 2b, and 3b show TPI analysis before manual sorting; 1c, 2c, and 3c show final bedform mapping with both TPI and manual methods. Figure 2.4A is the Site F DEM before mapping, the orange circle in 4b contains bedforms incorrectly identified by TPI due to under-identification, the blue circle in 4b contains one example of a bedform correctly identified by TPI.

Figure A2.3. Streamlined subglacial bedforms identified by the TPI identification tool (gray polygon) and manually identified (blue polygons) at sites (A) Puget Lowland, Washington, USA; (B) northwestern Pennsylvania, USA; (C) Chautauqua, NY, USA; (D) M'Clintock Channel, Canada; (E) Prince of Wales Island, Canada; (F) Nunavut, Canada; (G) Bárðardalur, Iceland; (H) northern Norway; (I) northern Sweden.

Figure 3.1. A) Site overview across the Puget Lowland with inset reference of CIS glaciation (14 kya; Ehlers et al., 2010). Site maps for i) the Blue Hills, ii) Devils Mountain, iii) Cougar Mountain, iv) Dow Mountain, v) big Skidder Mountain, vi) Fidalgo Island, vii) San Juan Island, viii) the Black Hills, and ix) Lopez Island. Streamlined subglacial bedforms are mapped upstream (gray polygons), on top of (black polygons), and downstream (blue polygons) of bed bumps (small white outlines) within larger site regions (large white outlines). B) Relative volume and surface area of bed bump sites.

Figure 3.2. Scatterplots of the log of bedform elongation ratio and surface relief in meters. The ellipses are 1σ (68%) confidence levels for multivariate t-distributions for all bedforms ($n=3,273$). Sites are listed in the legend from largest surface area ((i) Blue Hills) to smallest surface area ((ix) Lopez Island).

Figure 3.3. Box plots of A) bedform elongation data at each site with populations characterized upstream of, on top of, and downstream of bumps and B) surface relief data at each site with populations characterized upstream of, on top of, and downstream of bumps. Statistically significant differences between groups are indicated by asterisks. Multiple asterisks indicate a separate population with significant differences, independent from other groups of statistical significance.

Figure 3.4. A) Density curves of bedform elongation upstream, on top of, and downstream of nine bumps. Density curves with color are less than 4 square kilometers, all other sites are shown in gray. B) Density curves of bedform surface relief in meters upstream, on top of, and downstream of nine bumps. Density curves with color are less than 4 square kilometers in surface area, all other sites are shown in gray. C) Cardinal orientations of streamlined bedforms upstream, on top of, and downstream of nine bumps.

Figure 4.1. Adapted from Fig. 26 in Eyles et al., 2018: “Size and basal topography of the present-day Greenland Ice Sheet (GrIS; Rippin, 2013; Morlighem et al., 2014) compared to the Late Wisconsin Cordilleran Ice Sheet (CIS). Both ice sheets of a comparatively low relief central core zone are flanked by regions of high mountainous relief. Both ice sheets possess a presence of thick subglacial sediments.” Outlined boxes indicate outlet glaciers of similar topographic

setting to highlight the applicability of applying glacial processes in the Puget Lowland to modern systems.

Figure 4.2. Outcrop sites on Whidbey Island (white outline) in the northern Puget Lowland, Washington state.

Figure 4.3. The outcrop site at (a) West Beach shows evidence for final ice retreat below sea level due to the presence of marine shells stratigraphically above the last diamicton unit. Outcrops at (b) Fort Casey indicated ice retreat in a subaerial environment due to the lack of glaciomarine materials, indicating land emergence before ice retreat. The bedrock exposure at (c) Rocky Point may have had some topographic influence on ice flow. (d) Penn Cove outcrop cross-bedded sand below a massive diamicton sampled for OSL to constrain LGM ice re-advance into the region. (e) Woody debris in laminated silty-clay at West Beach, collected for radiocarbon dating.

Figure 4.4. OSL calculation workflow.

Figure 4.5. Double Bluff A) stratigraphic column with radiocarbon and OSL data and grain size data. Black dots indicate changes to site collection of samples. B) Trace element and magnetic susceptibility data for this site. C) Example coastal bluffs at Double Bluff taken from the Washington state Shoreline Viewer with inset regional map.

Figure 4.6. Fort Casey Site 1 A) stratigraphic column with radiocarbon and OSL data and grain size data. B) Trace element and magnetic susceptibility data for this site. C) Example coastal bluffs at Fort Casey Site 1 taken by M. McKenzie with inset regional map.

Figure 4.7. Fort Casey Site 2 A) stratigraphic column with radiocarbon and OSL data and grain size data. B) Trace element and magnetic susceptibility data for this site. C) Example coastal bluffs at Fort Casey Site 2 taken from the Washington state Shoreline Viewer with inset regional map.

Figure 4.8. Penn Cove A) stratigraphic column with radiocarbon and OSL data and grain size data. Black dots indicate changes to site collection of samples. B) Trace element and magnetic susceptibility data for this site. C) Example coastal bluffs at Penn Cove taken from the Washington state Shoreline Viewer with inset regional map.

Figure 4.9. West Beach Site 1 A) stratigraphic column with radiocarbon and OSL data and grain size data. B) Trace element and magnetic susceptibility data for this site. C) Example coastal bluffs at West Beach Site 1 taken by M. McKenzie with inset regional map.

Figure 4.10. West Beach Site 2 A) stratigraphic column with radiocarbon and OSL data and grain size data. Black dots indicate changes to site collection of samples. B) Trace element and magnetic susceptibility data for this site. C) Example coastal bluffs at West Beach Site 2 taken by M. McKenzie with inset regional map.

Figure 4.11. Cliffside A) stratigraphic column with radiocarbon and OSL data and grain size data. Black dots indicate changes to site collection of samples. B) Trace element and magnetic susceptibility data for this site. C) Example coastal bluffs at Cliffside taken from the Washington state Shoreline Viewer with inset regional map.

Figure 4.12. Figure 4 from Demet et al., 2019: “Map of surface slopes of Whidbey Island. Crestline orientations record episodic change in ice flow direction. Inferred GZW crestlines lack outcrop exposure. Outcrop locations are highlighted in red, with West Beach (WB) Fort Casey (FC) and Driftwood (DW) sections labeled.” In addition to the West Beach, Fort Casey, and Driftwood (in this work. Double Bluff) sites being stratigraphically assessed, the Penn Cove stratigraphy was also assessed in this project.

Figure 4.13. Grouping of facies based on depositional time periods across Whidbey Island. Units with asterisks have radiocarbon or OSL dates included in the table on the lower left.

Figure 4.14. Timeline of newly developed geochronologies and implications for overall landscape development and ice movement in the Puget Lowland.

Figure A4.1. A clay lamination seen in Unit 3 of Fort Casey Site 1 and a silt lens seen in Unit 1 of Fort Casey Site 1. This distinction is maintained throughout all site stratigraphic descriptions.

Figure A4.2. Schematic drawing of A) time 1 indicating Puget Lobe advance into subaerial Puget Lowland post landscape emergence (Figure 4.13). B) Indicates time 2 Puget Lobe ice retreat within a marine environment post landscape-submergence and marine-incursion following time 1. Puget Lobe ice retreat in a marine environment only occurred at southernmost sites Double Bluff and Penn Cove (Figure 4.13).

Acknowledgements.

It has been an honor and a privilege to conduct this work under the guidance and mentorship of Dr. Lauren Simkins throughout my time at the University of Virginia. The ways in which she helped me grow as a scientist, teacher, mentor, and collaborator allowed me to accomplish much more than I knew I could. Lauren, thank you for your constant encouragement, patience, and wisdom. I am a better person and professional for having had you as a mentor and role model.

The Ice and Ocean Group at UVA has become one of my biggest supporters and sounding-boards through the many ups and downs of the last four years. Thank you to Alie Lepp and Santi Munévar Garcia for your collaboration, support, advice, and above all, your friendship – I could not have done this without you. One of my favorite parts of graduate school was the opportunity to mentor some incredible undergraduate students. Thank you Medha Prakash, Jacob Slawson, Maya Weiss, Marion Donald, and Renee Hebert for trusting me and learning with me throughout your undergraduate experience. I cannot wait to see the amazing things you do in the future.

To my fellow graduate students that have become family: Madeline Miles, Kayleigh Granville, Angelique Demetillo, Alie Lepp, Mary Stack, and Lauren Brideau – thank you for making Charlottesville feel like home. Friendship with you has added a level of comfort, inspiration, and silliness to my life that made grad school so much more manageable. The constant support in the form of phone calls and visits from my mom, dad, brother, and best friends Liz Rose and Alexi Doak acted to remind me that I could do anything I put my mind to. Thank you to all of the friends and family that helped me get here – it takes a village, and I don't know where I'd be without my very large, very wonderful village.

Thank you to my committee for their support throughout this journey. I am especially grateful for the patient guidance of Dr. Regina DeWitt while navigating the complicated process that is OSL dating. Dr. Sarah Principato has also supported me throughout my undergraduate and now graduate career; I am so grateful for her advice and friendship.

This work was funded by the Chamberlain Endowment, the H.G. Goodell Endowment, and the Exploratory and Moore Awards at the University of Virginia. I thank the Washington Department of Natural Resources, USGS, and the Polar Geospatial Data Center for data used in Chapters 2 and 3 as well as A. Weiss, S. Tagil, and J. Jenness for research that was used to produce the TPI tool. Thank you to Jane Ruggles and Michael Cornish for their support in the development of Chapter 4. The funding and support for the radiocarbon dates presented in Chapter 4 was made possible through the National Ocean Sciences Accelerator Mass Spectrometry (NOSAMS) Graduate Student Internship at Woods Hole Institute and the Burke Institute. Thank you to Dr. Mark Kurz, Dr. Roberta Hansman, Anne Cruz, Mary Lardie Gaylord, and Nan Trowbridge for their hospitality and guidance throughout my internship.

The sites analyzed in Chapters 3 and 4 work are located on land historically cultivated and inhabited by the Skokomish, Suquamish, Squaxin, Stl'pulmsh, Steilacoom, Puyallup, Muckleshoot, and Duwamish peoples. The majority of the effort put into data analysis and dissertation construction was conducted on land cultivated and inhabited by the Monacan Nation. The peoples of these Nations were custodians of the land for time immemorial before forced removal and genocide during colonization. I acknowledge their ongoing stewardship of the lands.

Chapter 1: Introduction

Identifying controls on ice-sheet mass balance and behavior through the use of the paleo-record is imperative for constraining and modeling modern ice sheet changes (Vaughn et al., 2013). Fast-flowing regions of ice sheets (10^2 - 10^3 m a⁻¹) surrounded by slower flowing ice, called ice streams, have the ability to destabilize entire ice-sheet catchments. Ice streams are the primary conveyors of ice discharge into the ocean and are commonly studied due to the preservation of geologic evidence in deglacial landscapes (e.g., Ó Cofaigh et al., 2013; Greenwood et al., 2018; Margold et al., 2015). Ice-flow dynamics are influenced by a number of factors including changes in buttressing by sea ice and floating ice shelves (Fürst et al., 2016) and internally through ice deformation, basal sliding in the presence of meltwater, and basal sediment deformation (Benn and Evans, 2014). In studying glacial systems, the underlying topography and bed lithology are of large interest due to the role these properties play in controlling ice velocity (e.g., Hindmarsh, 2001; Spagnolo et al., 2017; Falcini et al., 2018; Ignéczi et al., 2018; Maier et al., 2019; Greenwood et al., 2021). Therefore, the composition and topographic characteristics of the geologic substrate beneath glacial systems is highly important in determining ice contribution to global sea-level rise. The properties of the underlying terrains (i.e., beds) that support ice streams are of great interest due to the effects different topography and lithology have on ice-flow dynamics (Serrousi et al., 2017; Spagnolo et al., 2017; Falcini et al., 2018; Greenwood et al., 2021). While subglacial properties in part control the presence or absence of ice streaming, the interactions between fast-moving ice and the underlying bed are not well understood. In order to adequately anticipate the factors affecting future ice-sheet contributions to sea level, a better understanding of ice-bed interactions is needed.

While ice-sheet change is influenced by external forcings like atmosphere and ocean warming (Hindmarsh & Le Meur, 2001; Seguinot et al., 2014; Bassis et al., 2017), patterns of ice flow (Clarke et al., 1977; Whillans and van der Veen, 1997; Cuffey & Paterson, 2010) and ice margin position (Weertman, 1974; Clark, 1994; Jamieson et al., 2012; Enderlin et al., 2014) are often linked to properties of the bed, although they can have opposing effects on ice-sheet behavior (De Rydt et al., 2013; Krabbendam et al., 2016; Falcini et al., 2018; Greenwood et al., 2021; McKenzie et al., 2022). In both marine and land-terminating systems, areas with negative relief, such as valleys and troughs, have potential to increase ice streaming due to syphoning and thickening of ice and subsequent increase in basal meltwater production (Hindmarsh, 2001; Eyles et al., 2018; McKenzie et al., 2022). Similarly, positive topographic relief (i.e. pinning points, ridges, and banks) and rough beds can increase basal meltwater and ice streaming through strain heating (McIntyre, 1985; Pohjola and Hedfors, 2003; Winsborrow et al., 2010b; McKenzie et al., *preprint*). In other circumstances, obstacles in the bed can enhance frictional resistance to ice flow and confined topography can enhance lateral drag, leading to slower ice flow and, in marine-terminating systems, potential margin stabilization (Favier et al., 2016; Falcini et al., 2018; Whillans and van der Veen, 1997; McKenzie et al., 2022). While these properties seem consistent in theory, some uncertainties remain regarding size thresholds for bed highs to significantly impact ice flow, as these factors relate to local glacial conditions (De Rydt et al.,

2013; Falcini et al., 2018). Questions about these thresholds have been explored using glacier seismology (Podolskiy and Walter, 2016) and numerical models supported by high resolution geophysical surveys (Greenwood et al., 2018; Sergienko and Wingham, 2019; Alley et al., 2021) but appear to vary between systems. In Chapters 2 and 3, the knowledge gap regarding ice-sheet sensitivity to a wide range of topographic features in the subglacial environment is addressed utilizing deglaciated terrestrial landscapes (McKenzie et al., 2022; McKenzie et al., *preprint*).

Due to the influence of oceans on marine terminating ice-sheet sectors, warming waters or increased sea level around the ice margin may destabilize and cause retreat where ice is thinned or becomes too buoyant and can no longer maintain contact with the bed (Favier et al., 2016; Hindmarsh and Le Meur, 2001). Reverse slope beds, or bed slopes that deepen in elevation inland, also pose a large threat to ice-mass balance of marine terminating systems: once the ice is no longer in contact with the bed, ice moving along reverse slope beds is likely to experience runaway retreat as marginal ice thickness and flux increase and thus thinning occurs leading the buoyancy-driven retreat inland (Weertman, 1974; Jamieson et al., 2012; Robel et al., 2019). Conversely, sediment deposition along the margin of retreating ice systems can contribute to stabilization by providing self-built pinning points for the ice to rest (Batchelor and Dowdeswell, 2015; Simkins et al., 2018; Demet et al., 2019). Glacial isostatic adjustment (GIA), or the redistribution of solid Earth due to ice load changes, is theoretically shown to stabilize marine-terminating margins of the Antarctic Ice Sheet by reducing effective water depth as the seafloor rebounds due to ice loss (Gomez et al., 2012; Whitehouse et al., 2019). This concept is tested empirically in Chapter 4 (McKenzie et al., *in prep*).

While subglacial bed characteristics are essential to understanding controls on ice-sheet behavior in both land- and marine-terminating systems, accessing these environments under modern ice sheets is logistically challenging. However, the study of deglaciated landscapes offer direct access to paleo-subglacial beds and to geologic archives of ice-sheet behavior (Wellner et al., 2001; Ottesen et al., 2008; Eyles & Doughty, 2016; Jones et al., 2020). The work herein focuses primarily on sedimentary material deposited during the Last Glacial Maximum (LGM; ~20,000 years ago) or local LGMs and subsequent deglaciation due to the strong preservation and little reworking of material from this time as compared to sedimentary deposits from earlier glacial periods.

1.1. Landform evidence of controls on ice flow and retreat

Pressure differences at the ice-bed interface drive stress fracturing, or plucking, while interactions between entrained rock material and underlying bed surfaces drive physical erosion, or abrasion, of the underlying bed surface. Together, these processes drive the evolution of glacial landscapes (Linton, 1963). As ice sheets persist on the Earth's surface for several millennia, they are able to erode and redistribute surface materials over large areas through their movement. Glacial landforms created through abrasion and deposition of ice-mobilized materials are proxies for past ice sheet behavior and ice-bed interactions that are difficult to observe

beneath modern ice streams (e.g., Riverman et al., 2019; Principato et al., 2016; Krabbendam et al., 2016; Simkins et al., 2018; Greenwood et al., 2021; McKenzie et al., 2022). Details inferred from these landforms include margin retreat style (i.e. punctuated, slow, fast) and flow direction and relative speed. However, the processes of abrasion, plucking, and deposition of material can vary widely based on the bed substrate, composition, topographic setting, and the overlying ice sheet.

Ice-flow dynamics of extinct glacial systems, assessed using streamlined subglacial bedforms as a proxy for ice speed, direction, and maturity, are explored across regional scales with relation to variable topographic and bed substrates throughout Chapter 2. Then within a single glacial system, to remove confounding local glaciological conditions, Chapter 3 explores the role of regional topographic highs on controlling ice flow speed and direction as well as subglacial erosion and deposition. The sites used in Chapters 2 and 3 exhibit remarkable topographic similarities to margins of the modern Greenland Ice Sheet, supporting that process-based findings from this work can be extrapolated to modern glacial systems (Eyles et al., 2018; MacKie et al., 2020; MacKie et al., 2021).

1.2. Stratigraphic and geochronological assessment of ice behavior: focused case study in the Puget Lowland, Washington state

In addition to quantitative geomorphology, stratigraphic records in previously glaciated regions can provide a highly detailed spatial and temporal record of ice movements across a landscape. Recent advancements in the fields of geochronology, glacial geology, and ice-sheet modeling have been incredibly useful in reconstructing spatial and temporal changes in ice-sheet extent, movement, and demise across many deglaciated landscapes (e.g., Rosenheim et al., 2013; Seguinot et al., 2016; Falcini et al., 2018). One understudied region with well-preserved glacial and interglacial sediments from the LGM is the Puget Lowland in Washington state, glaciated by the southernmost Cordilleran Ice Sheet (CIS) through at least the last 300,000 years.

While the CIS is argued to be the least understood of all Pleistocene ice sheets, its topographic environment is most similar to the terrain beneath the Greenland Ice Sheet (i.e., a basin surrounded by mountainous terrain; Bamber et al., 2013; Eyles et al., 2018). At the time of glaciation, the southernmost lobe of the CIS terminated within the marine environment of the Puget Lowland where dynamics of GIA caused uplift of the marine environment, thought to coincide with periodic ice sheet stability (Simkins et al., 2017; Demet et al., 2019). The Puget Lowland displays similar solid Earth rheology (lithospheric thickness and mantle viscosity) to the Antarctic Peninsula, suggesting viscoelastic responses of solid Earth could have played an important role in stabilizing CIS retreat, similar to modeled and observed contemporary outlet glaciers of the Antarctic Peninsula (Whitehouse et al., 2019; Nield et al., 2014). The well-preserved sediment record of the Puget Lobe, the southernmost portion of the CIS, has been highly interpreted to date, but the lack of detailed stratigraphic assessment in addition to the

unknown marine reservoir correction (MRC) of this region contribute to uncertainties in timing of glacial and deglacial events. These factors have contributed to discrepancies in radiocarbon-dated materials and largely unclassified timing of subaerial emergence. The decimeter-scale stratigraphic assessment and modern approaches to geochronological analysis in the Puget Lowland conducted in Chapter 4 provide novel insight to the spatial and temporal ice dynamics of the Puget Lobe while also addressing the role of subglacial environments in controlling ice movement. The topographic and rheological similarities between the Puget Lowland and modern margins of the GrIS and AIS, respectively, support the application of findings from this work to be extrapolated to contemporary ice systems (e.g., Nield et al., 2014; Eyles et al., 2018; Whitehouse et al., 2019).

Chapter 2: Streamlined subglacial bedform sensitivity to bed characteristics across the deglaciated Northern Hemisphere

Adapted from: McKenzie, M.A., Simkins, L.M., Principato, S., and Munevar-Garcia, S.: Subglacial bedform sensitivity to bed characteristics across the deglaciated Northern Hemisphere, *Earth Surface Processes and Landforms*, 47:9, 2341-2356, <https://doi.org/10.1002/esp.5382>, 2022.

2.1 Introduction

Understanding the conditions that control ice-sheet flow is particularly important for ice streams, conduits of fast-flowing ice at rates of 10^2 – 10^3 m a⁻¹, due to their ability to efficiently drain and destabilize glacial catchments and greatly impact glacial contributions to sea level (Bamber & Aspinall, 2013; Rignot et al., 2019; Serrousi et al., 2017). The character of the underlying terrain (i.e., bed) beneath ice streams influences ice-flow velocity and organization by modulating driving stresses, subglacial hydrology (Falcini et al., 2018; Greenwood et al., 2021; Hall & Glasser, 2003; Hindmarsh, 2001; Maier et al., 2019; Wellner et al., 2001) and spatial variations in ice thickness (Eyles et al., 2018; Payne & Dongelmans, 1997; Roberts et al., 2010). Patterns and rates of ice flow are commonly linked to known or perceived properties of the bed including topography and lithology (Clarke et al., 1977; Cuffey & Paterson, 2010; Whillans & van der Veen, 1997). Bed properties can have opposing effects and varying degrees of influence on ice-stream behavior (De Rydt et al., 2013; Falcini et al., 2018; Greenwood et al., 2021).

Valleys and troughs underlying both marine and terrestrial-based glacial systems have the potential to increase ice-flow velocities due to steering and thickening of ice, leading to increased pressure melting and overall meltwater abundance that enhance basal sliding and sediment deformation (Eyles et al., 2018; Hindmarsh, 2001). Similarly, ice flow is accelerated through strain heating of basal ice (McIntyre, 1985; Pohjola & Hedfors, 2003; Winsborrow et al., 2010) in areas of positive topographic relief (i.e., pinning points, ridges and banks) and regions of high bed roughness (i.e., spatial variation in surface elevation and slope; Falcini et al., 2018; Rippin et al., 2011; Siegert et al., 2005). In other circumstances, obstacles in the bed and deep valley regions surrounded by areas of high topographic relief enhance basal and lateral drag, leading to slower ice flow and potential grounding-line stabilization in marine-terminating systems (Falcini et al., 2018; Favier et al., 2016; Whillans & van der Veen, 1997).

Bed lithology also plays a fundamental role in ice–bed coupling, efficiency of meltwater transmission, and sedimentary processes such as deformation, erosion and deposition (Weertman, 1957). Permeable unlithified sedimentary beds allow for water infiltration and enhanced ice motion due to sediment deformation (Alley et al., 1986; Cuffey & Paterson, 2010; Tulaczyk et al., 2000), whereas more impermeable, “hard” beds facilitate sliding through liquid water being held between the ice and bed (Evans et al., 2006; Nienow et al., 2017). Rates of erosion and deposition in the subglacial environment are fundamentally impacted by bed

lithology due to its control on meltwater transmission and, presumably, relative erodibility differences between different lithologies (Fowler, 2010; Greenwood & Clark, 2010; Ng, 1998).

Erosion and deposition at the ice–bed interface commonly creates subglacial streamlined bedforms, elongate in the direction of ice flow, which indicate sedimentary processes under variable glaciological conditions across landscapes (e.g., Alden, 1905; Charlesworth, 1957; Clark, 1993; Clark et al., 2009; Hollingworth, 1931; King et al., 2009; Menzies, 1979; Shaw et al., 1989; Spagnolo et al., 2010, 2011; Stokes & Clark, 2001, 2002; Wright, 1912). Genetic controls on streamlined bedforms include bed erosion by meltwater (Shaw et al., 2008), ice-keel ploughing (Clark et al., 2003; Tulaczyk et al., 2000), heterogeneous sediment deposition due to orthogonal basal pressure variability (Schoof & Clark, 2008), and till deformation (King et al., 2009). Because many bedform types, such as glacial lineations, are genetically and morphologically similar between contemporary and paleo-glacial systems (King et al., 2009), the location of former warm-based ice flow is interpreted from streamlined bedforms (e.g., Bourgeois et al., 2000; Briner, 2007; Clark, 1993; Clark et al., 2003; Ottesen et al., 2008; Principato et al., 2016; Spagnolo et al., 2014; Stokes et al., 2013; Stokes & Clark, 2001). Streamlined bedforms are commonly well preserved and mark the final or most prominent phase of ice flow across the landscape (Clark, 1999; Winsborrow et al., 2010). Ranging in size from centimeters to several kilometers in length and from centimeters to tens of meters in amplitude, the elongation (i.e., ratio of length to width) of streamlined bedforms is commonly used to infer characteristics of ice-flow speed in deglaciated landscapes, while long-axis orientation is used to infer ice flow direction (e.g., Stokes & Clark, 2001, 2002; Zoet et al., 2021).

Streamlined bedforms in deglaciated landscapes are used to interpret ice-flow behavior (e.g., Clark et al., 2009, 2018; Dowling et al., 2015; Ely et al., 2016; Greenwood & Clark, 2010; Hättestrand et al., 2004; Spagnolo et al., 2012, 2014; Stokes et al., 2013) and used to understand ice–bed interactions applicable to contemporary glacial systems (e.g., Eyles et al., 2018; Greenwood et al., 2021). Qualitative (i.e., visually descriptive) and quantitative (i.e., morphometric and statistical) analyses of streamlined bedforms are arduous tasks as these bedforms have low, even sub-meter vertical relief and typically occur in “swarms” of tens to thousands of bedforms (Clark et al., 2018; Ely et al., 2016; Hughes et al., 2010). While automated mapping methods more quickly detect streamlined bedforms than traditional manual mapping techniques, only a subset of these methods have been systematically applied across multiple sites (e.g., Cazenave et al., 2008; Clark et al., 2009; Saha et al., 2011; Spagnolo et al., 2017; Wang et al., 2017). Our study uses topographic positioning index (TPI; Tagil & Jenness, 2008; Weiss, 2001) to calculate “neighborhood” elevation and slope variations to semi-automatically identify subglacial streamlined bedforms from nine deglaciated landscapes in the Northern Hemisphere (Figure 2.1). This large, geographically diverse dataset of streamlined bedforms contains both bedrock and sedimentary bedforms, encompassing a range of erosional and depositional processes associated with ice flow of four former ice sheets. We aim to identify the sensitivity of warm-based ice-flow conditions and subglacial processes to variable bed

conditions. Substrate influence on warm-based ice flow is inferred from bedform relationships with bed topography and lithology, independent of bedform genesis concepts.

2.2 Methodology

We examined nine study sites including (A) the Puget Lowland in Washington, USA, formerly glaciated by the southern Cordilleran Ice Sheet (CIS); (B) Northwestern Pennsylvania, USA and (C) Chautauqua, New York, USA, glaciated by the southern Laurentide Ice Sheet (LIS); (D) M'Clintock Channel, Canada; (E) Prince of Wales Island, Canada; (F) Nunavut, Canada, glaciated by interior reaches of ice streams, terminating at the margin of the LIS (Margold et al., 2018); (G) Bárðardalur, Iceland, glaciated by the Icelandic Ice Sheet; and (H) northern Norway and (I) northern Sweden, glaciated by the Fennoscandian Ice Sheet (Figure 2.1; Table 2.1). While all sites were glaciated during the Last Glacial Maximum (LGM; 23,000–19,000 years ago; Hughes et al., 2013) and the surface-exposed streamlined bedforms represent LGM and post-LGM ice flow, some bedforms may have formed during earlier glaciations or be multi-generational in nature. Because this process-based study focuses on resultant bedform morphology and distribution, we refrain from integrating absolute ages outlining when the bedforms formed or when the sites were deglaciated—information that does not exist for each study site and is therefore beyond the scope of this project.

Extensive efforts by state and national agencies to collect high-resolution digital elevation data allow for glacial landforms to be mapped at unprecedented spatial scales. Bed topography at each site was classified using publicly available digital elevation models (DEMs) with the highest clarity of 2 m vertical and 1.83 m × 1.83 m horizontal resolution and lowest clarity of 10 m vertical and 30 m × 30 m horizontal resolution, coupled with regional geology maps (Clallam County, Olympic Department of Natural Resources, WA, 2008; Porter et al., 2018; USGS, 1999, 2000). Present-day elevations of the DEMs differ from elevations at the time of glaciation due to glacial isostatic adjustment (GIA), tectonics and post-glacial landscape evolution; however, while absolute elevation differs from the LGM, relative relief at the streamlined bedform scale has not significantly changed. Visual hillshades for each DEM were created by utilizing ambient occlusion techniques, where multiple-scale and multi-directional hillshades were combined to create an incident lighting effect. This approach highlights the first-order detail on surface structures at different scales required to identify the wide range of streamlined bedforms presented here.

We classified topographic setting in the broadest sense as either “constrained” or “unconstrained” on spatial scales of 10^1 – 10^2 km (Payne & Dongelmans, 1997). “Constrained” topography is defined as low elevation surrounded by more elevated regions on the horizontal scale of 1 – 10^2 km and vertical changes of at least 400 m from valley bottom to top, while “unconstrained” topography is defined as open, relatively uniform topography on the horizontal scale of 1 – 10^2 km with no more than 400 m of vertical elevation change across the site

(Figure A2.1). Therefore, valleys, troughs and basins are considered constrained topography, while unconstrained topography lacks these features in the regional landscape.

Surficial bed lithology was generally classified as: “lithified sedimentary” including both clastic and carbonate bedrock; “crystalline”; “volcanic rock”; or, in one case, “mixed” bed including both crystalline and unlithified sedimentary beds. These distinctions were made due to the general variation in primary permeability, erodibility and likelihood of these lithologies to develop into a deformable subglacial bed. Unlithified sedimentary beds are the most permeable, erodible and likely to support a deformable bed, whereas the crystalline bedrock sites are the least permeable, erodible and least likely to contribute to the formation of a deformed till layer compared to a sedimentary bed. Only underlying bed composition was considered in determining site lithology; therefore, thin layers of till or soils overlying crystalline bed sites were not considered in bed lithology classification. While there are differences in properties between, for example, clastic and carbonate sedimentary rocks, the differences are subtle enough for the two categories to be classified together for the purpose of this regional and bedform-assemblage scaled work.

We mapped streamlined bedforms from the nine sites with a combination of manual identification and a novel semi-automated application of a TPI mapping tool, originally developed for the purpose of characterizing watersheds across regional landscapes (Weiss, 2001). TPI utilizes DEM cell elevation and mean elevation of a defined neighborhood to calculate slope variations across a landscape. Annulus neighborhood sizes were determined by assessing the visible range in scales of bedforms present. At least two neighborhood assessments, ranging from 300 to 2100 m, were conducted for each site and determined separately for each site based on the overall elevation range of the landscape and visual estimates of streamlined bedform metrics. Once the inner and outer neighborhood radius is defined, TPI calculates the mean elevation across the defined neighborhood for each pixel. A standardization is then used across the entire map to ensure varying sites are comparable. The tool, built using ArcPython code and ArcGIS ModelBuilder, was published for use (McKenzie et al., 2022). After standardization, TPI values above zero represent areas higher than surrounding topography, while negative TPI values measure locations lower than their surroundings. Using spatial analyst tools, all positive relief features identified by TPI, including features other than non-subglacial streamlined bedforms, were separated into a polygon file (McKenzie et al., 2022; Figure A2.2). Thresholding of TPI-mapped bedform metrics such as feature length, width, orientation and area attributes coupled with a manual assessment, conducted by visually removing incorrectly identified features and adding features missed by TPI, resulted in a more accurate dataset whose metrics were not influenced by morphometric threshold sorting (McKenzie et al., 2022; Figure A2.2).

For each mapped bedform, its long-axis length and orientation, width orthogonal to length, and the range in elevation along the landform’s long axis (termed here “bedform surface relief”) were calculated automatically in ArcGIS Pro using the “Minimum Bounding Geometry” and “Add Z Information” tools. Automatic calculation of streamlined bedform long-axis cardinal

orientation is quantified in degrees, measured by the rotation of the bedform long axis from due north, and is used to infer direction of ice flow (Clark, 1997; Kleman et al., 2006; Kleman & Borgström, 1996). Parallel conformity, or the standard deviation of an entire streamlined bedform dataset's orientation values at a given site, was additionally calculated in Excel. Bedform elongation ratio, calculated by dividing the bedform length by its width, and parallel conformity (i.e., the standard deviation of bedform orientation) were calculated in Excel. Defining bedforms solely by their shape rather than composition is a strength to this study, as it allows for the assessment of topographic and lithologic controls on ice streaming and sedimentologic and geomorphologic processes regardless of landform-generating processes that have been inferred for individuals or groups of landforms.

Statistical analyses including a linear Pearson correlation and Shapiro–Wilk test were conducted in “R” to compare bedform metric distributions. Qualitative metrics, namely site topography and lithology, were assigned a fixed numerical value that was used in the Pearson correlation, where topographically unconstrained regions were assigned a value of 0 and topographically constrained were assigned a value of 1. Sedimentary bedrock was assigned a value of 0, crystalline bedrock a 1, volcanic bedrock a 2 and mixed lithology a 3.

2.3 Results

In the following subsections, we demonstrate our use of TPI to identify streamlined subglacial bedforms, the trends and correlations of bedform morphology across all sites, and the relationship between spatial orientation and distribution of bedforms. Lastly, we describe the relationship between bedform characteristics and bed topography and lithology.

2.3.1 Streamlined subglacial bedform identification

Across the nine sites, TPI identified 7,635 bedforms, while 3,993 bedforms were manually mapped (i.e., added or adjusted from TPI mapping), resulting in a total dataset of 11,628 sedimentary and bedrock bedforms (Figure 2.2). Of the nine study sites, the Puget Lowland (Site A) and M'Clintock Channel (Site D) sites had the highest proportion of bedforms correctly mapped by TPI as determined by visual inspection, requiring a lower percentage of false-positive bedforms to be manually removed (Table 2; Figure A2.3). Sites with low variation in site elevation, such as those in northwestern Pennsylvania (Site B) and Chautauqua (Site C), required the least manual bedform mapping (Figure 2.2; Table 2.2). In northern Sweden (Site I), the number of bedforms considered incorrectly identified by TPI exceeded the number of those that were considered correctly identified. Sites with the greatest number of bedforms manually added to the final dataset include northern Norway (Site H) and northern Sweden (Site I). There was no statistical significance between the proportion of TPI-identified false positives and the proportion of bedforms manually added to bed topography and lithology across the sites. Almost all scales of known streamlined bedforms (Ely et al., 2016) are resolved by DEMs and

potentially identified by TPI, except for bedforms with millimeter to centimeter surface relief. The lowest relief of bedform surface mapped by TPI is <1 m, providing confidence in the ability of these dual methods to capture a “full” dataset of streamlined subglacial bedforms (Figure A2.3).

2.3.2 Bedform morphology

The streamlined bedforms range in length from 94 to 15,388 m (mean 1,052 m; median 754 m) and in width from 19 to 2,323 m (mean 219 m; median 157 m). As determined by a linear Pearson correlation, bedform length and width have a positive correlation coefficient (Figure 2.3). This statistical analysis was fitting for this data as it met the assumption that all groups were statistically significant in their difference from one another ($p < 0.05$). Puget Lowland (Site A) bedforms span the greatest range in width and length of all sites, while Chautauqua (Site C) has the smallest ranges of length and width. Interestingly, low bedform lengths and widths are common for all sites, while bedforms with lengths greater than ~2000 m and widths greater than ~600 m are less common (Figure 2.4A).

A minimum ratio of length to width (i.e., elongation; e.g., Clark et al., 2009; Ely et al., 2016) of 1.12:1 is distinct for all sites. Consistency in peak elongation ratios for all sites is also observed, with a median elongation ratio of 5:1 (Figure 2.5; Table 2.2). The degree of positive skewness of elongation varies by site, with sites Bárðardalur (Site G) and northern Sweden (Site I) highly skewed, while sites Chautauqua (Site C) and northwestern Pennsylvania (Site B) are the least positively skewed, as determined by a Shapiro–Wilk normality test. The northern Norway (Site H) site has the highest mean and median bedform elongation ratio values, while Bárðardalur (Site G) has the greatest range of elongation ratio of all sites (Figure 6B; Hoffmann, 2015). Chautauqua (Site C) bedforms have the smallest elongation ratio mean, median and range of all sites (Figure 2.6B, Hoffmann, 2015). Bedform length and elongation as well as bedform length and width are positively correlated (Figure 2.3).

The Puget Lowland (Site A) has the highest mean, median and range of individual bedform surface relief than any other site (Figure 2.6A; Hoffmann, 2015). Prince of Wales Island (Site E) has the smallest mean and median bedform surface relief, while M’Clintock Channel (Site D) has the smallest bedform surface relief of all sites (Figure 2.6A; Hoffmann, 2015). Bedform length and bedform surface relief have a strong positive correlation coefficient (Figure 2.3). When comparing individual bedform elongation and bedform surface relief, more elongate bedforms correspond to more uniform bedform surface relief (Figure 2.4C, D). Conversely, less elongate bedforms display greater variation in individual bedform surface relief (Figure 2.4D).

2.3.3 Bedform parallel conformity and distribution

While streamlined bedform orientations vary by site depending on predominant direction of ice flow, the average parallel conformity (i.e., standard deviation of orientation) of all sites is 26° (Figure 7). Multiple sites, including M’Clintock Channel (Site D) and Prince of Wales Island (Site E), have notable variations and cross-cutting relationships between bedforms of different orientations, indicating two temporally distinct flow orientations, although one flow orientation is far more prominent (Figures 2 and 7). Two of the topographically constrained sites, Bárðardalur (Site G) and northern Norway (Site H), are clearly influenced by topographic steering of bedform orientation (Figure 7). Swarms of bedforms at M’Clintock Channel (Site D) are more elongate in the center of the mapped clusters than the edges, while bedform elongation at all other sites varies without apparent spatial organization. At M’Clintock Channel (Site D), where we see this spatial organization of bedform elongation, the bedforms also express high parallel conformity and high density and packing (Figure 8; Table 2).

2.3.4 Bedform morphometric correlations with bed lithology and topography

The Puget Lowland (Site A), a topographically constrained mixed lithology site, has the greatest number of bedforms per area (i.e., density) and the highest bedform area per area (i.e., packing; Table 2) compared to the eight other sites. Altogether, the topographically unconstrained sites with sedimentary bedrock have the next highest packing or density values (Table 2).

The topographically constrained volcanic bed of Bárðardalur (Site G) contains low-density and packing bedform swarms and has the most elongate bedforms in the dataset (Figure 8; Table 2). After Bárðardalur (Site G), the sites with the most elongate bedforms are also all topographically constrained sites (Table 2). Utilizing a linear Pearson correlation, constrained topography has a high positive correlation coefficient with elongation and bedform surface relief, while unconstrained topography is correlated with greater bedform width (Figure 3). Bed lithology has a strong negative correlation coefficient, with bedform width indicating that large widths are likely on sedimentary bedrock sites while bedforms with smaller widths are more common in mixed lithology sites. Conversely, bedform surface relief is highly correlated with surface lithology, where sedimentary bedrock sites have lower bedform surface relief and mixed lithology sites have greater bedform surface relief (Figure 3). Regardless of these differences, all sites have similar morphometric distributions and show considerable overlap with common means and medians, rather than distinct populations, and only differ in the degree of skewness.

2.4 Discussion

A discussion of the performance of TPI in mapping subglacial streamlined bedforms is presented in the first subsection, followed by discussions of streamlined bedform morphology and the relationship between bedform morphology and bed settings.

2.4.1 Success of semi-automatic mapping streamlined bedforms in deglaciated landscapes

Previous morphometric studies of streamlined subglacial bedforms have utilized Fourier spectra data (e.g., Spagnolo et al., 2017), manual identification (e.g., Principato et al., 2016), object-oriented automatic identification (e.g., Saha et al., 2011), contour-tree mapping (Wang et al., 2017) and other methods systematically utilized to identify bedforms across singular and multiple geographic locations (e.g., Clark et al., 2009, 2018; Ely et al., 2016; Greenwood & Clark, 2010; Spagnolo et al., 2014; Stokes et al., 2013). While TPI was originally developed to classify landscapes and delineate watersheds (Tagil & Jenness, 2008; Weiss, 2001), its ability to characterize negative and positive relief features through slope variations is conceptually applicable to many landscapes. In the context of glacial landscapes, the distinct elongate morphologies and occurrence of numerous bedforms in close proximity make streamlined subglacial bedforms well suited for identification with TPI. In general, highly elongate bedforms with low bedform surface relief are more difficult to map due to small and narrow slope differentiations. Due to the difficulty of the TPI method in identifying these sizes of bedforms, many of the manually mapped bedforms were visually low-relief and highly elongate (Figure A2.3). Additionally, two sites with the greatest number of manually mapped bedforms occurred in northern Norway (Site H) and northern Sweden (Site I; Table 2.2), where preservation of non-glacial or minimally glacially modified landforms is significant across the entire region (Ebert et al., 2012; Hall et al., 2013; Kleman & Stroeven, 1997). These mapping challenges may be a result of residual pre-LGM landform assemblages and bedrock morphologies from pre-Quaternary formation and weathering processes (e.g., Ebert et al., 2012; Hall et al., 2013; Kleman & Stroeven, 1997). Landscape features that were manually removed include non-glacial positive relief features such as modern riverbanks and isolated bedrock highs, identified by their location, size, orientation or lack of any elongation. While there were some shortcomings in the bedform TPI identification method developed for this work, the hundreds of hours saved by semi-automatically identifying these bedforms renders this tool highly useful. Use of the TPI identification tool also reduces investigator bias through its systematic identification of positive relief features across a landscape.

While the percentage of bedforms incorrectly mapped by TPI has no correlation to site topography or lithology (Table 2.2), the crystalline bed sites in northern Norway (Site H) and northern Sweden (Site I) and volcanic bedrock site in Bárðardalur (Site G) had the greatest proportion of their bedforms identified manually (Table 2.2). The hard beds in Sweden and Norway, less easily eroded, preserve a landscape legacy of older and persistent processes and therefore have many large, high relief features such as inselbergs (e.g., Ebert et al., 2012; Hall et al., 2013). High-relief features dominate the landscape, even in areas impacted by glacial processes. Therefore, glacial features left on the surface are often very subtle and low in relief, creating difficulties for TPI to identify these small relief bedforms amidst the more pronounced, high-relief features of these landscapes, making manual identification more suitable for these

types of bedforms. TPI, therefore, does not perform as well on crystalline bedrock sites as it does on sedimentary bedrock sites where glacial erosion has a larger impact on surface relief. It is also important to note that the crystalline bedrock sites (Sites F, H, I) were deep in the ice sheet interior, where cold-based ice is thought to have been prevalent for long periods over multiple glaciations. Therefore, not only was the crystalline bedrock difficult to erode, but the glaciological environment did not support streamlined bedform processes (Margold et al., 2015; Stokes & Clark, 2001). For a similar reason, the large proportion of manually mapped bedforms in Bárðardalur (Site G) could, in part, be due to a variety of bedform composition and relief ranging from low-relief features comprised entirely of diamicton to high-relief features comprised of diamicton overlaying bedrock cores formed during rifting. More pronounced, high-relief features are more easily identified by TPI mapping, while low relief features are not as easily delineated by the tool.

2.4.2 Bedform properties across the deglaciated Northern Hemisphere

While sub-meter relief bedforms like bedrock striations are not resolved in the dataset presented here, meter to kilometer-scale bedforms like drumlins and flutes are well resolved. Bedforms across the datasets have significant overlap and positive correlation between width and length (Figures 2.3 and 2.4A,B), indicating a shared genetic mechanism between bedforms regardless of their composition or whether they formed through erosional or depositional processes. Additionally, both length and width data are positively skewed, with more small bedforms than large (Figure 2.4A,B). This process of bedform elongation is commonly referenced in the field and has led to the use of elongation as a proxy for ice streaming velocity and length of time that a particular flow regime has been operating (e.g., Benediktsson et al., 2016; Livingstone et al., 2016; Stokes et al., 2013; Stokes & Clark, 2002).

Although our nine study sites were glaciated by different ice sheets on different continents, resulting subglacial bedforms were found to be morphologically similar (e.g., Stokes & Clark, 2002; Clark et al., 2009; Saha et al., 2011; Spagnolo et al., 2014; Principato et al., 2016). The similarities in quantitative bedform morphometrics across the study sites suggest similar genetic relationships between all streamlines subglacial bedforms. In this study, we find a minimum length to width ratio (i.e., elongation; e.g., Clark et al., 2009; Ely et al., 2016) of 1.12:1, indicating that barely elongate bedforms are (1) resolved in the dataset and (2) occur for the full size range of bedforms (Figure 4A,B) potentially due to the highly dynamic and rapidly evolving bedform development beneath warm-based ice (Stokes et al., 2013). In other terms, we observe that a large bedform can be equally as stunted as a small one, suggesting that growth of bedforms does not necessarily add length or strip width preferentially and there is not one single style of bedform development. The unimodal distribution of elongation ratios with positive skewness seen in this work, indicating a continuum of bedform types, has also been found in other morphological bedform assessments (Figure 2.5; e.g., Clark et al., 2009; Saha et al., 2011; Stokes et al., 2013; Spagnolo et al., 2014; Ely et al., 2016; Principato et al., 2016).

We find that less elongate bedforms are interspersed with more elongate features and not present at the margins of bedform swarms (Figure 2.8). This result is not unique and has been hypothesized to be a result of the rapidly changing subglacial dynamics responsible for bedform formation and development (Rattas & Piotrowski, 2003; Stokes et al., 2013). An exception of this observation is at M'Clintock Channel (Site D), where the largest, most elongate bedforms at this site are spatially centered in the middle of the mapped bedform swarm, while the least elongate bedforms flank the lateral edges (Figure 2.8). This spatial organization likely represents a centralized zone of stronger ice streaming, where lateral drag slowed ice flow along the edges. At the M'Clintock Channel site (Site D), we see direct evidence for ice streaming where fast-flowing ice is bounded by slower moving ice (Margold et al., 2018). The spatial organization of elongation at M'Clintock Channel (Site D) contains classic assemblage characteristics associated with fast-flow corridors (e.g., Spagnolo et al., 2014; Stokes et al., 2013; Stokes & Clark, 2001, 2022, 2003).

While particularly notable at topographically constrained and easily eroded bed substrates, all sites showcase a trend of more elongate bedforms corresponding to lower bedform surface relief (Figure 2.4C,D). This pattern is an indication of ice-flow persistence (Benediktsson et al., 2016), whereby persistent erosion and deposition at the ice–bed interface in conjunction with warm-based ice flow produce a flat bedform feature. Conversely, less elongate bedforms correlate with greater variability in bedform relief (Figure 2.4C,D), suggesting areas of faster-flowing ice have a glaciological control of more persistent and uniform organization of subglacial erosion and deposition. Therefore, in areas where ice streaming is not persistent or stable or ice velocities are relatively slow, erosion and depositional processes are more spatially heterogeneous to result in uneven individual bedform surface relief. Controls on the occurrence of bedform development may be directly related to variations in bed lithology (Greenwood & Clark, 2010) and topography (Falcini et al., 2018; Favier et al., 2016; Whillans & van der Veen, 1997) or could be indirectly related through substrate control on glaciologic processes. However, this distinction was not explicitly assessed for individual bedforms within this study.

2.4.3 Bedform morphology in relation to bed setting

Spatially stable and persistent ice streaming conceptually contributes to spatial homogeneity in erosion and deposition processes, leading to the formation of consistently orientated and shaped bedforms. Deviations to bedform orientation occur from both temporal and spatial variations, where bedforms can be preserved from multiple glaciations, such as in northern Sweden (Site I), or across constrained topography, such as in the Puget Lowland (Site A), Bárðardalur (Site G) and northern Norway (Site H). Regions with highly elongate bedforms correspond to qualitatively greater flow orientation organization (Figures 2.6 and 2.8; Table 2.2), which is potentially attributed to multi-generational or persistent bedform formation and development. Multiple glaciations in the same orientation produce more uniformly oriented features (i.e., higher parallel conformity). In the case of spatially influenced orientation,

topographic constrains on ice-flow develops bedform clusters with orientation that reflects the orientation of the valley in which it is constrained, such as in Bárðardalur (Site G).

Findings from previous work on bedform presence and morphologies identify glaciological drivers as fundamental controls on bedform morphology via subglacial processes, while others identify direct substrate control on resulting bedform morphologies due to inherent characteristics in the bed (e.g., Greenwood & Clark, 2010; King et al., 2009; Rattas & Piotrowski, 2003; Stokes et al., 2013). Qualitatively soft, more permeable and easily eroded beds allow for greater production and transport of sediment to the ice margin (Clark, 1993; Rattas & Piotrowski, 2003; King et al., 2009; Livingstone et al., 2016). The abundance of deformable till forming from the permeable environments of both lithified and unlithified sedimentary beds explains the presence of high-density bedforms in the regions with unlithified sediment (King et al., 2009; Stokes et al., 2013). Conversely, “hard”, crystalline beds are generally more resistant to erosion (Eyles & Doughty, 2016; Krabbendam et al., 2016) and more likely to have “foxed” bedforms resistant to sediment production and transport (Zoet et al., 2021). The greatest number of bedforms per area, present on a mixed (unlithified sedimentary bed system with crystalline bedrock) bed in the Puget Lowland (Site A), likely occur due to high availability of unlithified sediments and meltwater presence from strain heating. Strain heating occurs as ice flows over bedrock highs, collectively allowing for greater bed erosion across the permeable unlithified sediment, material deposition and subsequent ice streaming (McIntyre, 1985; Pohjola & Hedfors, 2003; Winsborrow et al., 2010). In addition to the mixed bed site, lithified sedimentary beds were also densely populated with streamlined bedform features (Table 2.2). Crystalline and volcanic beds in both constrained and unconstrained topographic settings have the lowest bedform densities, suggesting that bed lithology, rather than topography, is a more dominant control on streamlined bedform density. However, it remains unclear and difficult to assess whether bed substrate controls either sedimentary processes regardless of flow regime or whether substrate controls streaming conditions. In either case, a distinct bedform signature across a particular bed substrate is produced.

The unimodal and positively skewed distribution of bedform elongation indicates that similar distributions of elongation occur at a multitude of sites regardless of bed topography and lithology or climatological and glaciological factors (Table 2.1; Figure 2.4A,B; e.g., Clark et al., 2009; Ely et al., 2016; Principato et al., 2016; Saha et al., 2011; Spagnolo et al., 2014; Stokes et al., 2013). The minimum elongation threshold and similarity in relative elongation distribution across sites highlight a similarity of ice–bed interactions across “soft” and “hard” beds in both topographically confined and unconfined settings, suggesting a self-organization of ice–bed processes regardless of site characteristics. The concept of streamlined bedforms developing as a self-organizing phenomenon is not novel in the field of glacial geomorphology and has been suggested to occur independently from local bed lithologic and topographic conditions (Clark 2010; Spagnolo et al., 2017; Clark et al., 2018). This independent organization is well represented by the unit-less elongation ratio and allows for comparison of warm-based ice-flow velocities or persistence between individual sites. Differences in elongation distributions across

sites of variable topography or bed lithology would suggest an influence of substrate on bedform formation and development or substrate influence of glaciologic processes at the bed. However, from the similarities in bedform elongation distribution we see here and in previous work, we suggest that regions of warm-based ice flow, leading to the development of streamlined subglacial bedforms, exhibit potential for equivalent relative ice-flow velocity distribution or persistence of ice-flow pathways regardless of bed character.

While all sites have similar elongation distribution trends, topographically constrained sites produce bedforms with the highest mean and median elongation ratios with the most elongate bedforms of the overall dataset (Figure 2.6B; Tables 2.1 and 2.2). Topographic constraint on ice flow results in topographic funneling and increased ice speed (Hindmarsh, 2001; Wellner et al., 2001; Hall & Glasser, 2003; Ottesen et al., 2008; Roberts et al., 2010; Eyles et al., 2018). While bedform elongation is enhanced in regions that are topographically constrained, bedform elongation is not contingent on bedrock substrate (Figure 2.6B; Tables 2.1 and 2.2), which we interpret to reflect a higher sensitivity of warm-based ice-flow velocity and persistence to bed topography than bed substrate (Greenwood et al., 2021; Halberstadt et al., 2016; Ignéczi et al., 2018; Serrousi et al., 2017; Stokes & Clark, 2003; Winsborrow et al., 2010). Additionally supporting this argument, we find the topographically unconstrained and lithified sedimentary bed sites in Chautauqua (Site C) and northwestern Pennsylvania (Site B) have the least elongate bedforms, despite the potential for deformable substrates on these more easily erodible and mobile beds, indicating that distinct bedform morphologies are developed through topography. More specifically, it is the effect of topography on glacial conditions that allows for distinct bedform elongation to develop.

Topographically constrained regions also produce large variations in individual bedform surface relief (Figure 2.6), indicating less consistency in erosion and deposition distribution across the surface. This effect is particularly apparent at topographically constrained sites with easily eroded beds such as those in the Puget Lowland (Site A) and Bárðardalur (Site G; Figure 2.6). Large values of bedform surface relief in the Puget Lowland (Site A) may also be explained by the presence of isolated crystalline bedrock highs or the presence of bedforms on steep slopes (Spagnolo et al., 2012). However, due to the role of glacial ice in shaping these crystalline bedrock highs, and the significance of other metrics that correspond to large variations in bedform surface elevation, these features with large surface elevation changes were included in the final dataset. The streamlined bedforms present in the Bárðardalur valley (Site G) are lower in elevation than those found along the valley edges (Figure A2.1) and were therefore topographically controlled during ice thinning of the Icelandic Ice Sheet (Benediktsson et al., 2022). However, it is unlikely that the bedforms with the highest surface relief in Bárðardalur (Site G) are entirely composed of diamicton like the bedforms with smaller surface relief. We suggest the high relief bedforms in Bárðardalur (Site G) are comprised of diamicton overlying bedrock cores from pre-existing topography; however, further investigation of these features is needed to confirm this interpretation.

Topographically unconstrained sites with lithified sedimentary bed conditions create bedforms with the most uniform elongation and surface relief (Figure 2.6), indicating these regions are most suitable for persistent, warm-based ice flow across the bed with well-developed processes of erosion and deposition in the subglacial environment (e.g., Benediktsson et al., 2016; Rattas & Piotrowski, 2003; Stokes et al., 2013). Lithified sedimentary sites that are topographically unconstrained have some of the greatest bedform densities (Table 2.2), highest orientation uniformity (Table 2.2; Figures 2.7 and 2.8), and smallest bedform relief and elongation, as previously mentioned (Figure 2.6), further suggesting these settings are favorable for persistent ice flow.

2.5 Conclusions

The large, semi-automatically mapped dataset developed in this work provides key insight into topographic and bed lithology controls on ice flow properties that should be applied to understanding contemporary systems (King et al., 2009). The application of TPI developed in this study highlights its widespread ability to quickly map thousands of bedforms with little computational time, about half of the human error, and subjectivity with only a few shortcomings, including its difficulty in identifying low-relief, elongate subglacial bedforms across landscapes with prominent pre-glacial topography (Ebert et al., 2012; Hall et al., 2013). From the results of the dataset, we learn that landform signatures of warm-based ice flow have remarkable morphometric distribution similarities regardless of bed topography and lithology. All regions of ice flow, measurable by the presence of streamlined bedforms, are capable of similar ice-flow velocity distributions regardless of bed characteristics. However, we find that topographically constrained sites have the most elongate bedforms of the entire dataset, indicating that topography has a first-order control on ice flow velocity and persistence, controlling streamlined bedform elongation through topographic funneling (Eyles et al., 2018; Hall & Glasser, 2003; Hindmarsh, 2001; Ottesen et al., 2008; Roberts et al., 2010; Wellner et al., 2001). In this case, it is interpreted that substrate properties control the glaciological environment to develop bedforms with distinct high elongation.

While bedform elongation is controlled by topography, sites with sedimentary beds contain the greatest number and area of bedforms per area, indicating that bedrock lithology has a more dominant control on density and packing than bed topography. Topographically unconstrained sedimentary beds support formation and development of bedforms with uniform elongation ratios, low bedform surface relief, uniform bedform orientation and high bedform density, indicating that these sites are most suitable for the development of persistent ice flow with well-organized subglacial erosive and depositional processes.

Due to the fundamental role of bed topography and substrate in determining ice dynamics (Clarke et al., 1997; Cuffey & Paterson, 2010; Greenwood et al., 2021; Whillans & van der veen, 1997), assessment of streamlined bedform morphologies provides crucial information on bed-related controls to ice flow (Stokes & Clark, 2001, 2002; King et al., 2009). As

contemporary ice streams continue to retreat across environments with variable topography and bed lithology that are difficult to access and visualize, the use of preserved streamlined bedforms from paleo-subglacial environments is highly beneficial to constraining subglacial process sensitivities to variable bed conditions (Eyles et al., 2018; Greenwood et al., 2021; King et al., 2009; Stokes & Clark 2001, 2002).

Table 2.1. Site descriptions and data information for nine deglaciated sites across the Northern Hemisphere.

Site	Latitude, longitude	Bed setting	Topographic setting	LGM ice sheet	Land surface area (km ²)	Vertical resolution (m)	Horizontal resolution (m × m)
(A) Puget Lowland, Washington State ¹	122.8041731° W, 47.3591840° N	Mixed	Constrained	Cordilleran Ice Sheet	2,713	2	1.83 × 1.83
(B) Northwestern Pennsylvania ²	79.9094684° W, 41.9908560° N	Lithified sedimentary bed	Unconstrained	Laurentide Ice Sheet	1,483	10	30 × 30
(C) Chautauqua, New York ³	79.4920982° W, 42.1933209° N	Lithified sedimentary bed	Unconstrained	Laurentide Ice Sheet	1,128	10	30 × 30
(D) M'Clintock Channel, Canada ⁴	106.0527872° W, 72.6426653° N	Lithified sedimentary bed	Unconstrained	Laurentide Ice Sheet	5,000	2	2 × 2
(E) Prince of Wales Island, Canada ⁴	98.7397049° W, 72.2545398° N	Lithified sedimentary bed	Unconstrained	Laurentide Ice Sheet	5,303	2	2 × 2
(F) Nunavut, Canada ⁴	83.5785928° W, 69.3271212° N	Crystalline bed	Unconstrained	Laurentide Ice Sheet	1,962	2	2 × 2
(G) Bárðdalur, Iceland ⁴	17.4280416° W, 65.1232720° N	Volcanic bed	Constrained	Icelandic Ice Sheet	3,220	2	2 × 2
(H) Northern Norway ⁴	23.6397066° E, 69.6518249° N	Crystalline bed	Constrained	Fennoscandian Ice Sheet	5,000	2	2 × 2
(I) Northern Sweden ⁴	22.4763304° E, 67.0992965° N	Crystalline bed	Unconstrained	Fennoscandian Ice Sheet	15,000	2	2 × 2

Data sources: ¹Cllallam County, Olympic Department of Natural Resources, WA, 2008; ²USGS, 2000; ³USGS, 1999; ⁴Porter et al., 2018.

Table 2.2. Bedform data by site, including spatial statistics and bedform metrics.

Site		Number of bedforms (removed; added)	Number of final bedforms per 10 km ²	Bedform area (km ²) per 10 km ²	% bedforms mapped manually	% TPI mapped false positives	Mean length ± standard deviation	Mean width ± standard deviation	Mean elongation	Parallel conformity
(A) Puget lowland, Washington state	V, mixed bed lithology	1,978 (512; 401)	7.3	3.8	20	20	2,013 ± 1,261	365 ± 180	5.9	27
(B) Northwestern Pennsylvania	O, sedimentary bedrock	881 (774; 60)	5.9	0.5	7	50	666 ± 342	162 ± 69	4.4	11
(C) Chautauqua, New York	O, sedimentary bedrock	702 (493; 103)	6.2	0.7	10	50	652 ± 337	164 ± 77	4.1	10
(D) M'Clintock Channel, Canada	O, sedimentary bedrock	1,737 (333; 615)	3.5	1.1	40	20	1,259 ± 789	278 ± 153	5.0	31
(E) Prince of Wales Island, Canada	O, sedimentary bedrock	1,588 (1,657; 665)	3.0	0.8	40	60	1,054 ± 882	224 ± 162	4.9	51
(F) Nunavut, Canada	O, crystalline bedrock	738 (>800; 155)	3.8	0.3	20	60	617 ± 614	115 ± 88	5.4	7
(G) Bárðdalur, Iceland	V, volcanic bedrock	659 (745; 326)	2.1	0.3	50	50	1,006 ± 701	175 ± 125	6.6	59
(H) Northern Norway	V, crystalline bedrock	1,427 (526; 783)	2.9	0.3	50	50	842 ± 580	132 ± 68	6.9	17
(I) Northern Sweden	O, crystalline bedrock	1,918 (2,241; 858)	1.3	0.6	50	70	1,324 ± 794	346 ± 187	4.1	19

Across site bed settings, a "V" denotes a topographically constrained site, while "O" denotes a topographically unconstrained site. Parallel conformity is a measurement of the standard deviation of mean orientation.

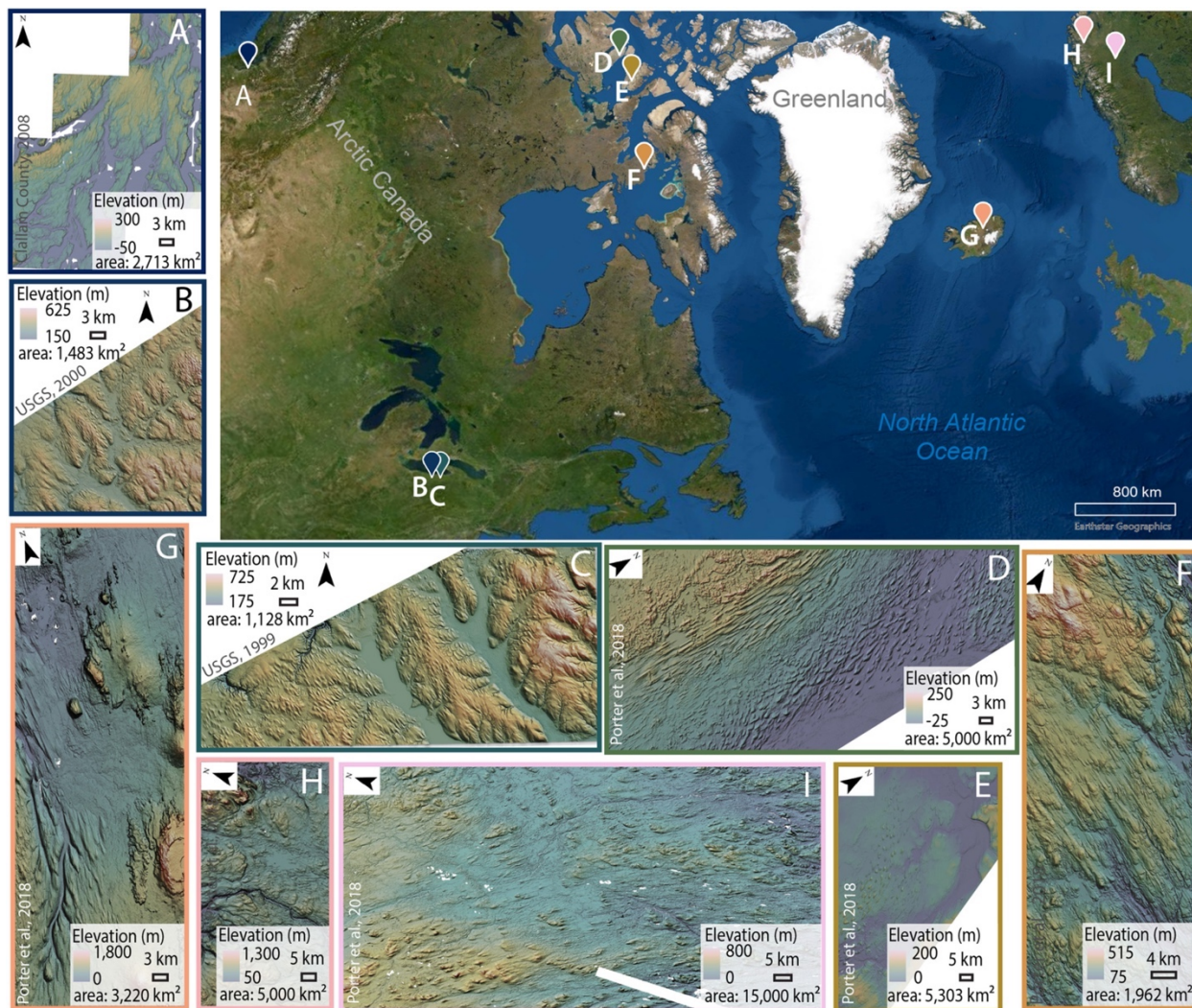


Figure 2.1. Study sites: (A) Puget Lowland, Washington, USA; (B) northwestern Pennsylvania, USA; (C) Chautauqua, NY, USA; (D) M'Clintock Channel, Canada; (E) Prince of Wales Island, Canada; (F) Nunavut, Canada; (G) Bárðardalur, Iceland; (H) northern Norway; (I) northern Sweden.

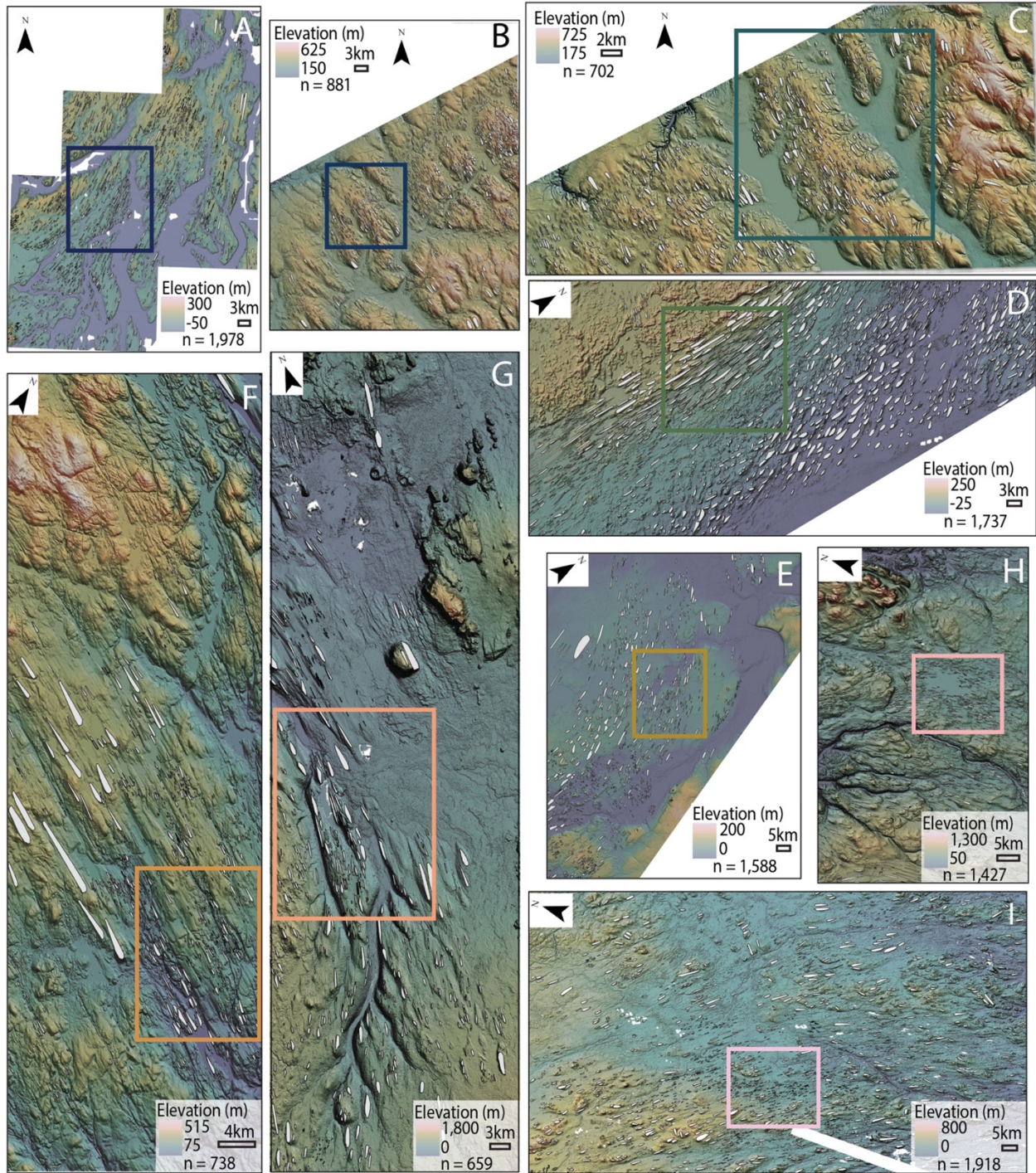


Figure 2.2. Streamlined subglacial bedforms (gray polygons) at sites (A) Puget Lowland, Washington, USA; (B) northwestern Pennsylvania, USA; (C) Chautauqua, NY USA; (D) M'Clintock Channel, Canada; (E) Prince of Wales Island, Canada; (F) Nunavut, Canada; (G) Bárðardalur, Iceland; (H) northern Norway; (I) northern Sweden. Outlined inset boxes are locations shown in Figure 2.8.

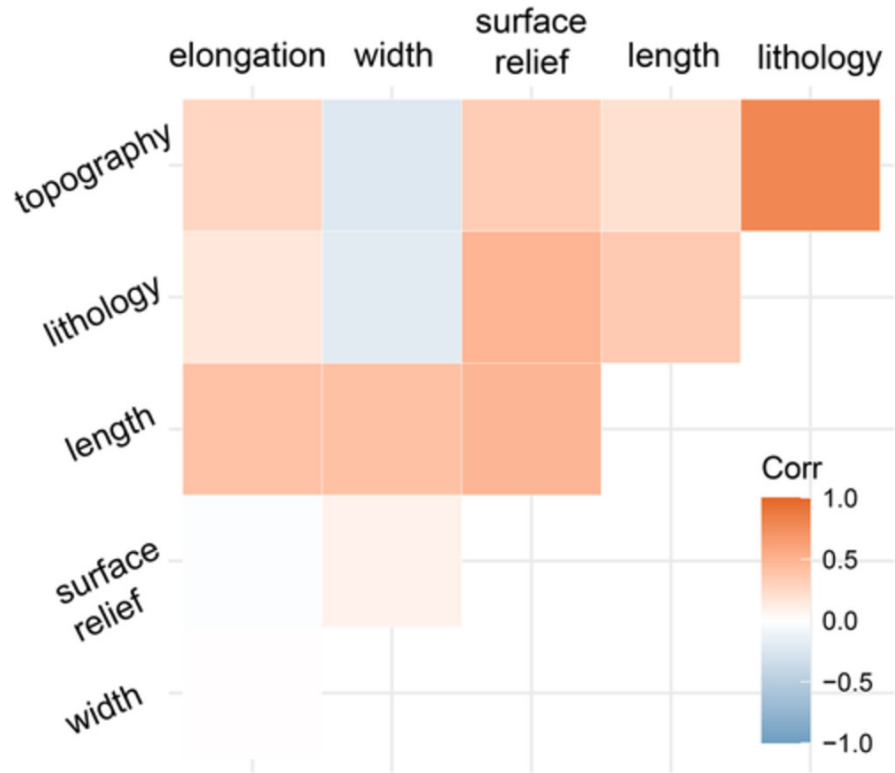


Figure 2.3. Correlation matrix of all 11.628 bedform features, conducted using linear Pearson correlation. Categorical variables were assigned arbitrary values for comparison statistics.

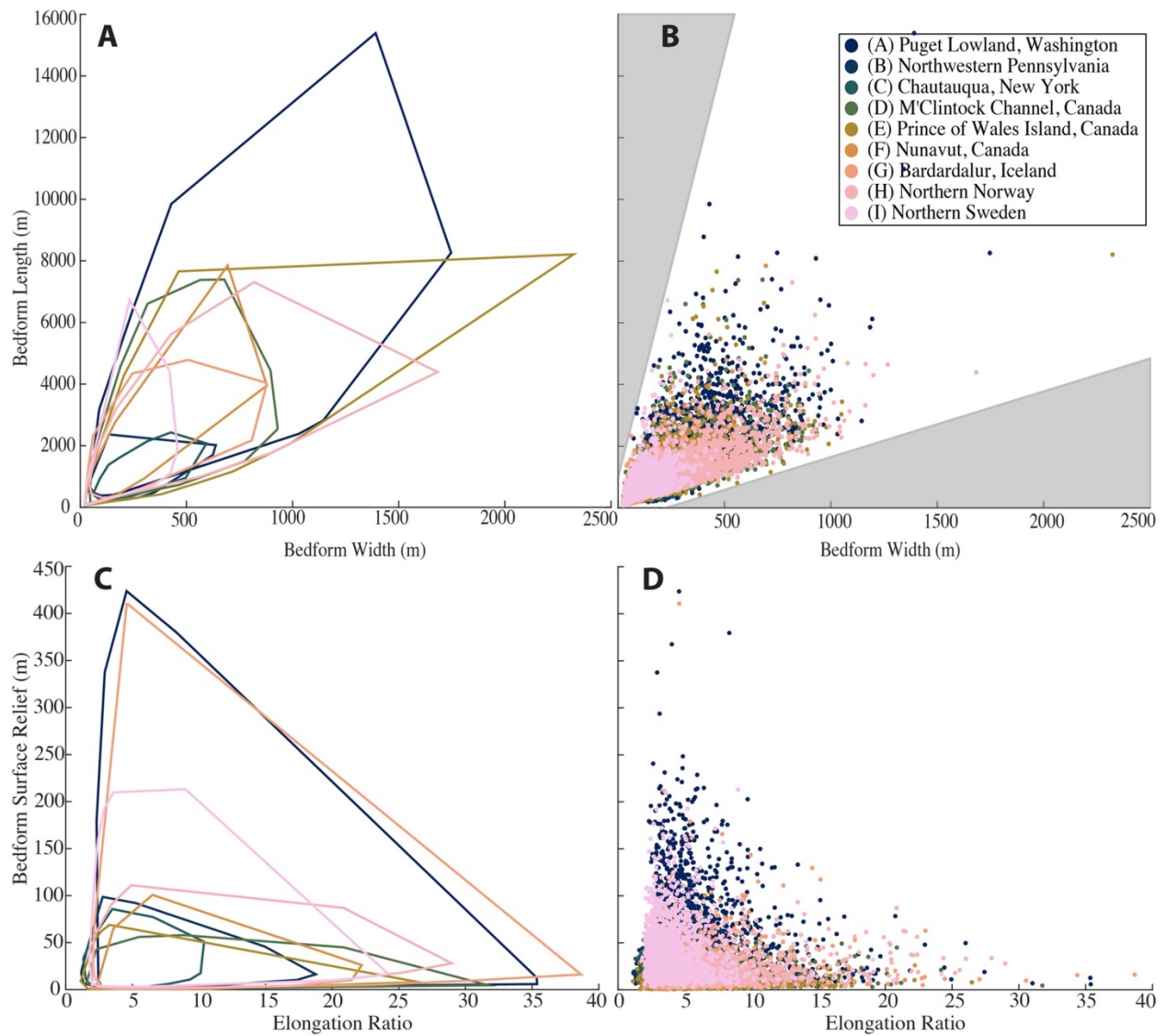


Figure 2.4. Bedform length and width metrics plotted by site: (A) convex hull area of all bedform length and width metrics and (B) scatterplot of the same data as (A); gray areas indicate regions where bedforms are not observed. (C) Convex hull area of all bedform elongation ratio and elevation range metrics; (D) scatterplot of the same data as (C).

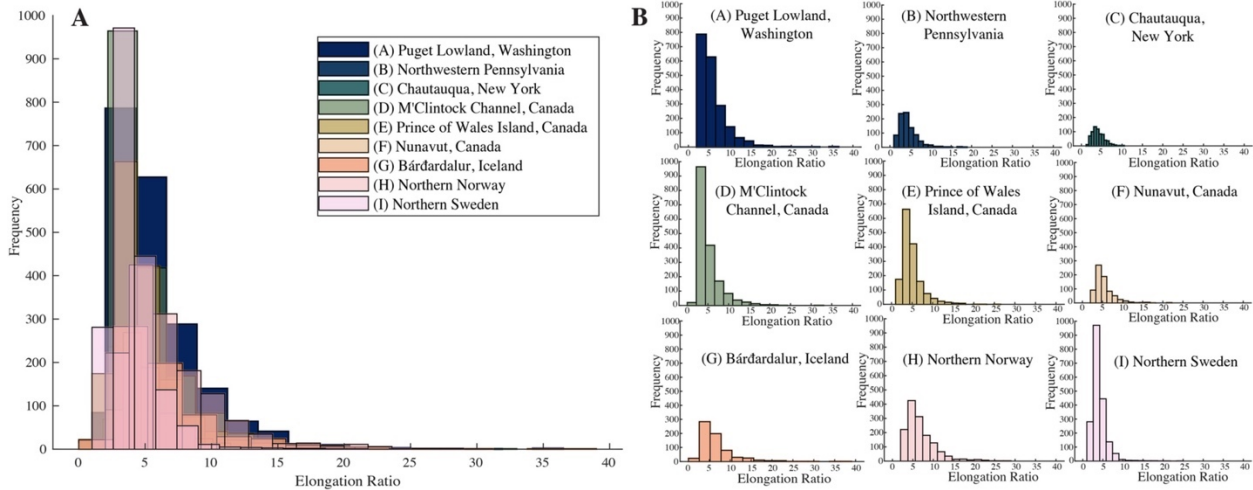


Figure 2.5. Frequency (n) of bedform elongation ratios. (A) Composite histograms of elongation frequencies for each site. (B) Individual site elongation frequencies. Site bins were determined using the “nbins” function in MATLAB, assigning each site 15 bins in order to make frequencies comparable.

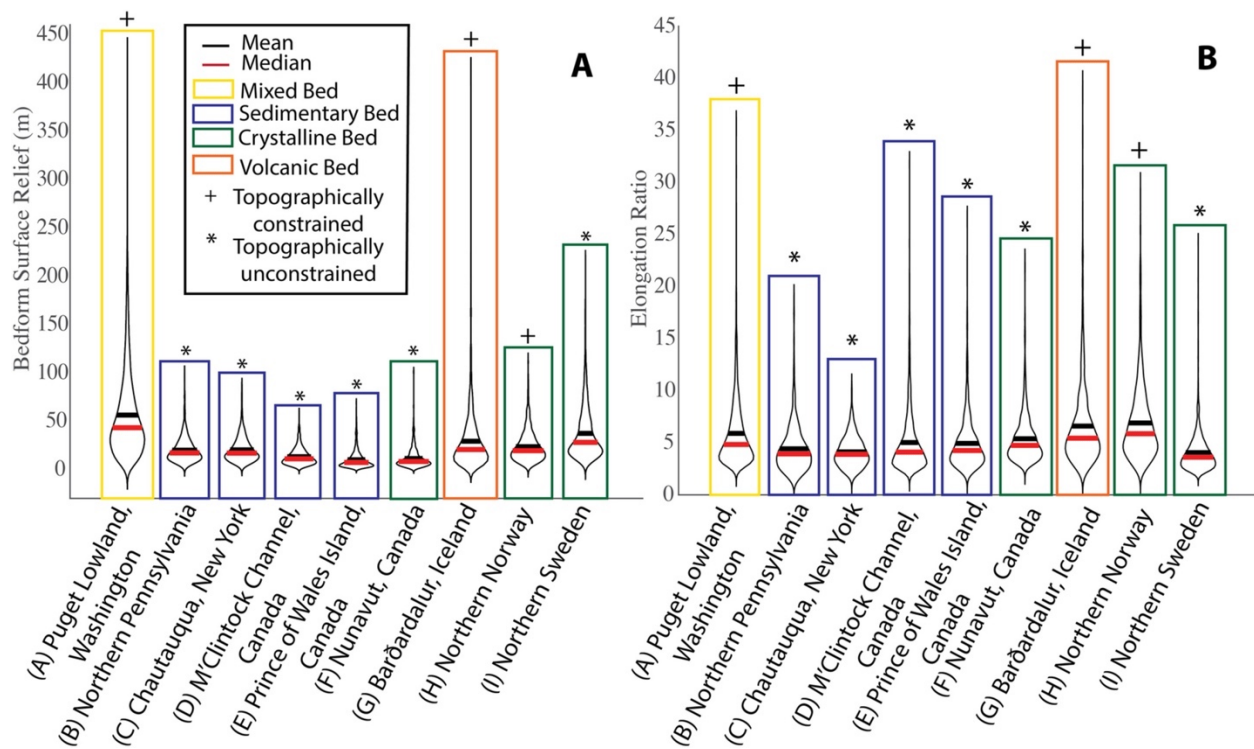


Figure 2.6. (A) Distribution of bedform surface relief range and (B) distribution of bedform elongation ratios by site characterized by topography and bed substrate. MATLAB code for violin plot visualization sourced from Hoffmann (2015).

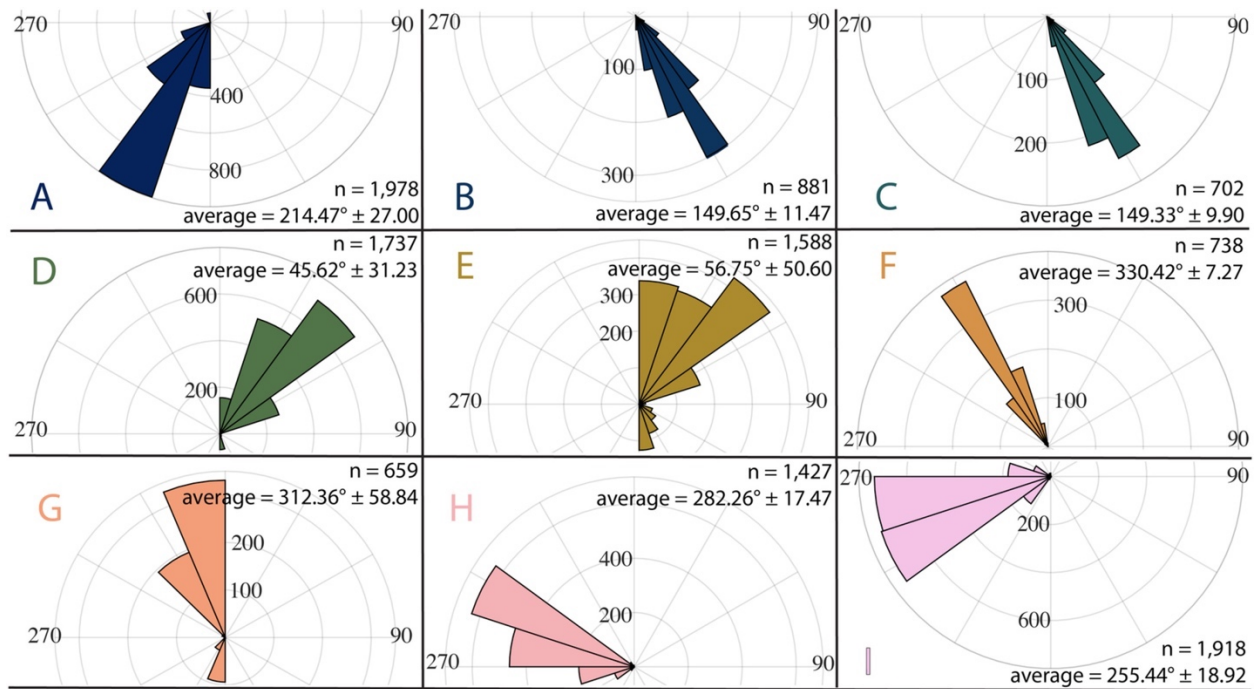


Figure 2.7. Cardinal orientations of mapped bedforms. (A) Puget Lowland, Washington, USA; (B) northwestern Pennsylvania, USA; (C) Chautauqua, NY, USA; (D) M'Clintock Channel, Canada; (E) Prince of Wales Island, Canada; (F) Nunavut, Canada; (G) Bárðardalur, Iceland; (H) northern Norway; (I) northern Sweden.

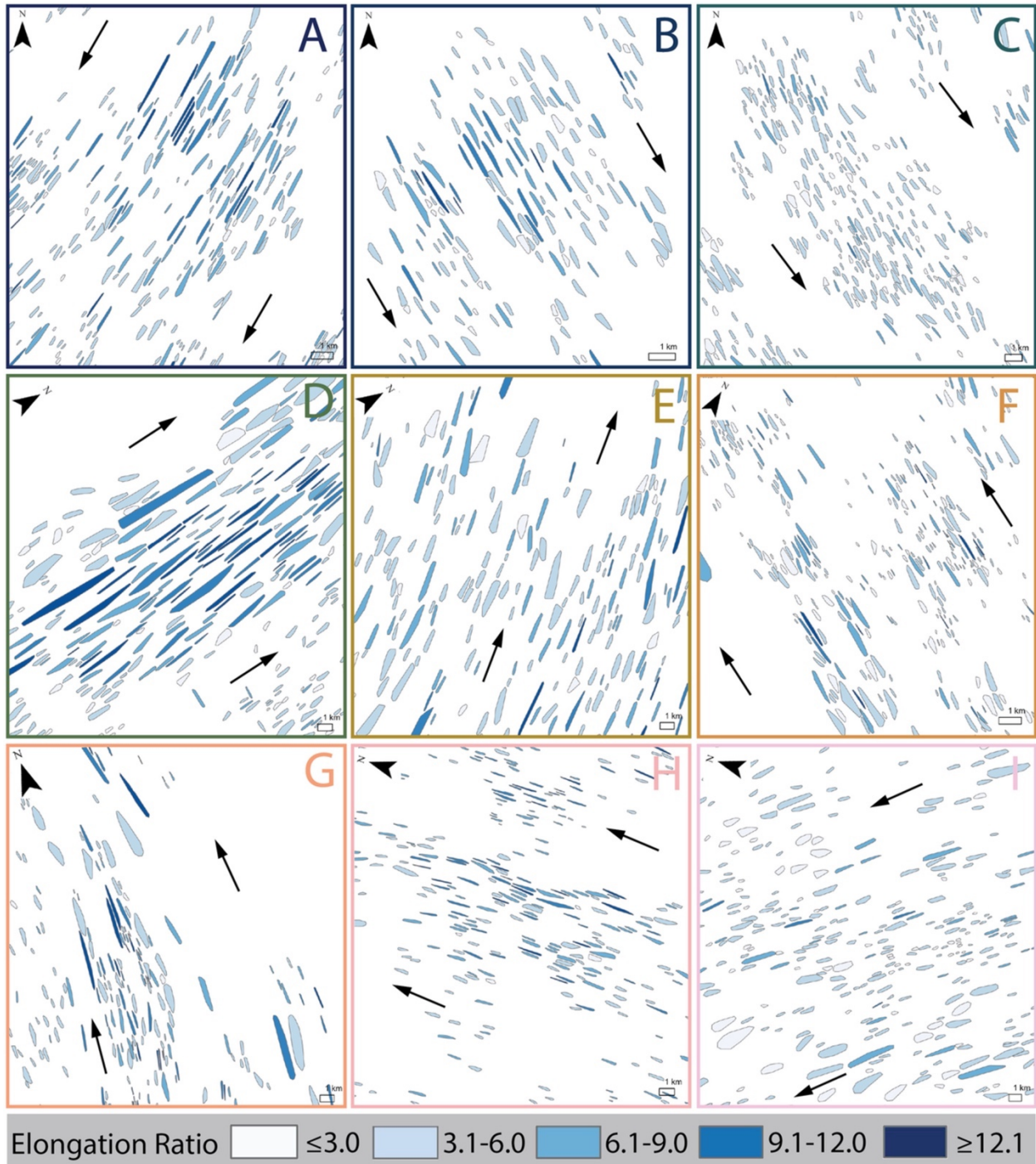


Figure 2.8. Representative bedform elongation ratios at (A) Puget Lowland, Washington, USA; (B) northwestern Pennsylvania, USA; (C) Chautauqua, NY, USA; (D) M'Clintock Channel, Canada; (E) Prince of Wales Island, Canada; (F) Nunavut, Canada; (G) Bárðardalur, Iceland; (H) northern Norway; (I) northern Sweden. Black arrows indicate ice flow direction.

Chapter 3: Differential impact of isolated topographic bumps on glacial ice flow and subglacial processes

Adapted from: McKenzie, M.A., Simkins, L.M., Slawson, J.S., MacKie, E.J., and Wang, S.: Differential impact of isolated topographic bumps on glacial ice flow and subglacial processes, *The Cryosphere*, <https://doi.org/10.5194/egusphere-2022-1220> (preprint).

3.1 Introduction

Isolated topographic highs in the terrain beneath ice sheets can contribute to increased basal drag and decreased ice flow velocity and, for marine-based margins, offer pinning-points to halt or slow down margin retreat (Durand et al., 2011; Favier et al., 2016; Alley et al., 2021; Robel et al., 2022). Conversely, ice flow over topographic highs can increase strain heating and basal meltwater production, elevating basal meltwater pressure and reducing basal friction in the downstream environment (Payne and Dongelmans, 1997; Cuffey and Paterson, 2010). However, identifying which forms and scales of “bumps” across a glaciated landscape may increase, decrease, or not affect ice-flow velocity, basal water pressure, and basal friction is not well understood. Additionally, basal topography at the base of the ice sheet – and even for most glacier catchments – is poorly resolved (e.g., MacKie et al., 2020; Morlighem et al., 2020). Therefore, we turn to a formerly glaciated landscape in Washington state where geomorphological indicators of ice-flow conditions in the form of streamlined subglacial bedforms, such as glacial lineations, whalebacks, and drumlins, can be used to better understand the sensitivity of ice sheets to isolated bumps in the subglacial environment. Morphometrics of streamlined subglacial bedforms offer information on ice-bed interactions and provide an opportunity to assess characteristics of paleo-ice flow organization and relative speeds across a landscape (e.g., Clark, 1997, 1999; King et al., 2009; Clark et al., 2003, 2009; Spagnolo et al., 2012, 2014; Principato et al., 2016). Assessment of streamlined subglacial bedforms and their implications for ice flow are applicable to modern ice sheets (MacKie et al., 2021), where empirical observations of subglacial conditions are spatially (and temporally) limited.

3.1.1 Site Characteristics

The Puget Lowland of Washington state was glaciated by the southwestern Cordilleran Ice Sheet (CIS) during the Last Glacial Maximum (LGM), when the region was largely depressed below sea level due to glacial isostatic adjustment (GIA; Booth and Hallet, 1993; Dethier et al., 1995; Kovanen and Slaymaker, 2004; Eyles et al., 2018); therefore, the southwestern CIS was predominantly marine based. Active tectonics and volcanic activity across the Puget Lowland have led to exposed crystalline and volcanic bedrock of Eocene age interrupting sedimentary bedrock across the region (Khazaradze et al., 1999; Booth et al., 2004). Based on subglacial modeling (Alley et al., 2021), it is highly possible the higher relief crystalline and volcanic bedrock exposures or “bumps” influenced marine and terrestrial-based ice-bed interactions across the Puget Lowland, but this concept has yet to be empirically tested

across the region. The Puget Lowland is a basin surrounded by mountainous terrain near the coast of the Pacific Ocean with isolated topographic highs, similar to the terrain beneath the margins of the Greenland Ice Sheet (Bamber et al. 2013; Eyles et al., 2018). This work aims to determine the role of topographic bumps on glacial ice flow via streamlined subglacial bedform morphology and distribution. By assessing ice flow behavior within a single glacial system, effects of isolated crystalline bedrock highs on ice flow will not be confounded by geographically variable conditions such as local climate and ocean forcings.

3.2 Methodology

3.2.1 Topographic “Bump” Classification

Digital elevation models with horizontal resolution of 1.83 x 1.83 meters and coarsest vertical resolution of 2 meters from across the Puget Lowland (Clallam County, Olympic Department of Natural Resources, WA, 2008; Quantum Spatial Inc., 2017, 2019; OCM Partners, 2019a, 2019b) and ambient occlusion hillshading techniques (c.f., McKenzie et al., 2022) were utilized to assess nine crystalline and volcanic bedrock bumps across the Puget Lowland with a wide range in peak elevation, bump surface area and volume, and topographic setting (Figure 3.1). The outermost 100-foot closed contour across each bump was expanded to three times the surface area to classify the region of interest, following the influence of bump perturbations on basal hydrologic potential by Alley et al., 2021. While present-day elevations of these deglaciated sites differ from elevations during glaciation due to GIA, tectonics, and post-glacial landscape evolution, relative relief and influence of these bumps on the presence of streamlined bedforms is well preserved. Fractures, faults, and joints from tectonic activity and brittle deformation of the crust across bumps are below the scale of analysis for this work and are therefore not considered here.

3.2.2 Streamlined subglacial bedform identification

Streamlined subglacial bedforms were identified across the nine bump sites using a combination of Topographic Position Index (TPI) analysis (McKenzie et al., 2022), contour-tree mapping (Wang et al., 2017), and manual identification. TPI utilizes DEM slope variations across defined cell-neighborhood sizes to semi-automatically identify positive relief features (McKenzie et al., 2022). Localized contour-tree mapping utilizes DEM data to isolate closed contours within a defined elevation (Wang et al., 2017). Both tool outputs were validated and corrected if needed by manual removal of incorrectly identified features and manual addition of bedforms missed by the automated tools. All bedforms in the final dataset (n=3,273) have an associated long-axis length, cardinal orientation, width orthogonal to long-axis length, and range in elevation across the long axis calculated by the ArcGIS Pro “Minimum Bounding Geometry” and “Add Z Information” tools (McKenzie et al., 2023). For each site, bedforms were

categorized into groups “upstream”, “on top of”, and “downstream” as determined by bedform location with respect to the outermost 100-foot contour of the topographic high. Bedforms identified “downstream” of bumps include bump-lateral features. Long axis cardinal direction, or orientation, of streamlined bedforms is used to infer direction of ice flow (Clark, 1997; Kleman et al., 2006; Kleman and Borgström, 1996). Bedform elongation ratio, calculated by dividing a bedform’s length by its width is used to infer relative speed of ice flow velocity (Clark 1997, 1999; Clark et al., 2003) and relative duration of ice presence in a region (Benediktsson et al., 2016). Bedform surface relief, the difference between the highest and lowest elevation along the bedform long axis, is used to infer maturity of ice flow and sedimentary processes in the subglacial environment, where smaller surface relief values indicate more mature sedimentary processes in the subglacial environment than larger values (McKenzie et al., 2022). We performed analysis of variance (ANOVA) and non-parametric Kruskal-Wallis tests to compare the statistical significance of the means and distributions between populations, respectively, in “R”. Results of statistical analyses were used to determine significance of bedform characteristics at each site (i.e., upstream, on top of, and downstream of bumps) as well as significance of bedform morphometrics across sites.

3.3 Results and Discussion

The number of streamlined bedforms per site is positively correlated with site surface area and volume (Figure 3.1B), indicating spatial continuity in the bedform distribution across the Puget Lowland. On top of all bump sites, bedform elongation for the full dataset ($n = 3,273$) is lowest and bedform surface relief is highest (Figure 3.2). We, thus, interpret that bumps in the subglacial environment of the Cordilleran Ice Sheet generally led to ice-flow deceleration and reduction of efficiency or spatial homogeneity of sedimentary processes including bedrock erosion and sediment transport and deposition – all of which are important for bedform genesis (Schoof and Clark, 2008; Shaw et al., 2008; King et al., 2009). While bedform surface relief and elongation ranges overlap across all site populations, bedforms associated with smaller bumps tend to have outliers below the 1σ (68%) confidence level for all populations (e.g., San Juan Island, Fidalgo Island, and Black Hills) while those associated with larger bumps have outliers above the 1σ confidence level (e.g., Blue Hills and Cougar Mountain; Figure 3.2). This trend in outliers demonstrates a linkage between bump size and possible bedform morphometrics in a relatively systemic manner across the Puget Lowland. Notably, there is a significant decrease in bedform elongation between upstream and on top of the two largest bumps (Figure 3.3A), Blue Hills and Devils Mountain, suggesting bump volume larger than 4.5 km^3 significantly slows or causes disorganization in ice flow (Figure 3.1B; Clark 1997, 1999; Clark et al., 2003).

At seven of the nine sites, surface relief along bedform crests increases significantly between populations upstream and on top of bumps (Figure 3.3B), most likely due to a transition in subglacial lithology from sedimentary to crystalline or volcanic bedrock, disrupting sedimentary processes as ice contacted more-erosion-resistant bed compositions. The two

exceptions to this trend are Big Skidder Hill and Lopez Island, where there is no appreciable change in streamlined subglacial bedform surface relief across the bumps (Figure 3.3B); therefore, suggesting that conditions at these two sites were able to overcome direct lithologic impact on bedform relief. Due to the more-erosion-resistant lithologies of the bumps, combined with increased pressure and basal drag in the subglacial environment, there is decreased homogeneity in bedform relief, indicating reduced efficiency in which the ice is able to facilitate streamlined subglacial bedform formation through bedrock erosion (Eyles and Doughty, 2016; Krabbendam et al., 2016), leading to truncated bedforms with high surface relief (McKenzie et al., 2022; Figure 3.2). We postulate that bump size – through its impact on ice flow and subglacial processes – is a major control on bedform surface relief, where the greatest proportion of bedforms with low surface relief (Figure 3.4B) are located at the smallest bump sites ($< 0.2 \text{ km}^3$). Increased sediment availability and basal meltwater that results from the strain heating on top of the bump (Payne and Dongelmans, 1997), increases downstream sediment transport efficiency (McIntyre, 1985; Pohjola and Hedfors, 2003; Winsborrow et al., 2010b), resulting in the greatest number and most elongate bedforms, as well as the greatest proportion of bedforms with low surface relief, downstream of bumps (Figure 3.1A; Figure 3.2; Figure 3.4A, 3.4B).

While many sites showcase an increase in disorganization of bedform orientation on top of the bump, only at the two largest bumps ($> 4.5 \text{ km}^3$) does downstream bedform orientation recover to patterns present in the upstream bedform populations (Figure 3.4C). The rest of the sites have bedform orientations that either remain unchanged or become more disorganized downstream (Figure 3.4C). From these findings, we infer a bump volume of $\sim 4.5 \text{ km}^3$ will influence reorganization of downstream ice-flow orientation and subglacial sedimentary processes, while bumps below this threshold cannot regain the same organization seen upstream of bumps. This analysis found no evidence of channelized meltwater in the subglacial environment, potentially suggesting meltwater development across these bumps was distributed and saturated, which would explain the homogeneity in bedform formation observed in bedforms downstream of bumps.

Overall, there is general ice flow deceleration and reduction of bedrock erosion on top of bumps, which results from a subglacial lithology transition. Sedimentary processes, essential to streamlined bedform genesis, are most organized and efficient downstream of bumps - likely as a result of increased sediment availability and subglacial meltwater sourced from strain heating on top of the bump. The largest sites notably disturb ice-flow orientation and speed on top of the bump with only bumps larger than $\sim 4.5 \text{ km}^3$ indicating recovery of ice flow orientation and speed downstream of bumps. Findings from these paleo-subglacial bumps may be used as an analog for ice flow in contemporary ice sheets and support process-based understanding of subglacial terrain influence on overlying ice-sheet behavior in similar systems.

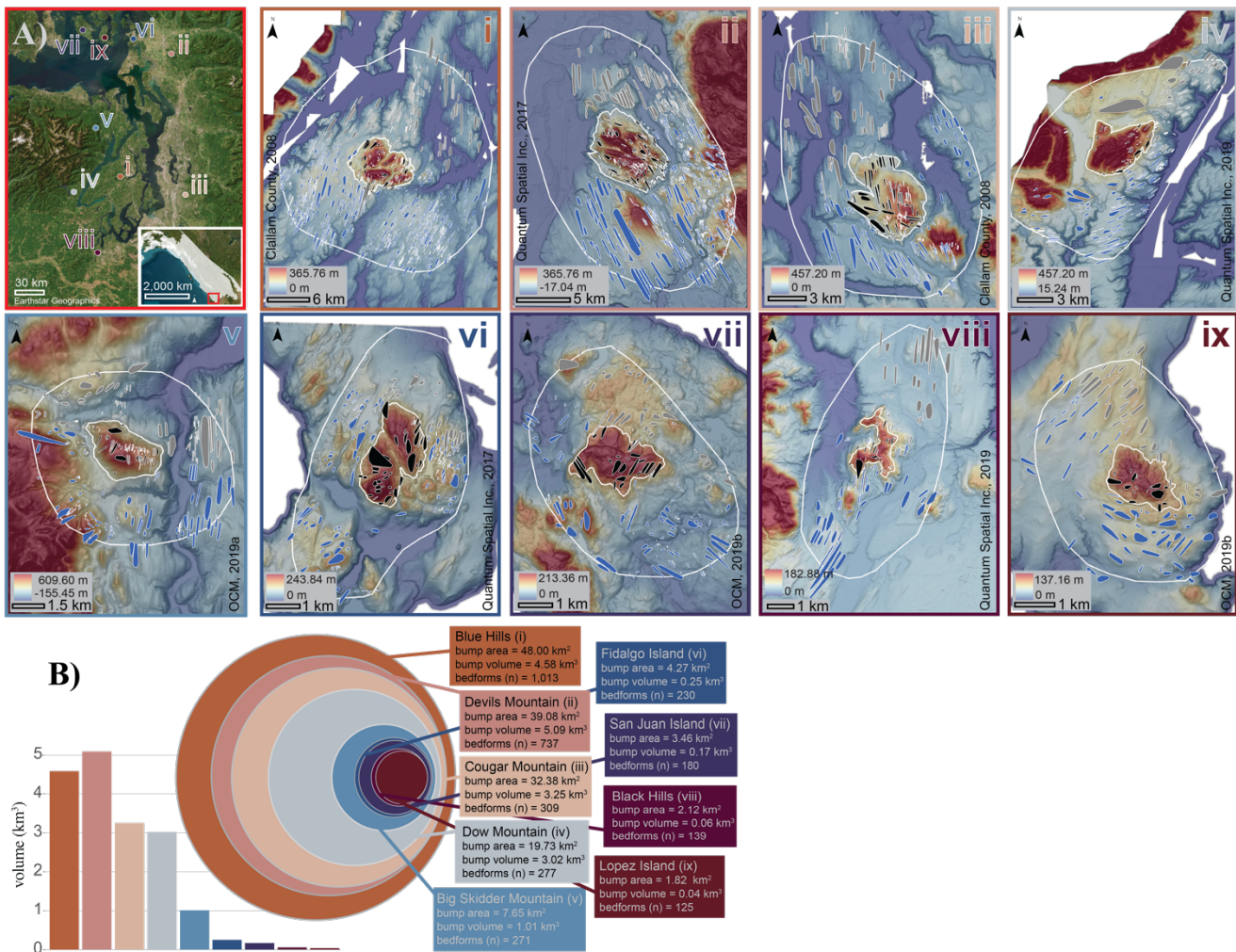


Figure 3.1. A) Site overview across the Puget Lowland with inset reference of CIS glaciation (14 kya; Ehlers et al., 2010). Site maps for i) the Blue Hills, ii) Devils Mountain, iii) Cougar Mountain, iv) Dow Mountain, v) big Skidder Mountain, vi) Fidalgo Island, vii) San Juan Island, viii) the Black Hills, and ix) Lopez Island. Streamlined subglacial bedforms are mapped upstream (gray polygons), on top of (black polygons), and downstream (blue polygons) of bed bumps (small white outlines) within larger site regions (large white outlines). B) Relative volume and surface area of bed bump sites.

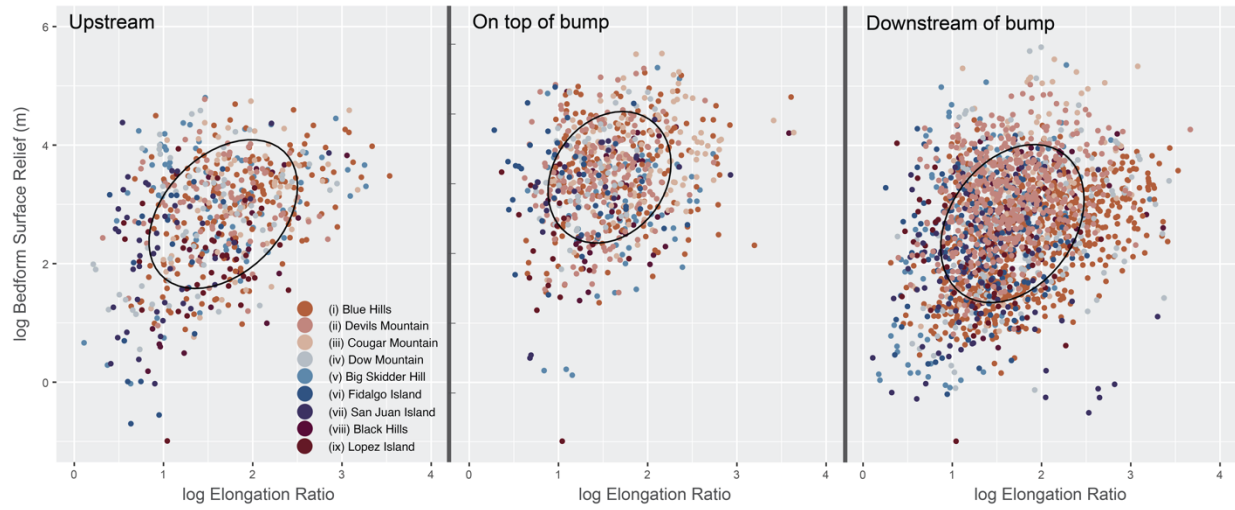


Figure 3.2. Scatterplots of the log of bedform elongation ratio and surface relief in meters. The ellipses are 1σ (68%) confidence levels for multivariate t-distributions for all bedforms ($n=3,273$). Sites are listed in the legend from largest surface area ((i) Blue Hills) to smallest surface area ((ix) Lopez Island).

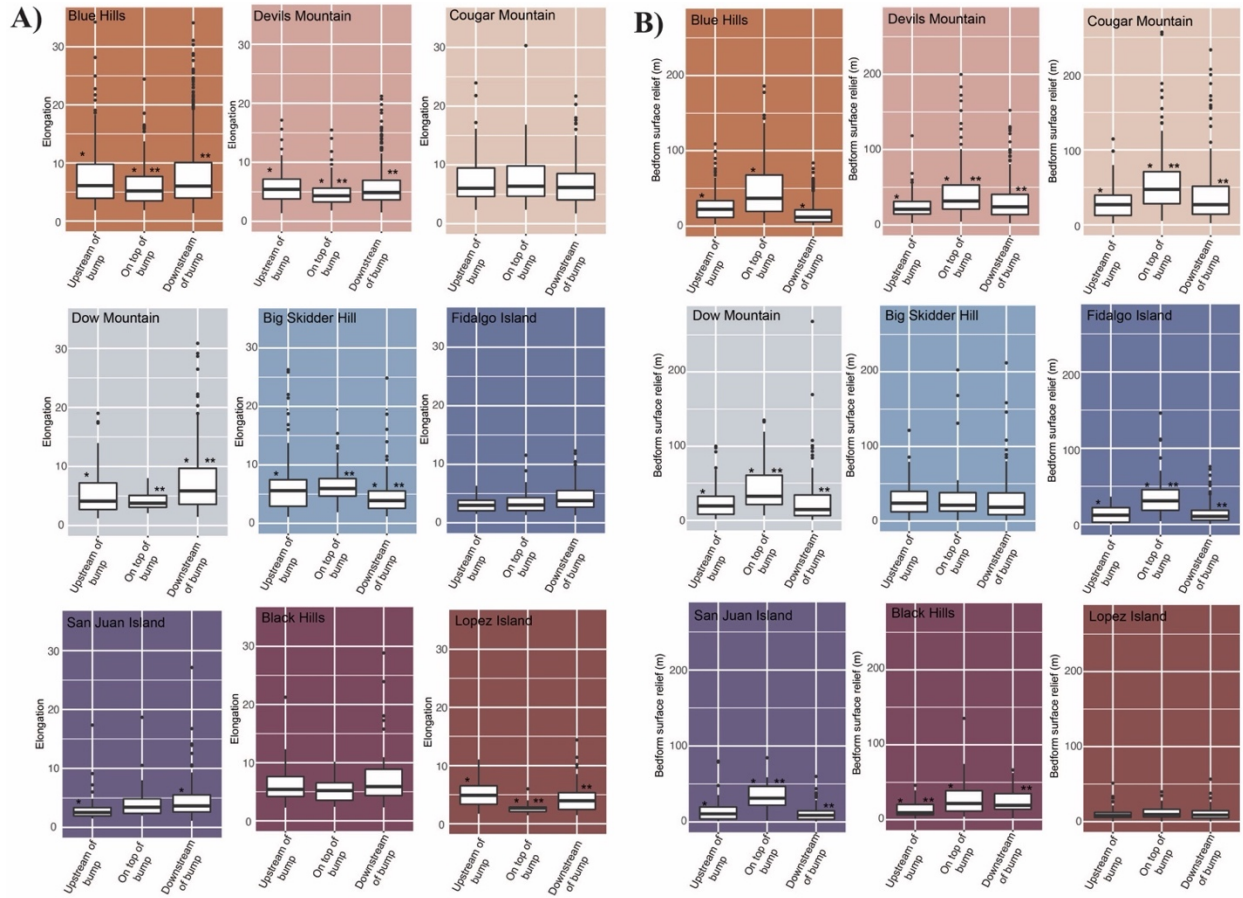


Figure 3.3. Box plots of A) bedform elongation data at each site with populations characterized upstream of, on top of, and downstream of bumps and B) surface relief data at each site with populations characterized upstream of, on top of, and downstream of bumps. Statistically significant differences between groups are indicated by asterisks. Multiple asterisks indicate a separate population with significant differences, independent from other groups of statistical significance.

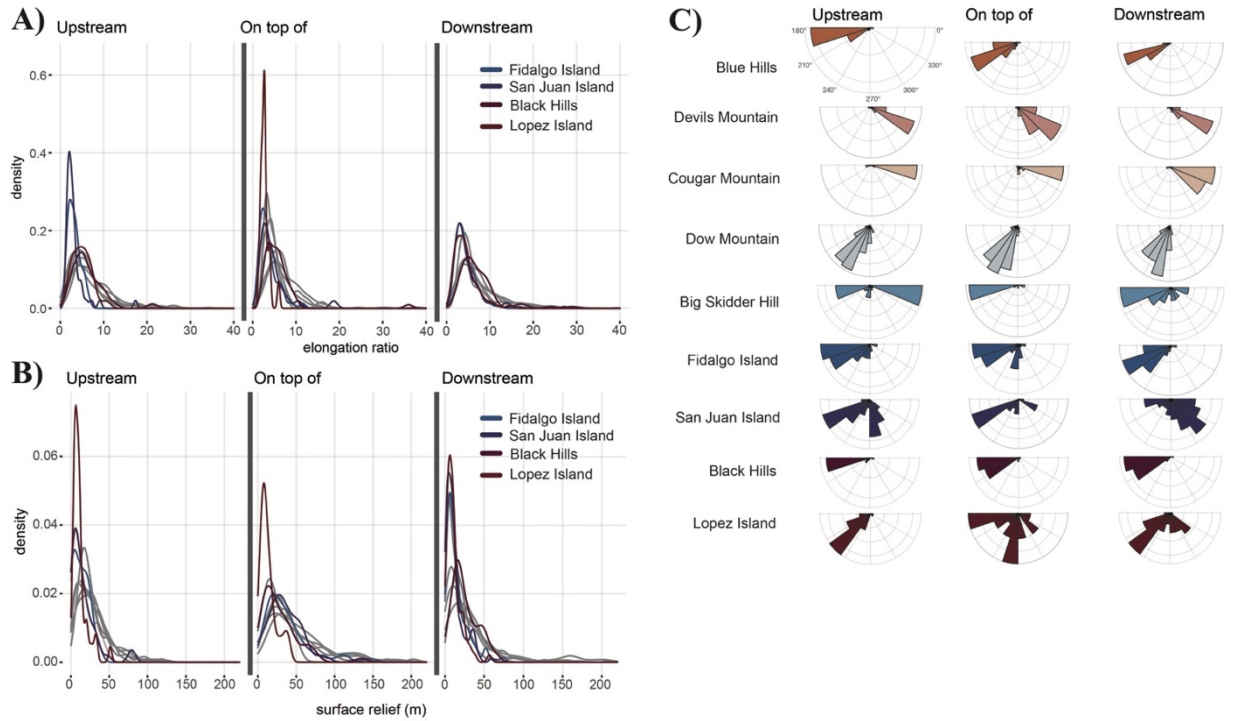


Figure 3.4. A) Density curves of bedform elongation upstream, on top of, and downstream of nine bumps. Density curves with color are less than 4 square kilometers, all other sites are shown in gray. B) Density curves of bedform surface relief in meters upstream, on top of, and downstream of nine bumps. Density curves with color are less than 4 square kilometers in surface area, all other sites are shown in gray. C) Cardinal orientations of streamlined bedforms upstream, on top of, and downstream of nine bumps.

Chapter 4: Outcrop perspectives on spatial and temporal effects of topography on the marine-terminating Puget Lobe of the Cordilleran Ice Sheet

Conducted with support from: Lauren M. Simkins, Allison P. Lepp, and Regina DeWitt. Work currently in preparation for submission to *Geology* or *Sedimentology*.

4.1 Introduction

While the extinct Cordilleran Ice Sheet (CIS) is the least understood of all Pleistocene ice sheets, constraining parts of this ice system may elucidate subglacial processes relevant to contemporary ice sheets. The southernmost part of the CIS, the Puget Lobe, was marine terminating and resided in a topographic basin not unlike the topography beneath modern outlet glaciers in Greenland (Figure 4.1; Eyles et al., 2018). The Puget Lowland of Washington state has been glaciated at least six times throughout the Quaternary as a result of southernmost CIS advance and retreat in the region. Glaciations occurred in marine isotope stage (MIS) 6 (~97,000 to 150,000 years ago; Easterbrook, 1969), MIS 4 (80,000 ± 20,000 years; Easterbrook et al., 1967; Easterbrook, 1969), and towards the end of MIS 2 (~17,500 cal. year BP; Mullineaux et al., 1965; Porter & Swanson, 1998). Existing geochronology data places final deglaciation of the Puget Lowland around 16,500 calendar years BP (Easterbrook, 1992; Dethier et al., 2005; Swanson & Caffee, 2001). The poorly recorded stratigraphic context and a lack of marine reservoir correction (MRC) for this region leave uncertainties in this timing of ice retreat. During final retreat, it is suggested a marine incursion led to rapid lift-off and retreat of the Puget Lobe from the region (Thorson, 1980, 1981; Waitt and Thorson, 1983; Booth, 1987; Booth et al., 2003). However, variable records of deglacial stratigraphy across the region (Powell, 1980; Pessl et al., 1981; Domack, 1984; Demet et al., 2019) and ice-marginal landforms indicate periodic stand-still in ice margin location during marine retreat (Simkins et al., 2017; Demet et al., 2019). Previous interpretations of Puget Lobe retreat style were not made within the context of modern understandings in glacial dynamics, high resolution stratigraphic mapping, nor geomorphological context for the greater region, leaving uncertainty in and prompting a revisitation of the plausibility of these hypotheses.

The magnitude of landscape emergence due to glacial isostatic adjustment (GIA) in the Puget Lowland is also poorly constrained, but is cited to have been as high as 10 cm per year during early deglaciation (Dethier et al., 1995). This rate of GIA-induced uplift suggests relative sea-level fall outpacing eustatic sea-level rise, leading to emergence of the landscape from below sea level (Shugar et al., 2014; Yokoyama & Purcell, 2021). Additionally, both pre-existing topography and GIA could have periodically stabilized the Puget Lobe during retreat, as suggested for contemporary ice sheets (Durand et al., 2011; Favier et al., 2016; Alley et al., 2021; Robel et al., 2022), highlighting the importance of constraining the role GIA-induced landscape emergence has on ice sheet behavior.

The preserved stratigraphy along the coastal bluffs in the Puget Lowland, Washington state, specifically Whidbey Island, provide the opportunity to assess temporal and spatial

variability in marine ice-sheet behavior and coupled submarine-to-subaerial landscape evolution. Whidbey Island hosts a large amount of coastal bluff features located in the central Puget Lowland and spans nearly 100 kilometers in distance along the North-South direction of glacial ice movement. The outcrops, comprised of glacial and interglacial sediments, preserve direct records from ice advance and retreat across the formerly marine landscape, as well as landscape transitions that took place coeval with deglaciation. With the exception of active tectonic deformation of sediments (Sherrod et al., 2008), local LGM and subsequent deglacial deposits appear to have little post-depositional reworking as evidenced by preservation of coastal outcrops and surficial glacial landforms (Booth & Hallet, 1993; Kovanen & Slaymaker, 2004; Eyles et al., 2018; Demet et al., 2019; McKenzie et al., *preprint*). The ice histories and solid Earth properties, such as flexural thickness of the lithosphere and mantle viscosity or rheology, that control vertical-landscape evolution in this region are similar in the Antarctic Peninsula (Whitehouse et al., 2019; Nield et al., 2014). Aside from the process-based relevance to modern systems, constraining timing of CIS ice retreat from the Puget Lowland has implications for timing of ice contribution to global sea level as well as routes and timing of human migration into the Americas (Mandryk et al., 2001; Goebel et al., 2011; Lesnek et al., 2018). Therefore, the remnant material deposited by the southernmost CIS is uniquely poised to answer questions relating to topographic controls on marine-terminating ice in similar topographic and rheological settings (Bamber et al., 2013; Eyles et al., 2018; Whitehouse et al., 2019; Nield et al., 2014).

The decimeter-scale stratigraphic and sedimentological assessment conducted in this work is complemented by accelerator mass spectrometry radiocarbon (^{14}C) and optically stimulated luminescence (OSL) dating. While these two dating methods have been utilized in this region for decades (e.g., Rigg and Gould, 1957; Leopold et al., 1982; Easterbrook, 1992; Anundsen et al., 1994; Dethier et al., 1995; Swanson and Caffee, 2001), the timing of landscape emergence in relation to ice retreat and periodic stabilization of ice retreat had still not been assessed using modern knowledge from the fields of glaciology, sedimentology, and geochronology. Therefore, the application of modern advances in geochronology, paired with a high-resolution stratigraphic assessment of Whidbey Island is a novel approach to constraining the ice retreat and land emergence across the region.

4.2 Methodology

4.2.1 Sedimentology and stratigraphy

Samples were collected from Whidbey Island outcrops a) Double Bluff, b) Fort Casey, c) Penn Cove, d) West Beach, and e) Cliffside at 10-cm intervals (Figure 4.2; Table 4.1) with additional subsamples collected from units with laminations, lenses, or intrusions. More continuously deposited layers are referred to as laminations, while less continuous material is referred to as a lens. For example, this difference can be seen between the clay laminations of Unit 3 and the clay lenses of Unit 1 at Fort Casey Site 1 (Figure A4.1). Over 300 discrete bulk

sediment samples were analyzed at the University of Virginia for grain size, trace element composition, and magnetic susceptibility. An additional 15 peat, wood, and marine shell samples were excavated for radiocarbon dating. (e.g., Figure 4.3). Grain size and shape analyses were conducted via a BetterSize S3 Plus Particle analyzer on sample matrix material (material ≤ 2 mm), trace element analysis was conducted with a handheld Niton XLF X-ray fluorescence (XRF) machine, and magnetic susceptibility (MS) measurements were collected with a Bartington MS2 magnetic susceptibility meter. Trace element results are presented with a focus on terrestrially sourced elements Ti and Fe and variably sourced Ca (Rothwell and Croudace, 2015). MS values provide information about amount and size of magnetic grains in each sample, elucidating continuity and source of biogenic and lithogenic deposits (Thompson and Oldfield, 1986; Verosub and Roberts, 1995; Rosenbaum, 2005; Hatfield et al., 2017; Reilly et al., 2019). Results of the Whidbey Island stratigraphy are presented according to latitudinal location, starting with the southernmost site, Double Bluff, followed by the Fort Casey Sites, Penn Cove, West Beach sites, and ending with the northernmost Cliffside and Rocky Point sites.

4.2.2 Accelerator Mass Spectrometry Radiocarbon Analysis

Assuming a constant cosmically produced ^{14}C to ^{12}C ratio, the variation in this ratio can be used to determine the amount of time since the death of formerly living specimens. Samples were run by M. McKenzie with supervision and support from the National Oceanographic Sciences Accelerator Mass Spectrometry Laboratory Graduate Student Internship at Woods Hole Oceanographic Institute. The unprocessed wood material underwent a series of six to eight acid-base-acid leaches to remove contamination and inorganic carbon prior to combustion. The carbonate shell samples were dissolved with acetic acid, and the resulting CO_2 gas from both the carbonate hydrolysis and organic carbon combustion reacted with Fe catalyst along vacuum-sealed lines to produce graphite (Goehring et al., 2019). Resulting graphite pellets were pressed into targets and analyzed by accelerator mass spectrometry in addition to standard and processing blanks (Roberts et al., 2019). The AMS measurements determined the ratio of ^{14}C to ^{12}C in each of the pellets, which was then used to calculate the radiocarbon age using the Libby ^{14}C half-life of 5,568 years (Stuiver and Polach, 1977; Stuiver, 1980).

Conversion of radiocarbon years to calendar years BP was conducted using the Int20 curve for terrestrial carbon samples and the Marine20 curve for marine shell samples within the Calib 8.2 interface. Marine20 is the baseline marine curve used for Calib 8.2 and is the most up-to-date, internationally agreed marine radiocarbon age calibration curve for non-polar global-average marine records (Heaton et al., 2020) A marine reservoir correction was calculated in Calib 8.2 and applied to all carbonate shell samples using contemporary shells with known pre-1955 (i.e., prior to nuclear bomb testing) collected dates from the Burke Museum in Seattle, Washington. The modern (pre-1955) shells from the Burke Institute range in beach-front collection date from 1911 to 1931 (Table 4.2) and include species *Modiolus rectus*, *Musculus niger*, *Cardita ventricas*, *Macoma carlottensis*, *Mya arenaria*, and *Macoma nasuta*. The radiocarbon ages calculated from these specimens range from 815 ± 15 to 925 ± 20 ^{14}C years.

Utilizing the marine reservoir correction curve developed by Calib 8.2, an average marine reservoir correction for this region was found to be 264 ¹⁴C years (50 calendar years BP). While there is a range of marine reservoir effects between 211 and 318 ¹⁴C years, a species-specific effect has yet to be definitively seen (Table 4.2).

4.2.3 Optically Stimulated Luminescence

In depositional environments, sediments are exposed to radiation in the form of gamma, beta, and alpha rays from cosmic exposure and the presence of in situ uranium (U), thorium (Th), and potassium (K) (Rhodes, 2011; Duller, 2015). Quartz and feldspar grains with crystal structure deformities incorporate this radiation by trapping electrons excited by incoming radiation, with the amount of electrons trapped increasing over time (Rhodes, 2011). Feldspar grains have higher sensitivity to OSL than quartz grains and have higher dose saturation levels (Rhodes, 2011). Fading occurs when feldspars naturally lose signal through time without resetting (Wintle, 1973), which can lead to an age underestimation. Additionally, K-feldspar has internal dose rates, adding to complexity of contamination (Rhodes, 2011). Therefore, feldspar fading and internal dose-rate from K-feldspar need to be corrected for in some samples. The amount of radiation per year that accumulates in an in situ quartz or feldspar grain can be determined through gamma spectrometry and cosmic dose calculations (Rhodes, 2011; Duller, 2015).

Light, pressure, and heat allow the trapped electrons to escape from the traps, and the quartz and feldspar grains emit luminescence (Duller, 2015; King et al., 2014). When an aliquot of sample, buried for an unknown amount of time, is exposed to a known amount of light in a controlled environment, the luminescence signal can be measured. Through a series of tests to correct for error and variation in aliquots, the equivalent dose, or the total energy accumulated during burial as determined through lab measurement of sample luminescence, divided by the dose rate, or the energy delivered each year from in situ radioactive decay and cosmic accumulation, will provide an age since burial date (Duller, 2015).

Using OSL dating in glacial environments presents challenges due to the potential of OSL signal not being fully reset between transport and deposition (Wallinga and Cunningham, 2015). Additionally, extensive overburden pressure from glacial ice has the potential to partially or completely reset OSL signatures, which could provide large error to the final OSL stage (King et al., 2014). Additionally, both past and present water content in the sedimentary deposits are important to consider as water in pore spaces between grains can scatter or absorb radiation, which would result in an improper representation of sample exposure to in situ radiation. Subglacial environments, especially those under ice streams, have a presence of significant meltwater which can saturate sediment pore space and influence quartz and feldspar exposure to radiation at the time of and for an extended period of time after deposition (Wallinga and Cunningham, 2015; Duller, 2013).

With these challenges in mind, my sample collection strategy included the collection of substantial gamma sample from the unit in which the OSL sample was taken. Modern water content was measured and inferred from the history of the region, and a smear-slide mineralogical analysis was conducted to determine amount and type of feldspar contamination, allowing for error corrections to be made to these samples.

4.2.3.1 Sample collection and preparation

Optically stimulated luminescence samples were taken from stratigraphic units with coarse-grain quartz material that mark a transition in depositional environment. Before collection, the exposed surface of the sample site was removed. In order to avoid pre-mature bleaching of sample collection in the field, the OSL samples were collected before sunrise or after sunset and were only exposed to low energy red light. Samples were wrapped in dark black plastic to protect them from light and transported to East Carolina University (ECU) for preparation and processing.

Samples were prepared for OSL analysis under dark-room conditions at ECU using standard coarse-grain procedures: samples were wet-sieved at 90-125 μ m with some expansion to grain sizes of 63-212 μ m. After drying the samples at 50°C, the samples were treated with 10% hydrochloric acid (HCl) to remove carbonates and rinsed with DI water. Then the samples were treated with 29% hydrogen peroxide (H₂O₂) to remove organics and rinsed with DI water.

A high-density separation was conducted with lithium heteropolytungstate (LST) at a density of 2.72-2.75 g/cm³ to isolate quartz grains. Coarse grains were etched for 40 minutes with 48% hydrofluoric acid (HF) to remove outer parts affected by alpha radiation, followed by a 10% HCl rinse to remove fluoride precipitates. A low-density separation to isolate quartz from feldspar was conducted with LST at a density of 2.62 g/cm³. After final sieving, the aliquots were prepared by using Reusch Silkospray to adhere material to the stainless steel sample cups. Samples were placed in metal cup holders labeled with position numbers. The hydrometers used to measure the density of the LST later proved to be faulty. Thus, the quartz extracted from the samples show contamination with feldspar. However, smear slide mineralogical assessment of samples allowed for feldspar classification as K-feldspar, leading to feldspar corrections in final calculations.

Bulk sediment was provided for gamma spectrometry and stored in plastic containers for at least 4 weeks prior to measurement. While the OSL samples were taken at unit boundaries, the dose rate samples were taken from the same unit as the OSL samples. Therefore, the gamma dose rates reflect the sample unit only and contain no information about adjacent, underlying, or overlying units.

4.2.3.2 Dose measurements

Dose measurements were conducted using a Risø TL/OSL-DA-20 reader manufactured by Risø National Laboratory with a bi-alkali PM tube (Thorn EMI 9635QB). The built-in $^{90}\text{Sr}/^{90}\text{Y}$ beta source gives a dose rate of ~ 100 mGy/s. The exact dose rate value was calculated for the specific day on which each sample was measured. Optical stimulation was carried out with an IR LED array at 870 nm with 121 mW/cm² (90%) power at the sample, a blue LED array at 470 nm with 74 mW/cm² (90%) power at the sample and a 7.5 mm Hoya U-340 detection filter (290-370 nm; Bøtter-Jensen & Murray, 1999).

Equivalent doses were determined following the single-aliquot regenerative dose (SAR) procedure developed by Murray and Wintle (2000) and Wintle and Murray (2006). Due to the feldspar contamination, a post-IR procedure was used to isolate quartz signals in the equivalent dose measurements (Wallinga et al., 2002). The preheat temperature of 180°C for 10 s was determined for each sample using plateau and dose recovery tests (Figure 4.4). Our specific measurement protocol is outlined in Table 4.3.

Luminescence signals L_i and T_i were determined by integrating over the first 0.8 seconds of an OSL decay curve and subtracting an average of the next 4 seconds as background signal. The signal uncertainty followed from counting statistics. The sensitivity corrected signal is given by $C_i = L_i/T_i$. The dose response of every aliquot was determined by fitting the luminescence signals C_1 to C_5 with a saturating exponential. The dose D_0 corresponding to the natural sensitivity-corrected luminescence signal C_0 , was calculated with the fitting parameters. All uncertainties were calculated using the Gaussian law of error propagation and Poisson statistics.

The vast majority of aliquots passed the reliability test – requiring recycling ratios between 0.9 and 1.1, dose recovery $<10\%$ deviation from given dose, low recuperation. The equivalent dose D_e was determined for each site using the central age model (Galbraith, 1999). The full uncertainty also includes 3.1% for the built-in beta source error.

4.2.3.3 Dose rate

In the sediment, grains are exposed to natural gamma and beta radiation from uranium, ^{232}Th , and potassium. The concentrations of these radionuclides were measured with high resolution gamma spectrometry. All samples were in radioactive disequilibrium. Uranium concentrations determined from ^{234}Th were all significantly higher than concentrations determined from ^{214}Pb and ^{214}Bi . We assumed that ^{234}U was leached out of the sample due to in situ water presence.

Dose rates were calculated by using the actual measured concentrations for the nuclides in the uranium decay chain. Uncertainties were calculated based on the maximum and minimum values obtained from the measured concentrations of ^{234}Th and $^{214}\text{Bi}/^{214}\text{Pb}$. Water contents were very low and have an uncertainty of 5% (Table 4.4). Beta and gamma dose rates were calculated using the conversion factors published by Guérin et al. (2011).

The cosmic dose rate was calculated as described by Barbouti and Rastin (1983), Prescott and Stephan (1982), and Prescott and Hutton (1994) and incorporates site latitude, longitude, site

altitude, and sample depth below surface. The effective thickness was assumed to be half the burial depth with an uncertainty of 5%.

4.2.3.4 Age determination

The sample ages, calculated in calendar years, were calculated by dividing the dose by the dose-rate (Table 4.4). Due to feldspar contamination in some samples, fading was measured with a post-IR blue sequence for all samples. Only some of the samples showed fading. For those, the ages were corrected as suggested by Auclair et al. (2003). While ^{14}C ages are reported in kilo years ago (kya) calendar year BP (1955), all OSL ages are reported in kya based on the date of collection (2020). OSL ages in kya can be converted to kya cal. BP by removing 65 years from the final age.

4.3 Results

4.3.1 Double Bluff

The stratigraphically lower-most unit visible at Double Bluff, Unit 4, is a well-sorted sand with sparse rounded gravel lenses. Unit 4 is normally graded with clasts ranging from granule to pebbles with a consistent horizontal long-axis orientation and some silt rip-ups from underlying units. A gradational boundary leads into the overlying sandy silt and fine clayey silt of Unit 3. This unit contains wavy laminations and woody debris dated to be 48.0+ thousand years (kya) cal. BP (i.e., “radiocarbon dead”). Unit 3 generally fines upwards but with many, variable matrix grain size modes between 10 and 500 microns (Figure 4.5A). Unit 2 is composed of massive diamicton with a clay and fine-silt matrix, marked by a matrix grain size mode of 8 microns and a mix of angular and rounded granule to cobble-sized clasts without a preferred long-axis orientation. There is a gradational contact between Unit 2 and Unit 1. Unit 1 consists of variable diamicton between sandy silt and silty sand with woody debris dated to 48.0+ kya cal. BP in age (i.e., “radiocarbon dead”) and clasts that are predominantly aligned parallel to bedding and evidence of soft-sediment deformation (i.e., rapid sediment deposition and/or loading). This uppermost unit has interbedded silt and clay, as well as shells in the upper 50 cm of silt that were inaccessible to sampling. In Units 4, 2, and 1, iron (Fe), titanium (Ti), and calcium (Ca) follow similar trends. Unit 3 has discrete peaks in Ti and Fe that correspond to lows in Ca and magnetic susceptibility (MS) values (Figure 4.5B).

4.3.2 Fort Casey

The lower-most visible unit, Unit 3, at Fort Casey Site 1 consists of massive diamicton with a fine-silt and clay matrix and randomly oriented pebble to cobble-sized angular and rounded clasts. Interbedded with the massive diamicton are discrete gravel and sand laminations

at the base of Unit 3 and silt and clay laminations with rip ups and woody debris toward the top of Unit 3. Unit 2 consists of fine sand to pebble-size clasts in a sandy silt matrix with vertically-oriented and reverse-graded angular clasts. Unit 2 has remarkably similar matrix grain size modes throughout the unit and a minimum OSL age of 9.33 ± 2.3 kya at the unit boundary of Unit 2 (Figure 4.6A). This unit also contains sand and silt lenses with mud and organic rip ups (Figure 4.6B). A gradational boundary leads to Unit 1, which is massive diamicton with a distinctly lighter matrix than Unit 3. Unit 3 contains Fe, Ti, and Ca that show similar trends, albeit the sparse sampling interval does not allow for determination of correspondence with peaks in either (Figure 4.6B).

At Fort Casey Site 2, the first visible unit, Unit 5, contains interbedded clay and sand with reverse grading, or clear coarsening of material up-unit (Figure 4.7A). Unit 4, in which there are no physical samples, consists of diamicton with concentrated granule to pebble lenses and clay and silt lenses, as well as evidence of soft-sediment deformation. Unit 3 is a massive clay, followed by the thin silt of Unit 2 across an irregular, undulating, and most likely erosional contact. OSL dates at the top of Unit 2 and base of Unit 1 were found to be 40.8 ± 8.2 and 56.6 ± 15.5 kya. The overlying Unit 1 is a diamicton with very fine to cobble sized angular and rounded clasts. A normal gradation is present in the matrix of Unit 1 with crushed granite fragments. Unit 5 shows similar trends in Ca, Ti, and Fe, albeit are not well constrained due to sparse sampling intervals (Figure 4.7B). Unit 1 hosts peaks in Ti and Fe with a dip in Ca (Figure 4.7B).

4.3.3 Penn Cove

The lowest visible unit at this site, Unit 5, is comprised of a reverse-graded diamicton with a sand matrix and rounded granules and pebbles. The matrix grain size distributions through this unit show coarsening upward sand (Figure 4.8A). Following a sharp boundary with Unit 5, Unit 4 consists of silt and sand laminations with cross-bedded sands near the top. Unit 4 deposits were OSL dated to ages 56.6 ± 4.1 and 44.4 ± 2.8 kya. The grain size modes for Unit 4 are predominantly between 500-700 microns (Figure 4.8A). A non-parallel boundary at the top of Unit 4 leads to the clayey silt diamicton of Unit 3. This unstructured diamicton contains rounded fine to cobble size clasts with some sandy silt and silt lenses. A gradational boundary connects Units 3 and 2, which is a massive clay diamicton with rounded fine sand to cobble grains and articulated shells. Five shells were radiocarbon dated to an age of 12.9 ± 0.3 to 12.1 ± 0.3 kya cal. BP (Table 4.2). Unit 2 also contains sand lenses and wood fragments. Unit 2 has a sharp contact with Unit 1, which is a normally graded gravel with rounded and angular small to large pebbles with no predominant long-axis orientation. A mode of clay-sized grains is visible in Units 2 and 3 but is not visible in Unit 1 (Figure 4.8A). Fe, Ti, and Ca follow similar trends throughout this site (Figure 4.8B). Fe, Ti, Ca, and MS reach a collective peak in Unit 4 and then remain relatively high throughout Unit 1 despite minor fluctuations (Figure 4.8B).

4.3.4 West Beach

At West Beach Site 1, the lowest unit, Unit 5, consists of matrix-supported diamicton with randomly orientated clasts. There are two matrix grain size modes in this unit at 8 microns and 20 microns (Figure 4.9A). This unit has a sandy-silt lamination that interrupts the diamicton. The diamicton above the silty-sand lamination, however, contains highly irregular dips indicating soft-sediment deformation. Unit 5 gradationally leads into Unit 4 – a light clay layer deposited on a laterally irregular surface, marked by normal-grading, or fining upward (Figure 4.9A). Unit 3 consists of a thick gravel layer with less matrix and poorly sorted fine to cobble size clasts. A sharp, horizontally regular contact connects Unit 3 to the thick, well sorted sand of Unit 2. OSL ages in this unit were dated to 6.2 ± 0.6 and 4.1 ± 1.8 kya. Unit 2 has a gradational contact with Unit 1, which is a modern soil overlain by a basal shell hash dating between 1.56 ± 0.1 and 1.34 ± 0.1 kya cal. BP. While Fe, Ti, Ca, and MS follow similar trends through Units 5, 4, 2, and 1, Unit 3 shows peaks in Ti and Fe with corresponding dips in Ca and MS (Figure 4.9B). However, these correlations in chemical signature are not well constrained due to sparse sampling intervals.

At the base of West Beach Site 2, there are cross-bedded and coarse sand laminations. OSL dates from the sand in Unit 8 are dated to 31.3 ± 2.7 and 38.1 ± 9.7 kya. A gradational contact leads into Unit 7, consisting of silt and clay with radiocarbon dead woody debris. Unit 6 consists of sand with wavy bedding and silt laminations. No samples were collected from Units 5 and 4, consisting of a peat layer and a unit of sand and silt laminations, respectively. The Unit 3 diamicton matrix coarsens upwards and this unit has many grain size modes between 5 and 70 microns (Figure 4.10A). Unit 2 consists of fine to pebble sized sand-matrix diamicton and is not spatially continuous throughout the site. A gradational boundary leads into Unit 1, consisting of silt. Unit 1 has the only Ca peak in an otherwise Ca-deficient site (Figure 4.10B). The Ca peak in Unit 1 corresponds to dips in Fe and Ti levels (Figure 4.10B). Fe, Ti, and MS follow similar trends throughout this site as well (Figure 4.10B). However, these correlations in chemical signature are not well constrained due to sparse sampling intervals.

4.3.5 Rocky Point, Cliffside

The lowest visible unit at Cliffside, Unit 6, consists of fine to cobble size rounded clasts. This massive diamicton has no preferential orientation for clast long axis. The matrix changes from clay to sand and includes some evidence of soft-sediment deformation (Figure 4.11A). Unit 6 gradationally contacts Unit 5, which is a normally graded, fine sand to cobble size clast-diamicton. Unit 5 contains normally graded gravel lenses with horizontal long-axis orientation. Unit 5 gradually transitions into the granule and sand layer of Unit 4. Unit 4 includes sand and silt lenses within gravel-rich and wavy laminations. Unit 3 intrudes into Unit 4 and consists of a massive diamicton with rounded, outsized clasts. The matrix of Unit 3 has two grain size modes at 5 and 20 microns (Figure 4.11A). Two of the lower-unit samples for Cliffside Unit 3 were

taken from Rocky Point as this unit is continuous throughout both sites. Unit 3 gradually transitions into Unit 2, which is a laterally discontinuous light clay unit with silt layers. Unit 1 is comprised of mostly rounded, normally graded crushed granite with fine to large cobble size clasts. Units 6, 5, 3, 2, and 1 have similar trends in Fe, Ti, and MS values (Figure 4.11B). However, Unit 4 material shows a dip in Fe and Ti with a peak in MS (Figure 4.11B). Additionally, a peak in Ca can be seen in Unit 3.

4.4 Discussion and Interpretation

The extensive physical and sedimentological data, in addition to the geochronology samples collected at each site support reconstruction of depositional history across Whidbey Island. Starting with general facies interpretations, we present evidence for specific types of deposits and their significance in elucidating changes in depositional environments. Landscape evolution and ice behavior is then inferred from these facies classifications and used to describe regional landscape evolution before, during, and following LGM glaciation (Figure 4.13).

4.4.1 Facies interpretation

Unstructured diamicton with no preferential clast orientation, a range of matrix and clast sizes, and variable roundness are classified as **glacial tills**, or sediments deposited directly by glaciers in the subglacial environments (Boulton and Deynoux, 1981; Sengupta, 1994). Units classified as glacial till include Unit 2 from Double Bluff, Unit 3 at Fort Casey Site 1, Unit 1 from Fort Casey Site 2, Unit 3 from Penn Cove, Unit 5 from West Beach Site 1, and Unit 6 from Cliffside (Figures 4.5-4.9; 4.11; 4.13).

Glacial outwash, or variable diamicton with well-rounded and some angular clasts and parallel-to-bedding clast orientation that suggest the presence of glacial ice upstream of the outcrop site and proglacial meltwater yet in a subaerial or subaqueous environment rather than a subglacial environment (Boulton and Deynoux, 1981). The deposits usually also exhibit normal grading and peaks in terrigenous, lithogenic sourced material (i.e., Fe, Ti) and occasionally contain evidence of soft-sediment deformation (Boulton and Deynoux, 1981). Using this classification, Units 1 and 2 from Fort Casey Site 1, Units 4 and 5 from Fort Casey Site 2, Units 1 and 5 from Penn Cove, and Units 1 and 3 from Cliffside are all determined to be glacial outwash deposits (Figures 4.6-4.8; 4.11; 4.13).

Diamictons, resembling those interpreted as glacial till yet containing articulated and/or broken marine shells, occasional winnowing of fine-matrix material, sedimentary structures such as wavy laminations, and dips in Fe and Ti all point to **glacimarine sediments**, receiving both glacial and marine sediments and influence in a marine environment seaward of the ice margin. Both Unit 1 from Double Bluff and Unit 2 from Penn Cove meet these classifications (Figures 4.5; 4.8; 4.13). These glacimarine sediments indicate ice retreat within a marine environment; while conversely, glacial till lacking marine shells and overlain by subaerial deposits (i.e., those

with cross-bedded sands, parallel-to-bed oriented gravels, wavy laminations) indicate **ice retreat in a subaerial environment**. Unit 3 from West Beach Site 1 and Unit 5 from Cliffside both meet these classifications (Figures 4.9; 4.11; 4.13).

Facies with grain sizes coarsening-upward and correspond with increasing values of Fe, Ti, and MS are associated with **landscape emergence** (Sengupta, 1994; Komar, 1998). The coarsening of material between Units 3 and 2 at Fort Casey Site 2, transition from Unit 5 laminated silt to Unit 4 cross-bedded sand at Penn Cove, and coarsening of grain size with peaks in Ti, Fe, and MS across Units 7 and 6 at West Beach Site 2 all indicate land emergence events (Figures 4.7; 4.8; 4.10; 4.13).

Facies with grain-sizes that fine-upward, correspond with dips in Fe, Ti, and MS, and have a presence of marine shells are associated with **landscape submergence** (Sengupta, 1994; Komar, 1998). The transition from Unit 4 sand deposits to Unit 3 silts at Double Bluff, introduction of shells to the fining material between Units 2 and 1 at West Beach Site 1, and fining of grain size, corresponding with a peak in Ca across the Unit 2 and 1 boundary at West Beach Site 2 are all interpreted as land submergence events (Figures 4.5; 4.9; 4.10; 4.13).

4.4.2 Pre-LGM landscape evolution

Prior to LGM glacial advance across Whidbey Island, several submergence and emergence facies record dramatic landscape changes. An event of landscape emergence is recorded across both Penn Cove and Fort Casey Site 2. Penn Cove OSL ages identify this landscape emergence to occur between 56.6 ± 4.1 and 44.4 ± 2.8 kya (Figure 4.14). Similar Fort Casey Site 2 OSL ages constrain this event to 56.6 ± 15.5 and 40.8 ± 8.2 kya (Figure 4.14), placing the emergence within the MIS 4 glacial and MIS 3 interglacial transition.

A sequence of transgressive (emergence) and regressive (submergence) facies are observed in the pre-LGM deposits at West Beach Site 2. OSL dates from one of the regressive facies places a submergence event between 38.1 ± 9.7 and 31.3 ± 2.65 kya while OSL dates from overlying transgressive facies places subsequent emergence between 30.7 ± 2.5 and 29.2 ± 4.6 kya. Both of these events occurred within the MIS 3 interglacial. This rapid transition between landscape submergence and emergence not only identifies high sedimentation rates at this site during MIS 3 but also indicates that the southern CIS experienced rapid growth and decay during this time period.

4.4.3 LGM glacial advance

Erosional contacts between glacial till and underlying facies mark LGM advance of ice into the region at multiple sites across Whidbey Island including Double Bluff, Fort Casey Site 2, and Penn Cove (Figure A4.2A). OSL dates from below the erosional contact place maximum age of ice extent at 56.6 ± 4.1 and 44.4 ± 2.8 kya, however sediments from MIS 4 and 3 are

missing from this record. An OSL age from the bottommost glacial till from Fort Casey Site 1 places deposition at 9.33 ± 2.3 kya, constraining these glacial facies to LGM ice advance.

4.4.4 Deglaciation

The glacial marine sediments in the uppermost 50 cm of Double Bluff Unit 1 records retreat of ice within a marine environment (Figure A4.2B). At Penn Cove, the presence of articulated shells and winnowing of smaller grain sizes from glacial tills suggests marine water intrusions into the subglacial environment during deglaciation. Five articulated shells found at Penn Cove were radiocarbon dated to a range of dates between 12.9 ± 0.3 and 12.1 ± 0.3 kya cal. BP (Table 4.2). These dates place glacial ice into this region for ~3,000 years longer than previously thought (e.g., Easterbrook, 1992; Dethier et al., 1995; Swanson & Caffee, 2001).

Based on the range in shell radiocarbon dates, glacial ice also appears to be stable at Penn Cove for at least 1,000 years (Figure 4.8A) with high rates of deposition, accumulating two and half meters of material during this period. The length of ice stability is an indication that ice retreat was step-wise, rather than catastrophic (Easterbrook, 1992). Step-wise retreat of the margin is also supported by the presence of grounding-zone wedges (GZWs) and high rates of sedimentation in the region (~2.5 mm/year) at this site, indicating the ice margin is nearby to this site (Figure 4.12; Demet et al., 2019; Simkins et al., 2017). Grounding zone wedges represent periodic stand-stills of a grounding zone, allowing for accumulation of sediment in a triangular shape (e.g., Simkins et al., 2018).

Deglacial facies seen at the more northern West Beach Site 1 and Cliffside indicate ice retreat within a subaerial environment (Figure 4.13). The change in ice retreat style seen from the more southern Double Bluff and Penn Cove sites to the northern West Beach and Cliffside sites may be due to the substantial stand-still of ice at Penn Cove. Rocky Point is also a location with a bedrock high and mapped GZWs, suggesting this site could have periodically stabilized ice during land rebound before final deglaciation of the region (Demet et al., 2019; Simkins et al., 2018).

4.4.5 Post-LGM landscape evolution

Following deglaciation of the region, several sites including Penn Cove and Cliffside record outwash deposits from proglacial fluvial sources. An OSL age within the submergence facies of Unit 2 at West Beach Site 1 marks the transition from a post glacial fluvial environment to a submerged marine environment between 6.2 ± 0.6 and 4.1 ± 1.8 kya. Radiocarbon dated shell hash found in the uppermost unit at this same West Beach Site 1 suggests a highly energetic marine system was present in this location as early as 1.56 ± 0.1 kya cal. BP, at least 5,000 years following loss of ice in the Puget Lowland. After initial rigid-lithospheric rebound from ice-loading, it is possible vertical land movement slowed enough to allow eustatic sea level to resubmerge the region around 1,000 years ago (Figure 4.9A). Before the addition of this work,

rates of GIA in the Puget Lowland were cited to have been as high as 10 cm a^{-1} during early deglaciation, which is thought to be at least an order of magnitude larger than the rate of vertical land motion from tectonics (Booth and Hallet, 1993; Dethier et al., 1995; Kovanen and Slaymaker, 2004; Eyles et al., 2018; Demet et al., 2019).

Overall, findings from this work support better understanding of the extinct CIS while also elucidating the role GIA and subglacial topography may play in determining ice-margin retreat styles for systems with similar subglacial topography and rheologic settings such as margins of Greenland and the Antarctic Peninsula (Eyles et al., 2018; Whitehouse et al., 2019; Nield et al., 2014).

4.5 Conclusions

This decimeter-scale physical and chemical sedimentological assessment, paired with geochronological assessment of seven sites across the deglaciated Puget Lowland, provides information on specific timing and rate of landscape emergence and submergence as well as final ice advance and retreat of the southernmost CIS. Recording landscape emergence and submergence through OSL dating indicates the Puget Lowland was a highly dynamic region where a sequence of landscape emergence and submergence was able to occur within $\sim 1,000$ years in MIS 3, despite the concurrent period of rapid and substantial global mean sea level rise (Yokoyama & Purcell, 2021). Additionally, findings place glacial ice in the Puget Lowland for 3,000 years longer during the LGM than previously thought, with final retreat occurring across the middle of Whidbey Island at approximately $12.1 \pm 0.3 \text{ kya cal. BP}$. Radiocarbon dates are used to show substantial stand-still and sedimentation near the ice grounding line during final retreat. While more southern sites record ice retreat within submarine environments, the northernmost stratigraphic site, which corresponds with a topographic high and previously mapped grounding-zone wedge (Demet et al., 2019), appears to record ice retreat into a subaerial environment. This work provides empirical evidence that coastal Washington experienced rapid vertical landscape evolution, which had the potential to contribute to marine-terminating ice stability for at least a millennia. The similarities between the rheology in this location and the rheology of the Antarctic Peninsula, as well as the topographic similarities between the Puget Lowland and modern margins of the Greenland Ice Sheet make these findings highly relevant to increasing process-based understanding of solid Earth influence on ice dynamics in contemporary marine-terminating glacial systems.

Table 4.1. Site and sample collection information

Site	Sediment samples	Radiocarbon samples	OSL samples
Double Bluff (a)	53	2	0
Fort Casey (b)	20	0	2
Penn Cove (c)	126	8	2
West Beach (d)	54	4	6
Cliffside (e)	29	0	0
Total	282	14	12

Table 4.2. Radiocarbon sample descriptions and data. Gray rows indicate known-age shells dated to develop MRC.

Name	Type	Age ± error (RCY)	MRC	Δ13C	Age ± error (cal year BP)	actual age (cal year BP)	NOSAMS Receipt #	NOSAMS Accession #
WB S1 RCD1 s.h. base U6	Mollusc	1290 ± 20	278 ± 35	-0.84	1494 ± 137	n/a	176236	OS-164669
WB S1 RCD1 s.h. base U6 clam	Mollusc	1210 ± 25	278 ± 35	-1.4	1563 ± 130	n/a	176237	OS-164670
WB S1 U6 RCD2	Mollusc	1450 ± 15	236 ± 30	0.12	1336 ± 112	n/a	176238	OS-164671
PC S3 U3 RCD3	Mollusc	13200 ± 75	278 ± 35	0.44	12646 ± 371	n/a	176239	OS-164691
PC S3 U4 RCD5	Mollusc	13000 ± 75	271 ± 35	-0.31	12305 ± 327	n/a	176240	OS-164692
PC S3 U4 RCD1 a.s.	Mollusc	13250 ± 75	264 ± 36	0.13	12749 ± 366	n/a	176241	OS-164693
PC S4 U6 RCD1	Mollusc	1400 ± 20	264 ± 36		1390 ± 114	n/a	171379	OS-160221
PC S3-4 RCD2	Mollusc	12900 ± 55	264 ± 36		12147 ± 293	n/a	171380	OS-160222
PC S3 RCD4	Mollusc	13200 ± 55	264 ± 36		12674 ± 334	n/a	171381	OS-160223
PC S3 U4 RCD3	Mollusc	13300 ± 75	216 ± 30	0.33	12923 ± 343	n/a	176242	OS-164694
WB S2 U1 RCD1	Plant/Wood	>48000		-23.48		n/a	176243	OS-164850
PC S4 U6 RCD2	Mollusc	1720 ± 15	236 ± 30	-0.06	1087 ± 145	n/a	176244	OS-164695
DB S3 RCD1 U4	Plant/Wood	>46700				n/a	171378	OS-160371
DB S5 RCD1 U7	Plant/Wood	>48000		-28.62		n/a	176245	OS-164851
Mo. r. 6298-1	Mollusc	840 ± 15	236 ± 30	0.15	1872 ± 145	91	176246	OS-164743
Mu. n. 3320-1	Mollusc	860 ± 25	253 ± 51	1.36	1860 ± 148	110	176247	OS-164744
Mu. n. 3320-2	Mollusc	925 ± 20	318 ± 40	1.42	1866 ± 145	110	176248	OS-164745
Ca. v. 13329-1	Mollusc	875 ± 20	270 ± 40	0.49	1867 ± 145	104	176249	OS-164746
Ca. v. 13329-2	Mollusc	890 ± 15	285 ± 30	1.74	1871 ± 144	104	176250	OS-164747
Ma. c. 3348-1	Mollusc	895 ± 15	288 ± 30	0.85	1870 ± 143	110	176251	OS-164748
Ma. c. 3348-2	Mollusc	890 ± 20	283 ± 40	0.05	1866 ± 145	110	176252	OS-164749
My. a. 3427-1	Mollusc	905 ± 15	298 ± 30	0.83	1870 ± 143	110	176253	OS-164750
My. a. 3427-2	Mollusc	850 ± 20	243 ± 40	0.74	1866 ± 145	110	176254	OS-164751
Ma. n. 3470-1	Mollusc	825 ± 15	221 ± 30	0.99	1872 ± 175	91	176255	OS-164760
Ma. n. 3470-2	Mollusc	815 ± 15	211 ± 30	0.39	1872 ± 175	91	176256	OS-164761

Table 4.3. OSL measurement sequence

1. Radiation dose D_i
 2. Preheat at 180°C^* for 10s
 3. IRSL at 125°C for 150s to remove feldspar signal
 4. OSL at 125°C for 100s, measure OSL signal L_i
 5. Fixed test radiation dose D_t^{**}
 6. Cutheat at 160°C to remove unstable signals
 7. IRSL at 125°C for 150s to remove feldspar signal
 8. OSL at 125°C for 100s, measure OSL signal T_i
 9. Repeat steps 2-8 for cycle 0 and steps 1-8 for cycles 1-7
- Cycle 0: Natural signal, $D_0 = 0$ Gy with no administered dose
Cycle 1-4: Regenerative doses, $D_1, D_2 < D_0 < D_3 < D_4$
Cycle 5: Dose recovery test, $D_2 < D_5 < D_3^{***}$
Cycle 6: Recycle test, $D_6 = D_1^{***}$
Cycle 7: Recuperation test, $D_7 = 0$

* preheat temperature determined by plateau test

** $D_t = 15\text{-}20\%$ D_0

*** administered to check the precision with which a known dose can be recovered

Table 4.4. Dose measurements, dose rate, and OSL age data. Final sample ages are bolded.

Sample	grain sizes measured	Dose (Gy)	Dose err (Gy)	fading rate (%/decade)	g err	Gamma dose rate (Gy/ka)	Gamma dose rate error	Beta dose rate (Gy/ka)	Beta dose rate error	Internal Beta dose rate (Gy/ka)	Internal Beta dose error (Gy/ka)	total dose rate (Gy/ka)	total dose rate error (Gy/ka)	Age unfaded (ka)	err	Age after fading (ka)	err
FC51-OSL1	90-125	12.13	2.82	7.1	6.1	0.33	0.03	0.61	0.03	0.18	0.07	1.30	0.09	9.33	2.25		
FC51-OSL2																	
FC52-OSL1	63-90	92.96	7.27	3.6	3.8	0.67	0.07	1.27	0.06	0.14	0.06	2.26	0.11	41.18	3.76	56.6	15.5
FC52-OSL2	63-90	69.16	4.6	2.7	2.5	0.60	0.06	1.21	0.06	0.14	0.06	2.13	0.10	32.48	2.65	40.8	8.2
WB51-OSL1	150-250	7.5	0.68	2.6	5.5	0.55	0.06	1.10	0.06	0.36	0.21	2.20	0.22	3.40	0.46	4.10	1.78
WB51-OSL2	90-150	11.86	0.68	0		0.56	0.07	1.14	0.06	0.00	0.11	1.90	0.14	6.24	0.59		
WB52-OSL1	90-212	64.58	4.66	3.74	2.5	0.67	0.05	1.39	0.06	0.25	0.23	2.37	0.24	27.22	3.39	38.05	9.65
WB52-OSL2	90-150	70.97	4.1	0		0.67	0.05	1.33	0.07	0.22	0.11	2.27	0.14	31.27	2.65		
WB53-OSL1	150-212	68.43	4.96	0		0.62	0.05	1.20	0.05	0.34	0.04	2.23	0.08	30.71	2.50		
WB53-OSL2	150-212	55.9	4.77	2.99	1.7	0.73	0.06	1.42	0.06	0.25	0.07	2.47	0.11	22.64	2.19	29.18	4.63
PC52-OSL1	125-150	75.47	5.77	4.54	0.28	0.49	0.04	0.97	0.04	0.45	0.07	2.05	0.10	36.80	3.29	56.60	4.14
PC52-OSL2	125-150	93.2	4.11	0		0.50	0.04	1.02	0.05	0.45	0.07	2.10	0.10	44.39	2.82		

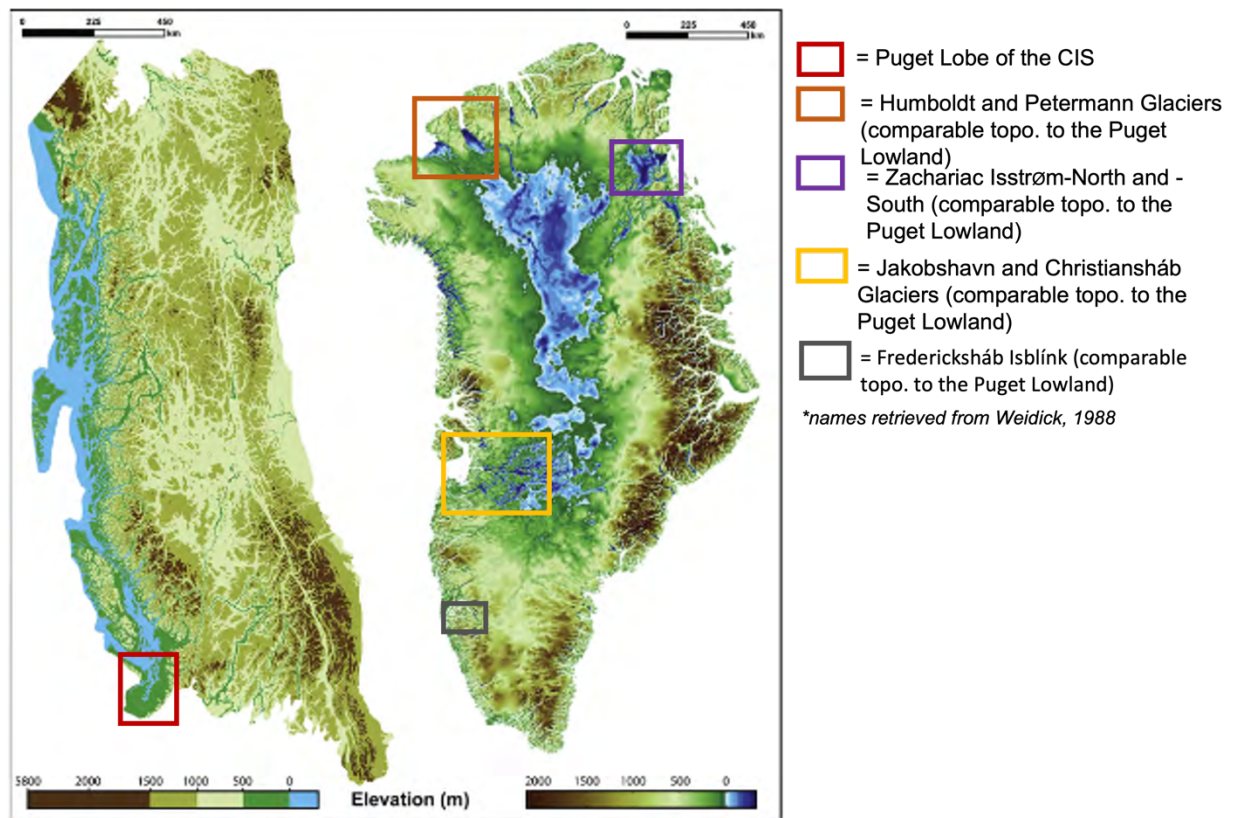


Figure 4.1. Adapted from Fig. 26 in Eyles et al., 2018: “Size and basal topography of the present-day Greenland Ice Sheet (GrIS; Rippin, 2013; Morlighem et al., 2014) compared to the Late Wisconsin Cordilleran Ice Sheet (CIS). Both ice sheets of a comparatively low relief central core zone are flanked by regions of high mountainous relief. Both ice sheets possess a presence of thick subglacial sediments.” Outlined boxes indicate outlet glaciers of similar topographic setting to highlight the applicability of applying glacial processes in the Puget Lowland to modern systems.



Figure 4.2. Outcrop sites on Whidbey Island (white outline) in the northern Puget Lowland, Washington state.



Figure 4.3. The outcrop site at (a) West Beach shows evidence for final ice retreat below sea level due to the presence of marine shells stratigraphically above the last diamicton unit. Outcrops at (b) Fort Casey indicated ice retreat in a subaerial environment due to the lack of glaciomarine materials, indicating land emergence before ice retreat. The bedrock exposure at (c) Rocky Point may have had some topographic influence on ice flow. (d) Penn Cove outcrop cross-bedded sand below a massive diamicton sampled for OSL to constrain LGM ice re-advance into the region. (e) Woody debris in laminated silty-clay at West Beach, collected for radiocarbon dating.

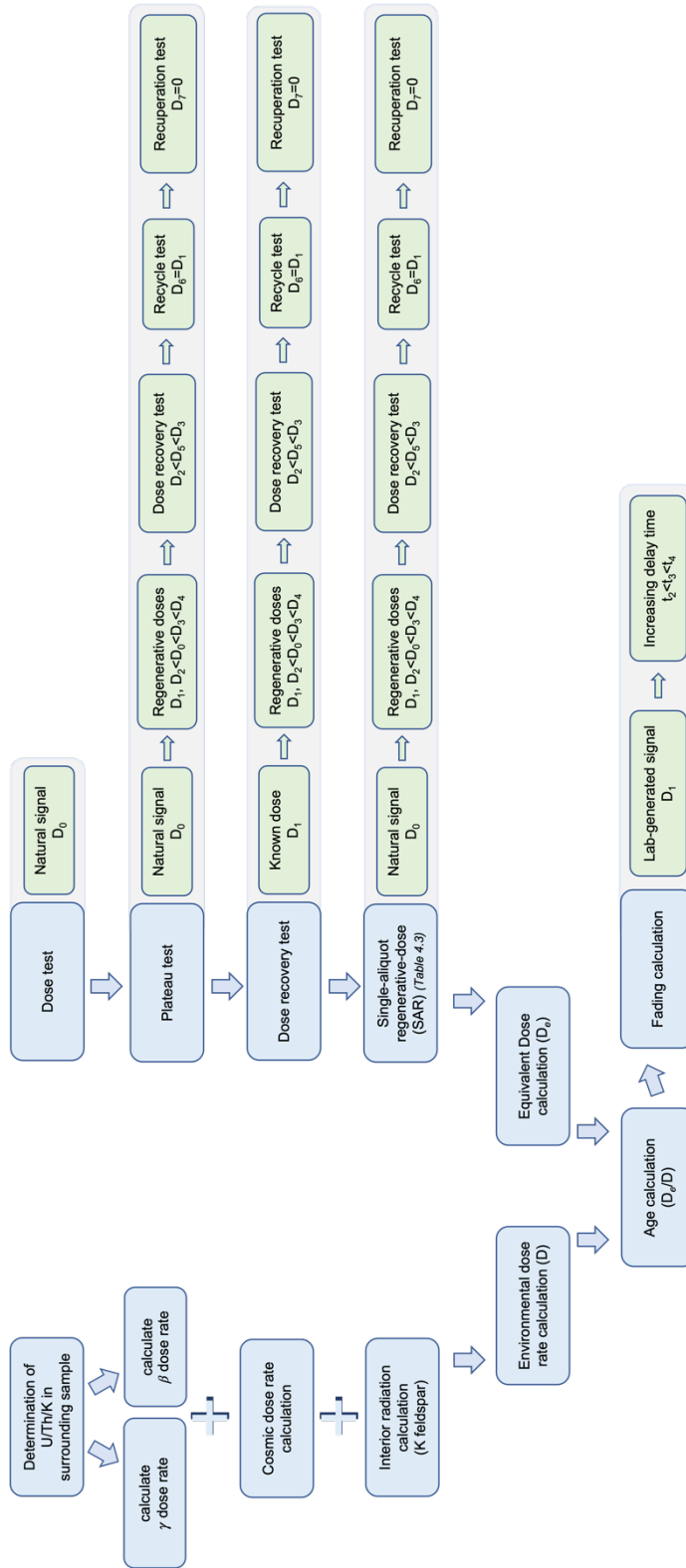


Figure 4.4. OSL calculation workflow.

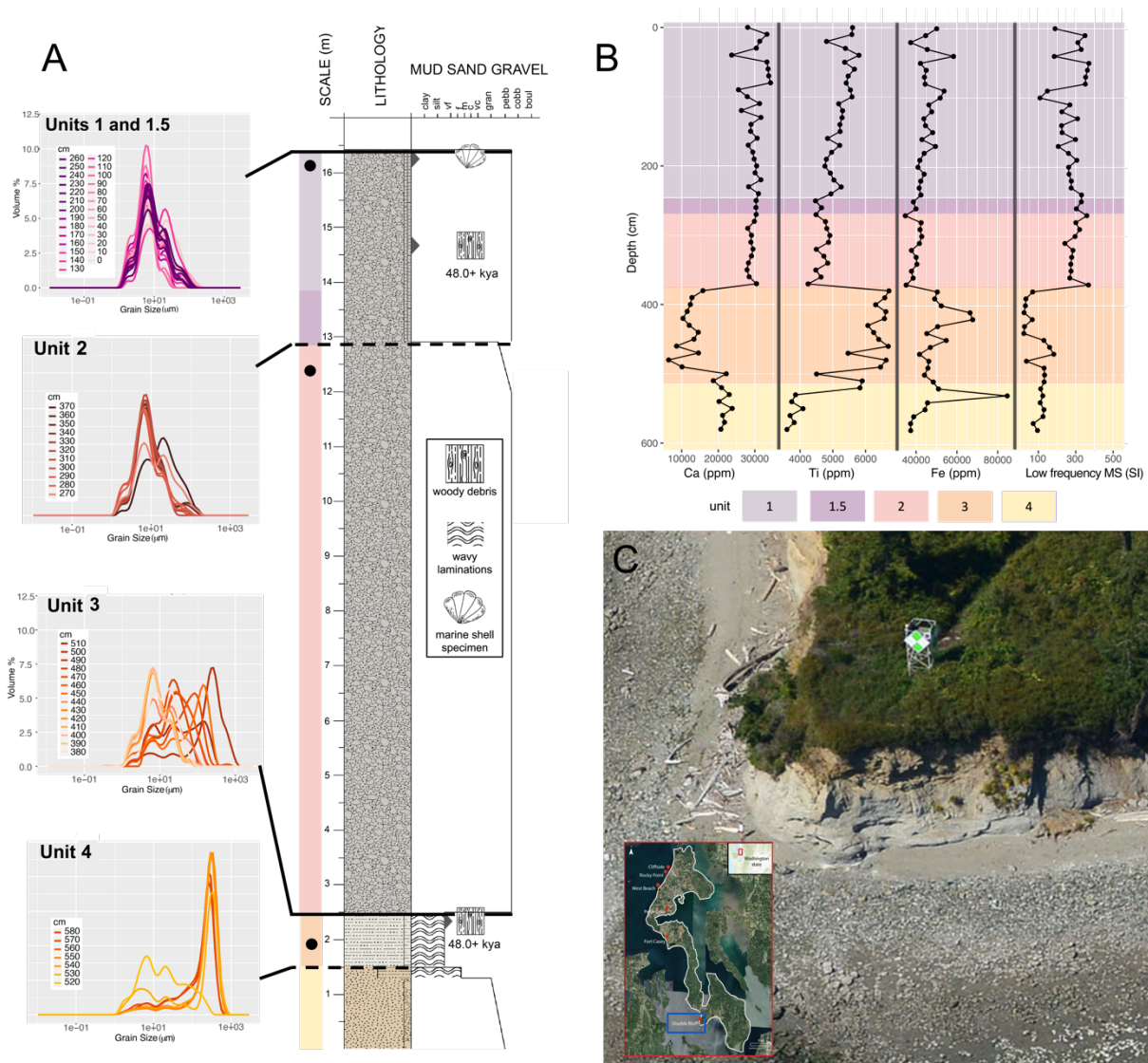


Figure 4.5. Double Bluff A) stratigraphic column with radiocarbon and OSL data and grain size data. Black dots indicate changes to site collection of samples. B) Trace element and magnetic susceptibility data for this site. C) Example coastal bluffs at Double Bluff taken from the Washington state Shoreline Viewer with inset regional map.

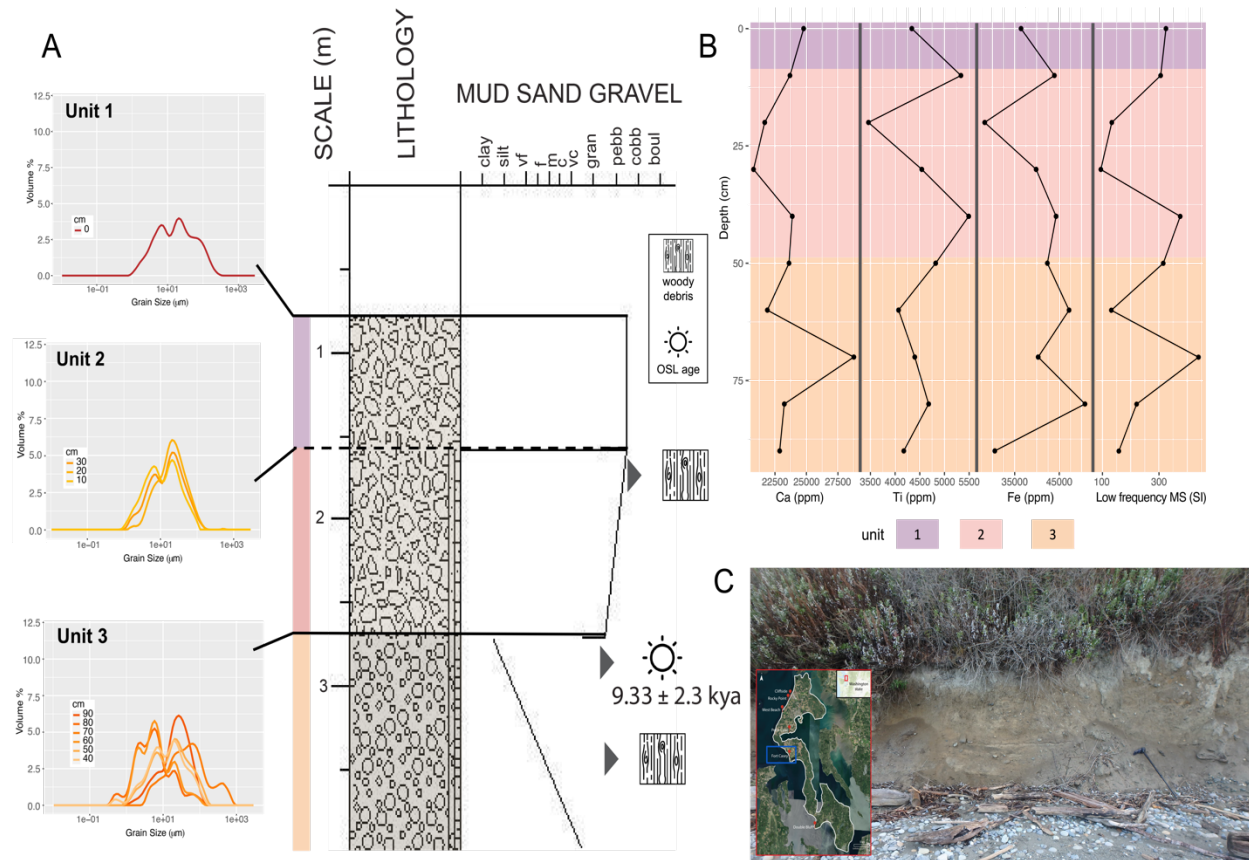


Figure 4.6. Fort Casey Site 1 A) stratigraphic column with radiocarbon and OSL data and grain size data. B) Trace element and magnetic susceptibility data for this site. C) Example coastal bluffs at Fort Casey Site 1 taken by M. McKenzie with inset regional map.

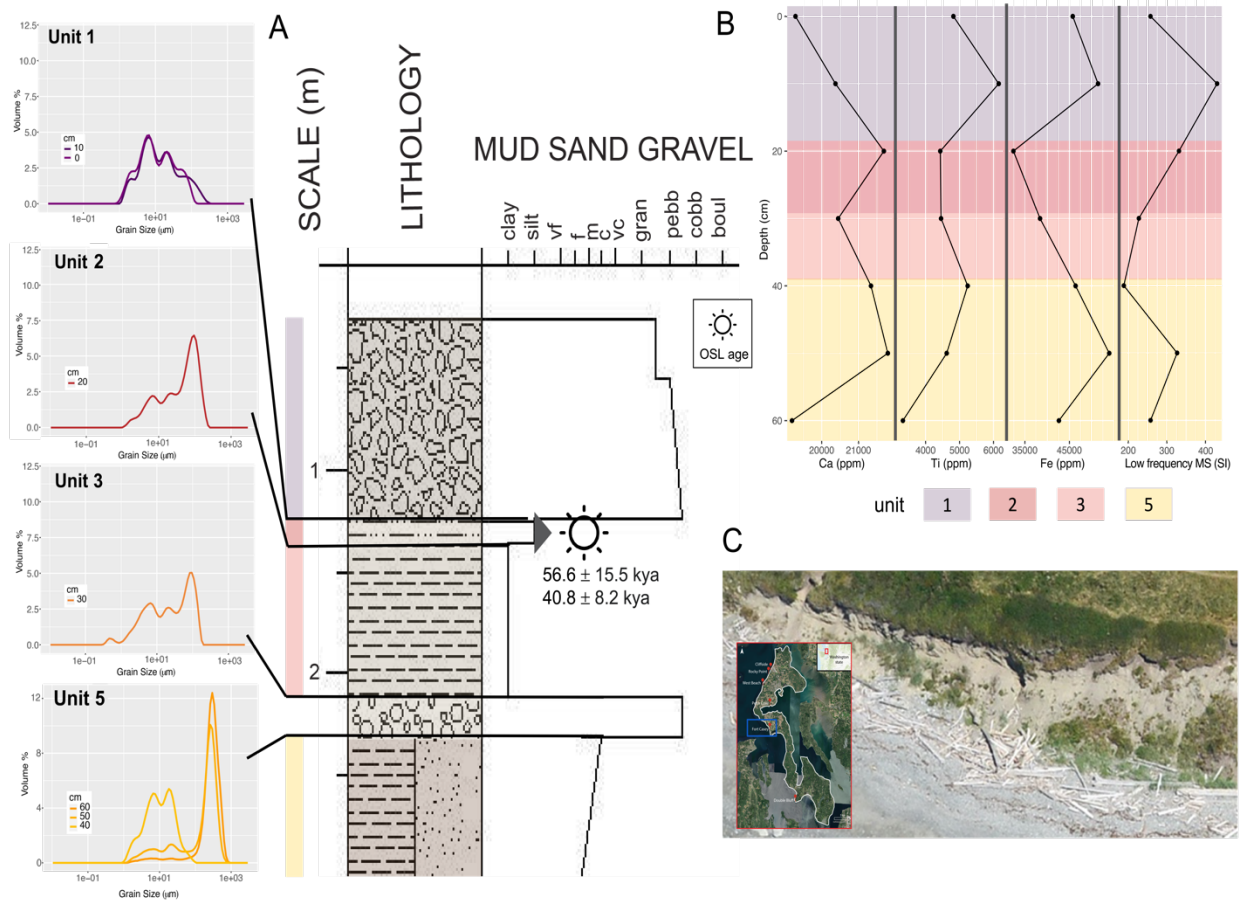


Figure 4.7. Fort Casey Site 2 A) stratigraphic column with radiocarbon and OSL data and grain size data. B) Trace element and magnetic susceptibility data for this site. C) Example coastal bluffs at Fort Casey Site 2 taken from the Washington state Shoreline Viewer with inset regional map.

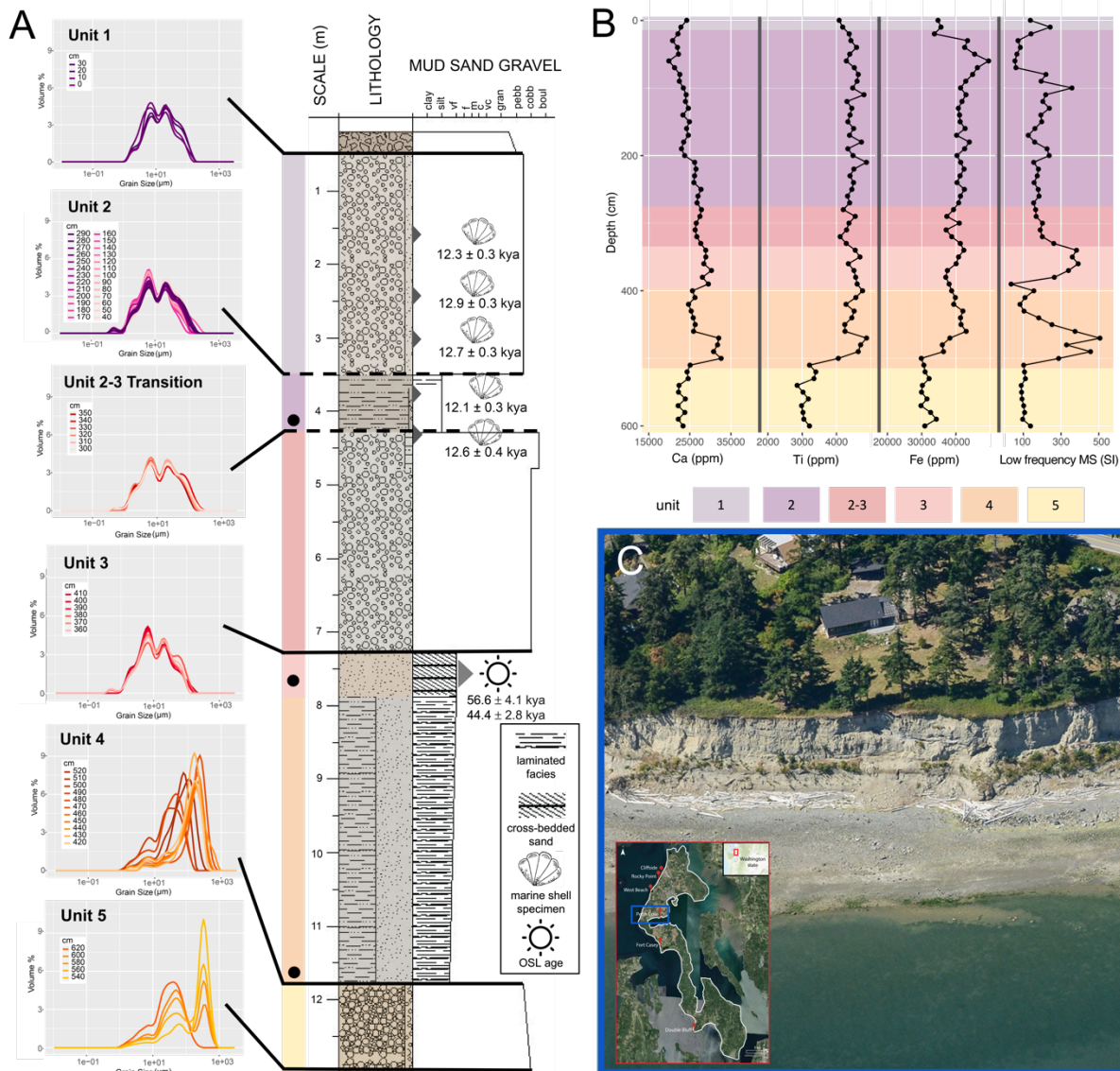


Figure 4.8. Penn Cove A) stratigraphic column with radiocarbon and OSL data and grain size data. Black dots indicate changes to site collection of samples. B) Trace element and magnetic susceptibility data for this site. C) Example coastal bluffs at Penn Cove taken from the Washington state Shoreline Viewer with inset regional map.

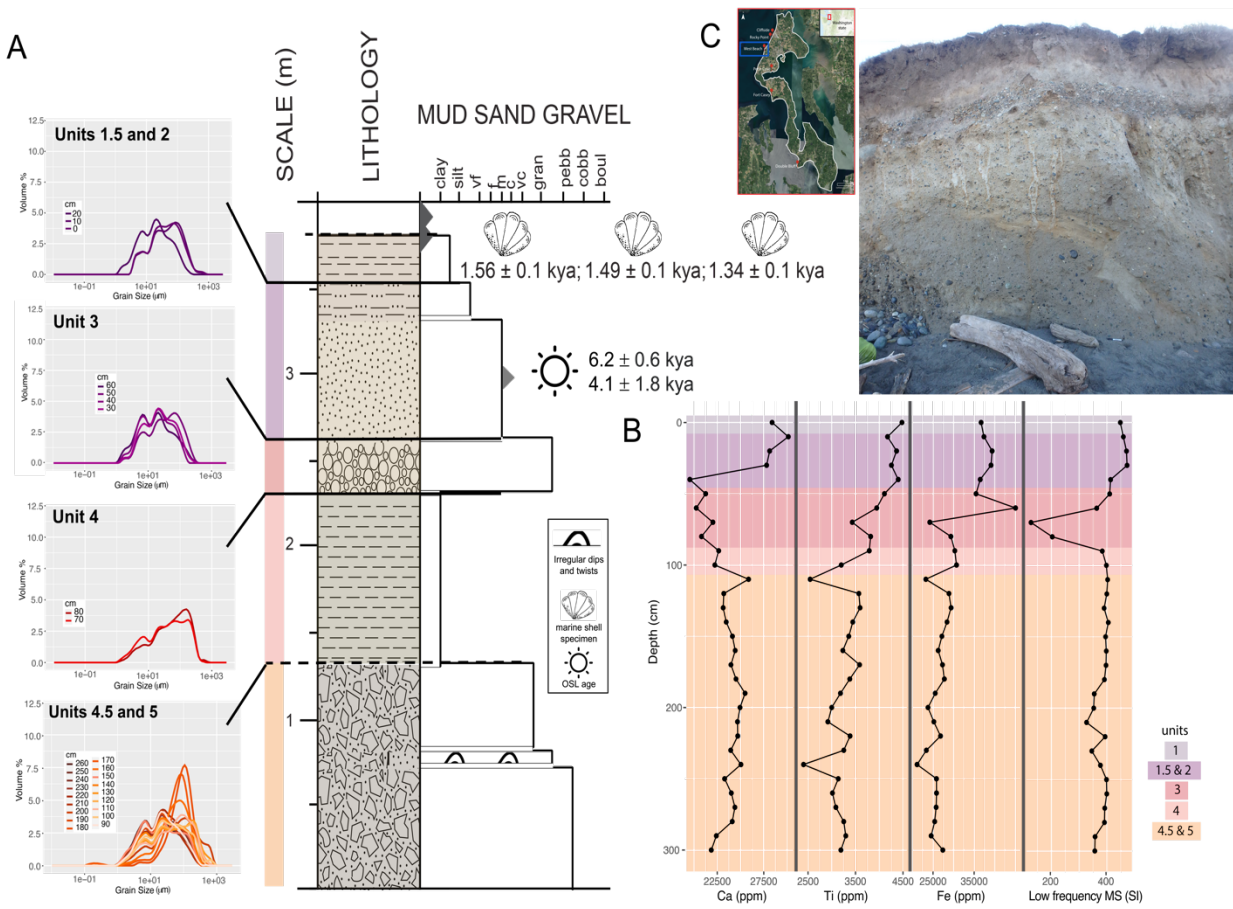


Figure 4.9. West Beach Site 1 A) stratigraphic column with radiocarbon and OSL data and grain size data. B) Trace element and magnetic susceptibility data for this site. C) Example coastal bluffs at West Beach Site 1 taken by M. McKenzie with inset regional map.

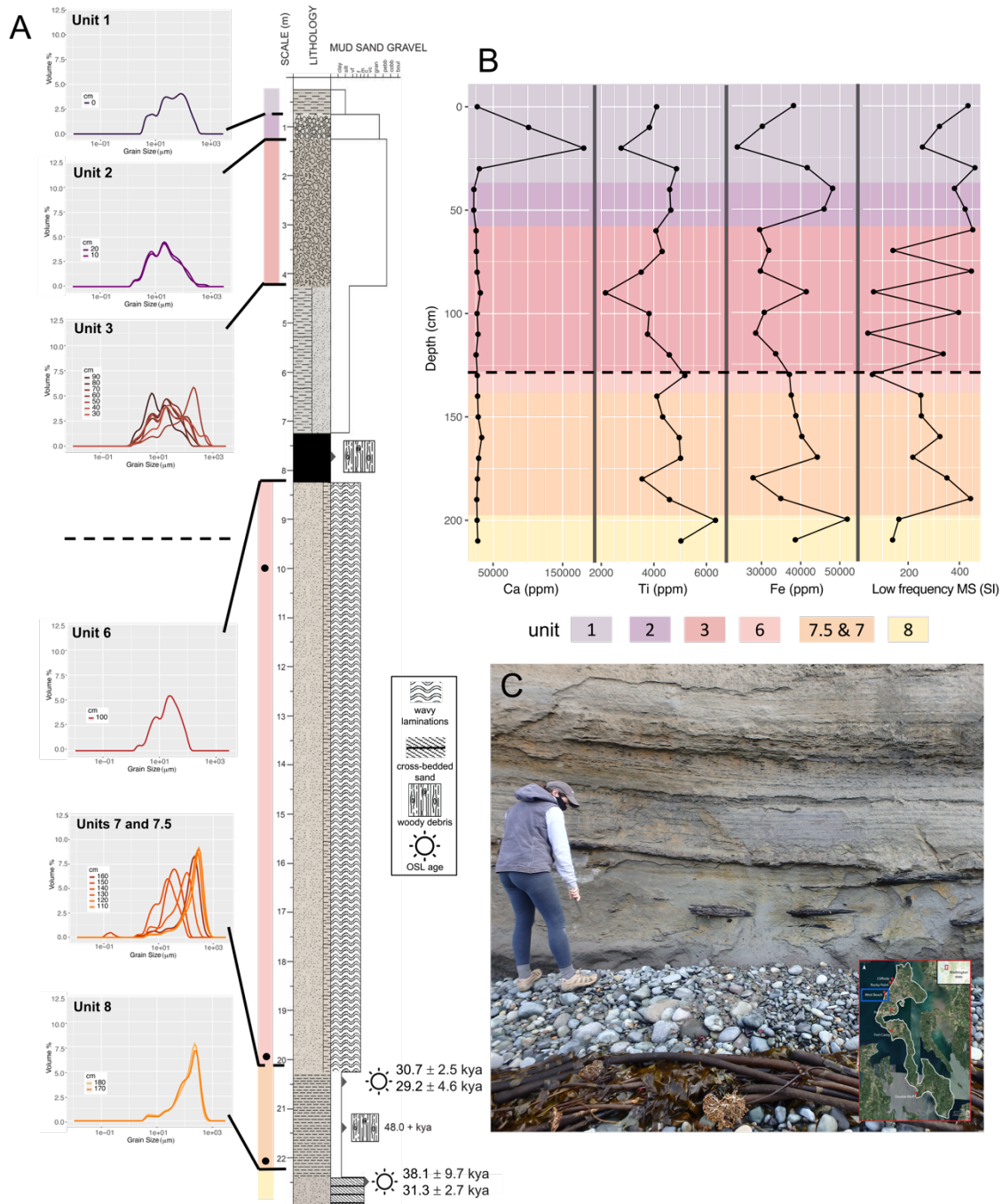


Figure 4.10. West Beach Site 2 A) stratigraphic column with radiocarbon and OSL data and grain size data. Black dots indicate changes to site collection of samples. B) Trace element and magnetic susceptibility data for this site. C) Example coastal bluffs at West Beach Site 2 taken by M. McKenzie with inset regional map.

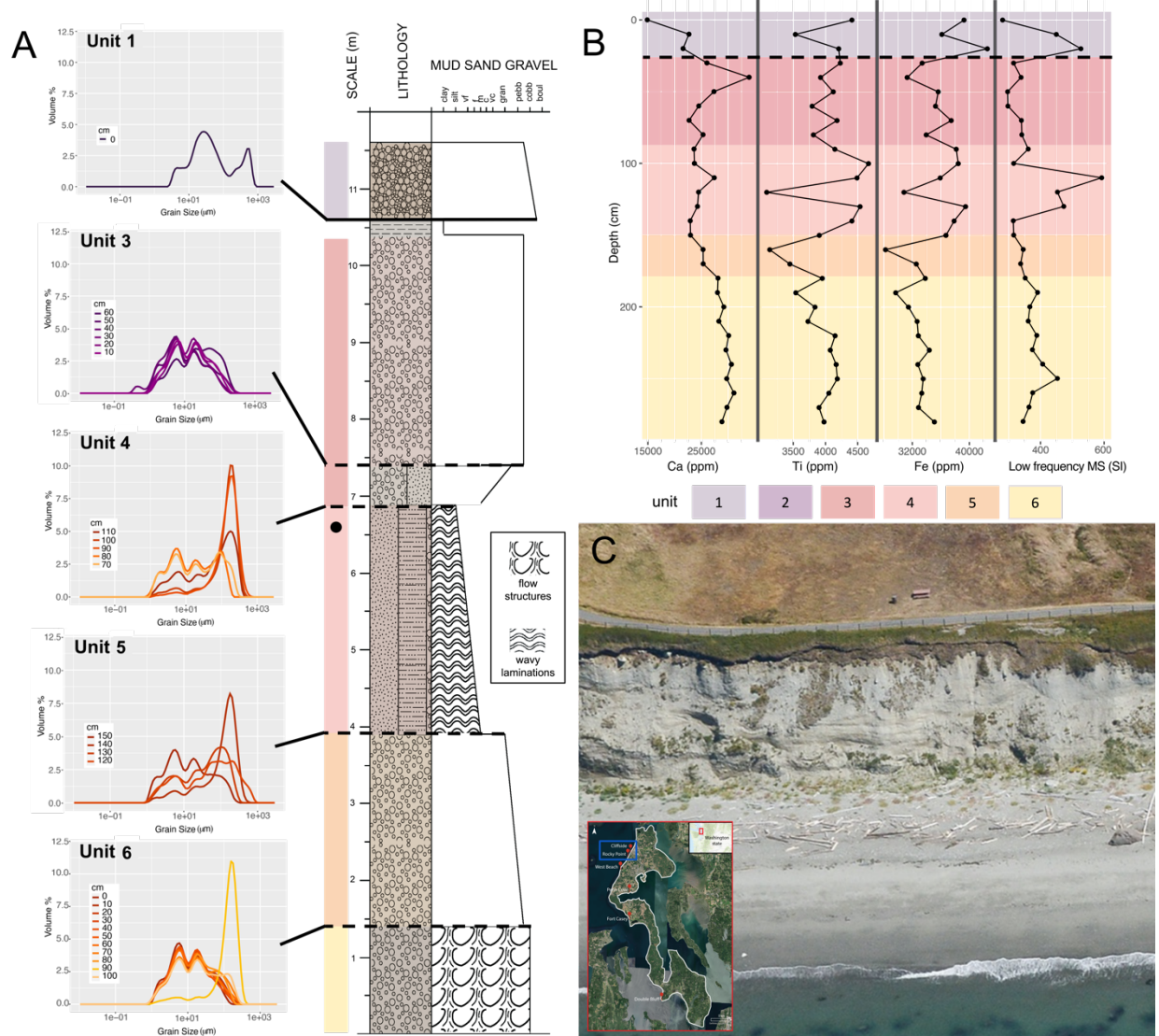


Figure 4.11. Cliffside A) stratigraphic column with radiocarbon and OSL data and grain size data. Black dots indicate changes to site collection of samples. B) Trace element and magnetic susceptibility data for this site. C) Example coastal bluffs at Cliffside taken from the Washington state Shoreline Viewer with inset regional map.

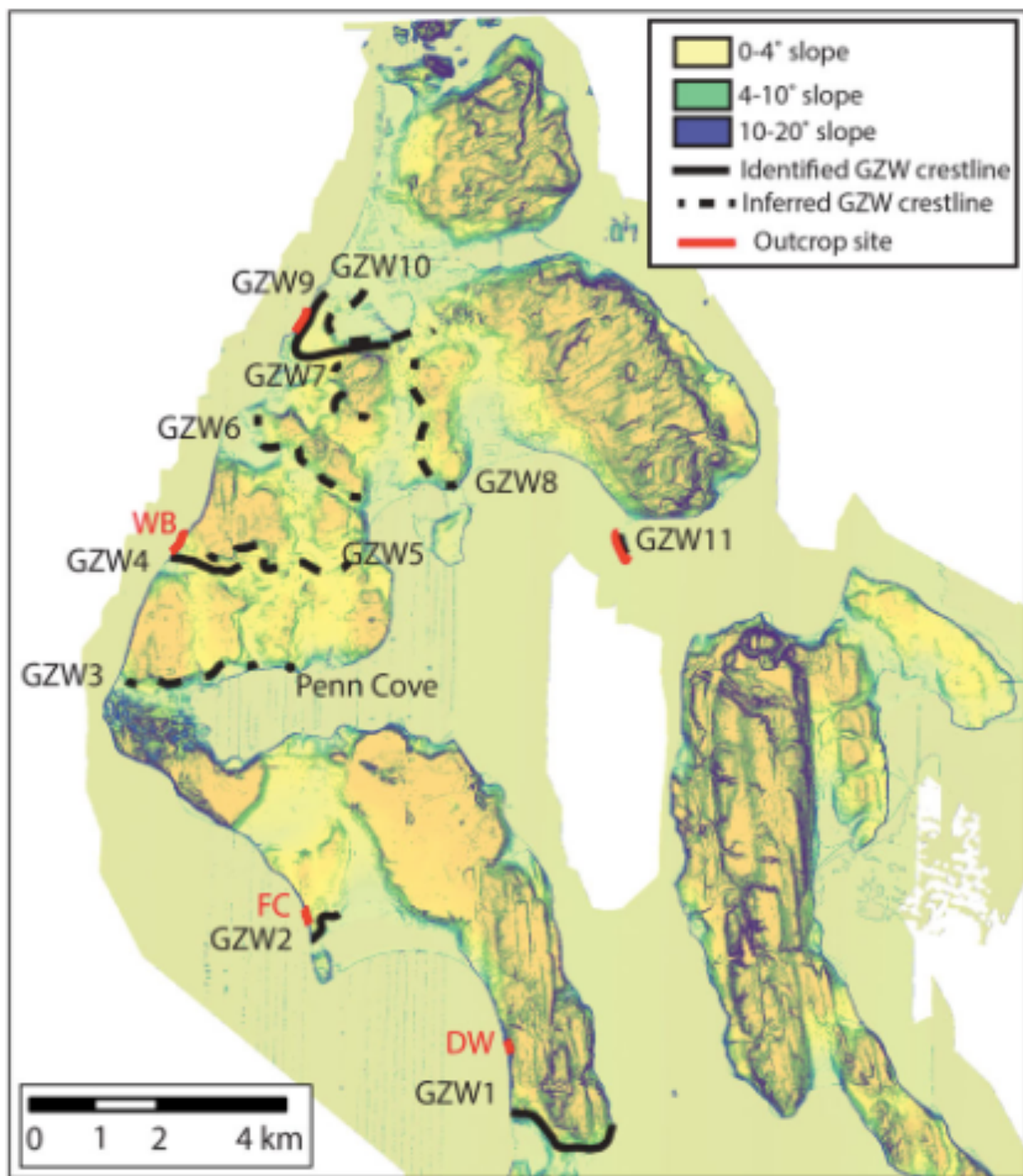
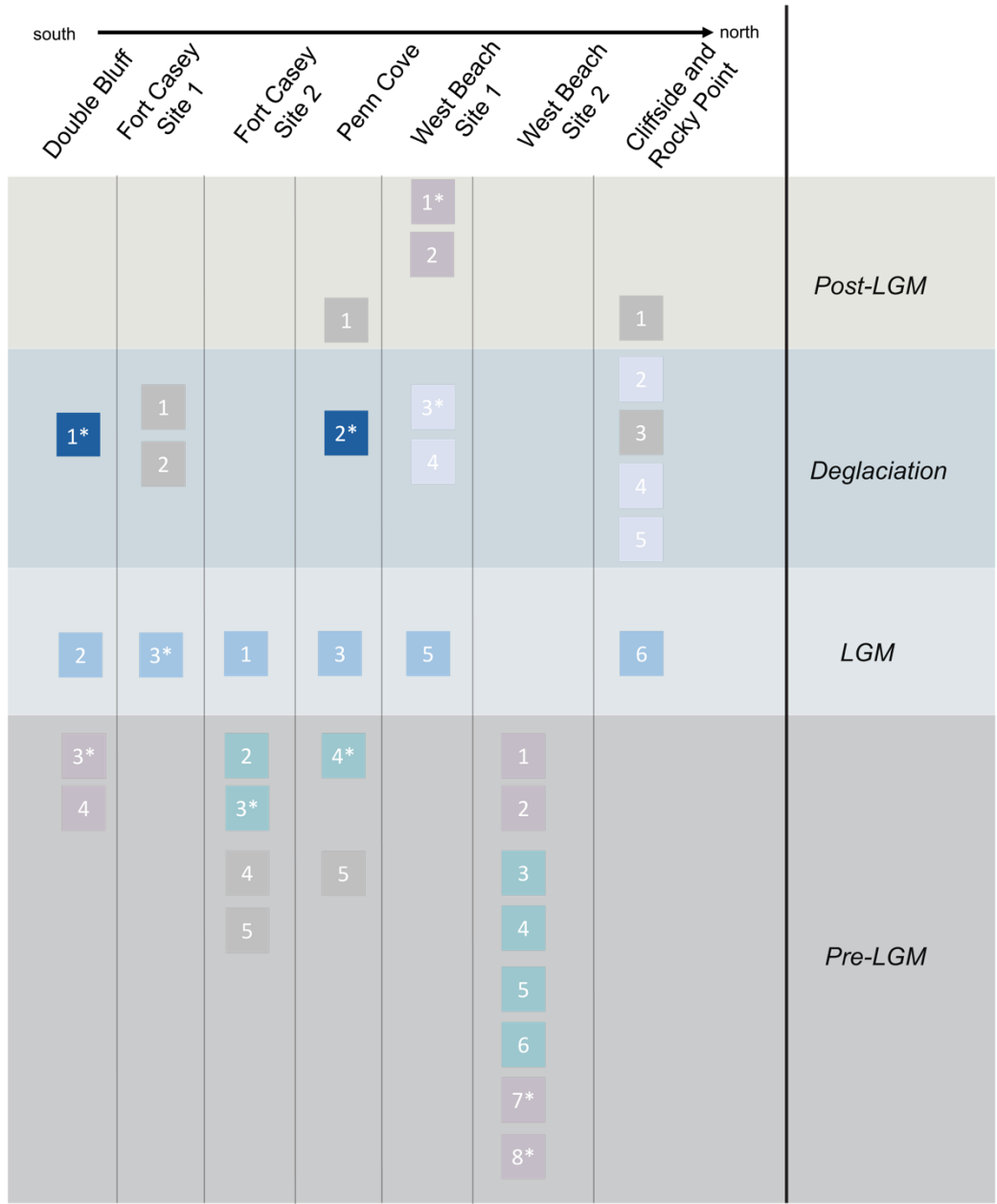


Figure 4.12. Figure 4 from Demet et al., 2019: “Map of surface slopes of Whidbey Island. Crestline orientations record episodic change in ice flow direction. Inferred GZW crestlines lack outcrop exposure. Outcrop locations are highlighted in red, with West Beach (WB) Fort Casey (FC) and Driftwood (DW) sections labeled.” In addition to the West Beach, Fort Casey, and Driftwood (in this work. Double Bluff) sites being stratigraphically assessed, the Penn Cove stratigraphy was also assessed in this project.



Site	Unit	Type	Date (kya)
Double Bluff	1,3		48.0+ cal. BP
Fort Casey Site 1	3		9.33 ± 2.3
Fort Casey Site 2	3		56.6 ± 15.5 ; 40.8 ± 8.2
Penn Cove	2		12.9 ± 0.3 cal. BP; 12.1 ± 0.3 cal. BP
	4		56.6 ± 4.1 ; 44.4 ± 2.8
West Beach Site 1	1		1.56 ± 0.1 cal. BP
	3		6.2 ± 0.6 ; 4.1 ± 1.8
West Beach Site 2	7		30.7 ± 2.5 ; 29.2 ± 4.6
	8		38.1 ± 9.7 ; 31.3 ± 2.65

Figure 4.13. Grouping of facies based on depositional time periods across Whidbey Island. Units with asterisks have radiocarbon or OSL dates included in the table on the lower left.

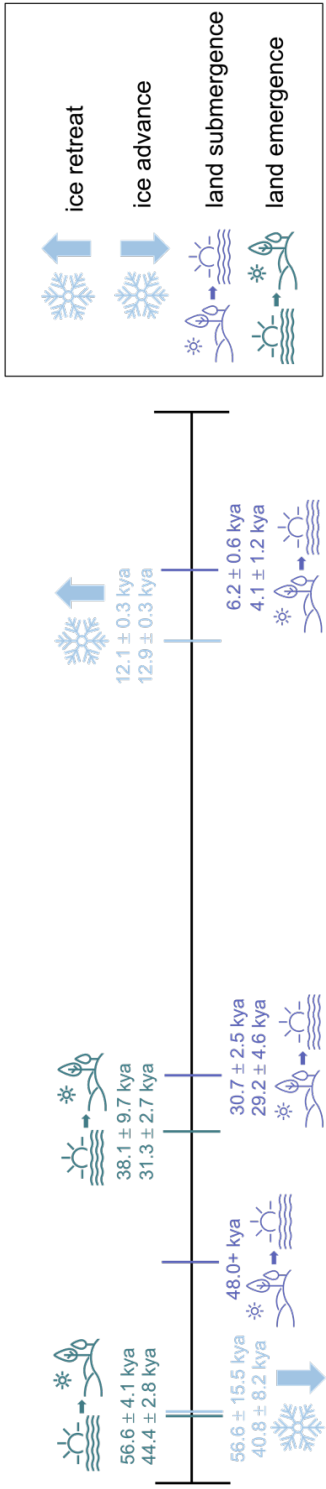


Figure 4.14. Timeline of newly developed geochronology and implications for overall landscape development and ice movement in the Puget Lowland.

Chapter 5: Concluding Remarks

5.1 Summary

This dissertation elucidates processes of glacial ice dynamics across spatially and temporally variable bed conditions. Utilizing deglaciated landscapes to infer ice sheet behavior provides keys for understanding contemporary ice sheets. The difficult-to-reach subglacial environments of modern ice sheets can be studied by using terrestrial analogs, as demonstrated herewithin.

Chapter 2 utilizes nine deglaciated sites across the northern hemisphere to explore the relationships between streaming ice behavior and subglacial topography and geology. The development of a semi-automated mapping tool to identify streamlined subglacial bedforms, used to infer paleo-ice speed, direction, and maturity is applicable across any landscape with elevation data, including regions recently or currently glaciated with proper subglacial elevation data (McKenzie et al., 2022). From the large dataset of subglacial streamlined bedform data collected for Chapter 2, the similar landform signatures seen across ice-streams of all topographic and geologic settings suggests that streamlined subglacial bedforms are being developed under all contemporary ice streams. Additionally, the finding of highest bedform elongation in topographically constrained regions suggests modern ice streams found in valleys or troughs, such as glaciers along the margins of Greenland (Figure 4.1) have higher ice streaming speeds than surrounding, topographically unconstrained areas (Eyles et al., 2018). Due to the first-order control of topography on ice streaming, in these regions controlled by topographic funneling, substrate properties will work to develop highly elongate bedforms at the ice-bed interface. Contrastingly, in regions with topographically unconstrained ice streams with sedimentary beds, we can expect to see persistent ice flow and well-developed erosional and depositional processes at the bed.

While numerical modeling assesses the role of often idealized subglacial topographic highs on ice-flow dynamics (e.g., Alley et al., 2021), Chapter 3 provides the first empirical evidence from the paleo-record to assess the influence of topographic highs in ice flow and subglacial dynamics within a single glacial system. Topographic bumps across the landscape glaciated by the southernmost Cordilleran Ice Sheet reduce ice-flow speed and spatial homogeneity of bed erosion and sediment transport and deposition, as a result of a subglacial lithology transition. An increase in sediment availability and basal meltwater, produced from strain heating on top of the bump (Payne and Dongelmans, 1997), manifests downstream as increased sediment transport efficiency seen in bedforms with homogenous surface relief (McIntyre, 1985; Pohjola and Hedfors, 2003; Winsborrow et al., 2010b). Beneath contemporary glacial systems such as Thwaites Glacier, models predict similar ice-flow response to subglacial topographic bumps (Alley et al., 2021), however the added understanding of the influence of multiple and variable size bumps on subglacial processes from this empirical study are highly useful in elucidating how sedimentation may also be able to contribute to potential contemporary ice-margin stabilization. In the paleo-record, the size of the topographic bump is seen to correlate

to bedform morphometrics, suggesting a threshold in which bump volume significantly slows ice flow or disrupts ice flow organization with only the largest bumps supporting later recovery of ice flow orientation and speed downstream of bumps. While the threshold of bump volume for this influence is not expected to be the same between all contemporary and paleo-systems, the identification that this threshold exists will be useful in identifying potential influence of subglacial topography on ice flow beneath modern ice sheets and glaciers.

The role of glacial isostatic adjustment (GIA) in addition to topographic variability is an important consideration in identifying styles of ice retreat and stability. In Chapter 4, the use of stratigraphic assessment, sedimentological analysis, and geochronological reconstruction to constrain landscape evolution of the Puget Lowland, glaciated by the southernmost CIS, provides empirical evidence of the interplay between GIA and topography as they collectively influence styles and timing of final ice retreat from the region. The Puget Lowland, with similar solid Earth rheology to that of the Antarctic Peninsula (Whitehouse et al., 2019; Nield et al., 2014), records rapid transitions between a subaerial and submarine environment were rapid enough to outpace a steadily increasing global mean sea level (Yokoyama & Purcell, 2021). While the southern part of the Puget Lobe was marine-terminating, as seen by the presence of carbonate shells in the depositional environment (Figure 4.5; 4.8), sedimentary records from northern Whidbey Island suggest ice retreat into a subaerial environment (Figure 4.11). Radiocarbon dates identifying marine-terminating ice stand-still on Whidbey Island for at least 1,000 years, consistent with the presence of GZWs, indicates step-wise retreat of this system (Demet et al., 2019; Simkins et al., 2018) rather than the previously hypothesized catastrophic retreat (Thorson, 1980, 1981; Waitt and Thorson, 1983; Booth, 1987; Booth et al., 2003). Identifying the style of retreat of the southernmost CIS with respect to rapid changes in landscape elevation from GIA has implications for the rate of possible retreat scenarios of glaciers on the Antarctic Peninsula and the role GIA can play in periodic ice-margin stabilization during ice retreat.

The use of preserved streamlined bedforms and sediment records from paleo-subglacial environments is highly beneficial to constraining subglacial process sensitivities to variable bed conditions (Eyles et al., 2018; Greenwood et al., 2021; King et al., 2009; Stokes & Clark 2001, 2002). The remarkable similarities between the environments and processes of both paleo and modern glacial dynamics ensure that work conducted on paleo-environments may be directly applicable to modern systems that are more difficult to study. Overall, this dissertation has major implications for the role of subglacial topography, lithology, and solid Earth dynamics on ice sheet behavior and may be widely used in the fields of glaciology, glacial geology, ice sheet modeling, geochronology, and paleoclimate studies.

5.2 Future Directions

The connections that can be made between paleo-glaciology and modern glaciology present a unique and exciting opportunity to extrapolate process-based knowledge into predicting

future ice sheet and glacier changes. Importantly, constraining ice-bed interactions across variable subglacial conditions aids in the range of potential ice-sheet sensitivity and responses in terms of flow organization and speed and retreat of ice margins. On broad landscape scales, the knowledge derived from Chapter 2 regarding location of bed deformation and ice streaming can be applied to state-of-the-art numerical ice-sheet models that integrate high-resolution topography, lithology, and sedimentary processes. For example, using stochastic modeling of paleo-subglacial environments (MacKie et al., 2020; MacKie et al., 2021) may elucidate subglacial topography and sedimentary processes beneath modern ice streams that are missed using *in situ*, on-ice observations that satellite-based remote sensing cannot capture. The impact of former ice flow behavior in the presence of local topographic bumps (Chapter 3) will provide test cases for numerical models and potentially allow for better targeting of suitable glaciated sites for *in situ* studies. Models that seek to constrain GIA influence on ice retreat may be compared to the empirical evidence of rapid landscape evolution under the southernmost CIS seen in Chapter 4. Additionally, the findings from Chapter 4 provide information that can be used to consider the accuracy of CIS models and overall timing of ice sheet collapse (e.g., Seguinot et al., 2014; Seguinot et al., 2016). Contributing to an understanding of glacial histories, especially the vastly under-studied CIS, will not only improve aforementioned paleo-climate modeling, but also support modeling of contemporary glacial loss by contributing process-based knowledge to analogous ice sheets. Constraining the past through a process-based lens is an innovative, resourceful way to assess the Earth system through geologic history and consider how these processes will contribute to evolution of glacial systems into the future.

With this work, I have developed a great appreciation for the importance of ice-bed interactions in constraining glacial dynamics. I have recognized a need for the development of process-based understanding to be incorporated into models of glacial behavior into the future. While ice-sheet models have limitations on the parameters they can use to make their predictions, there are still many limitations in understanding of how subglacial conditions hinder or help future ice loss to global sea level rise. My hope for future glaciology, geochronology, and geomorphology research is for the breadth of knowledge developed in these fields to be used to draw more direct connections between paleo and contemporary research -- a goal in which I strive to contribute in my future work as well.

Appendix A2

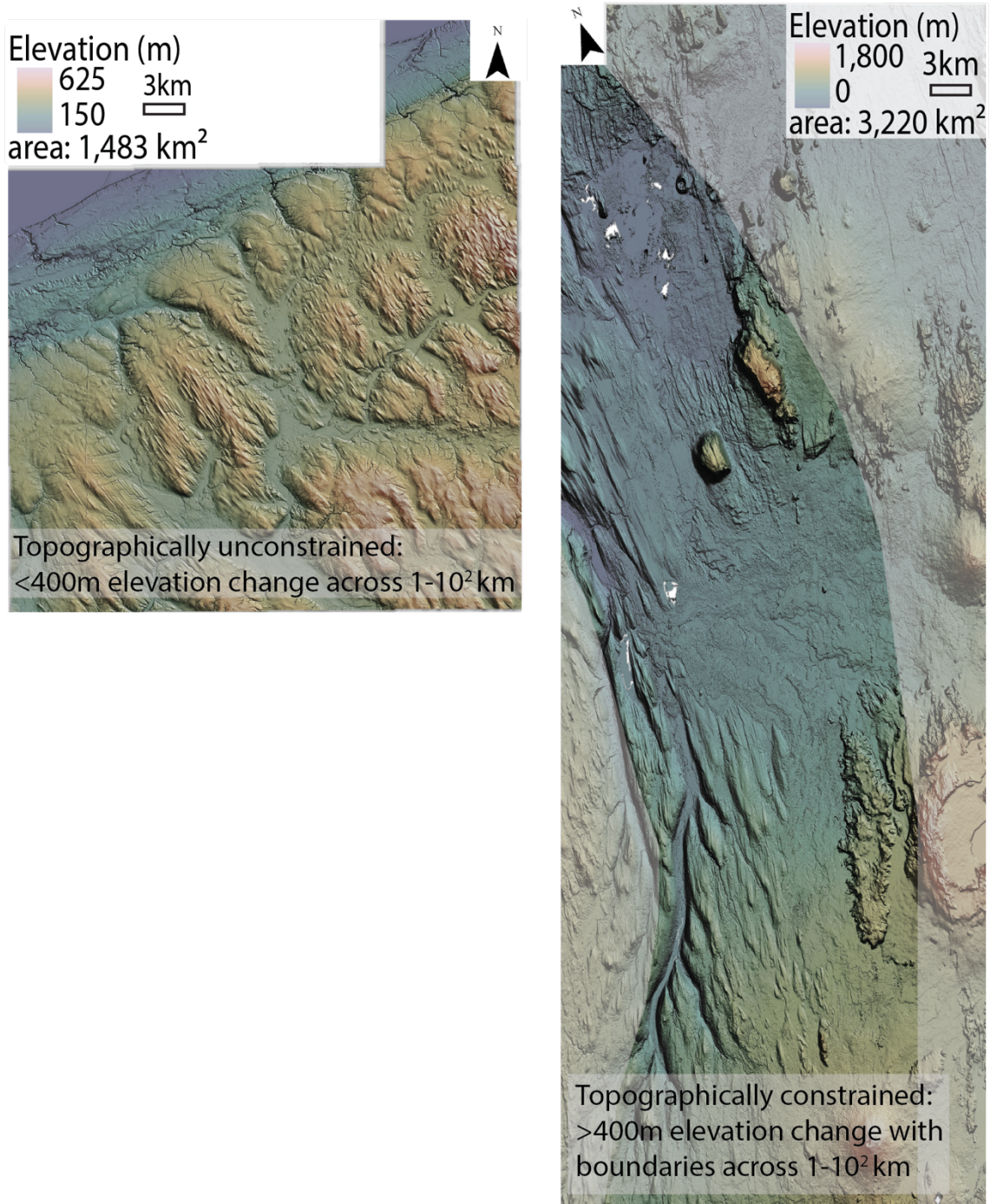


Figure A2.1. Examples of topographically unconstrained topography (A) in northwestern Pennsylvania (Site B) and topographically constrained topography (B) in Bárðardalur, Iceland (Site G). Gray areas in (B) indicate areas of higher topography and generally follow the valley wall boundary.

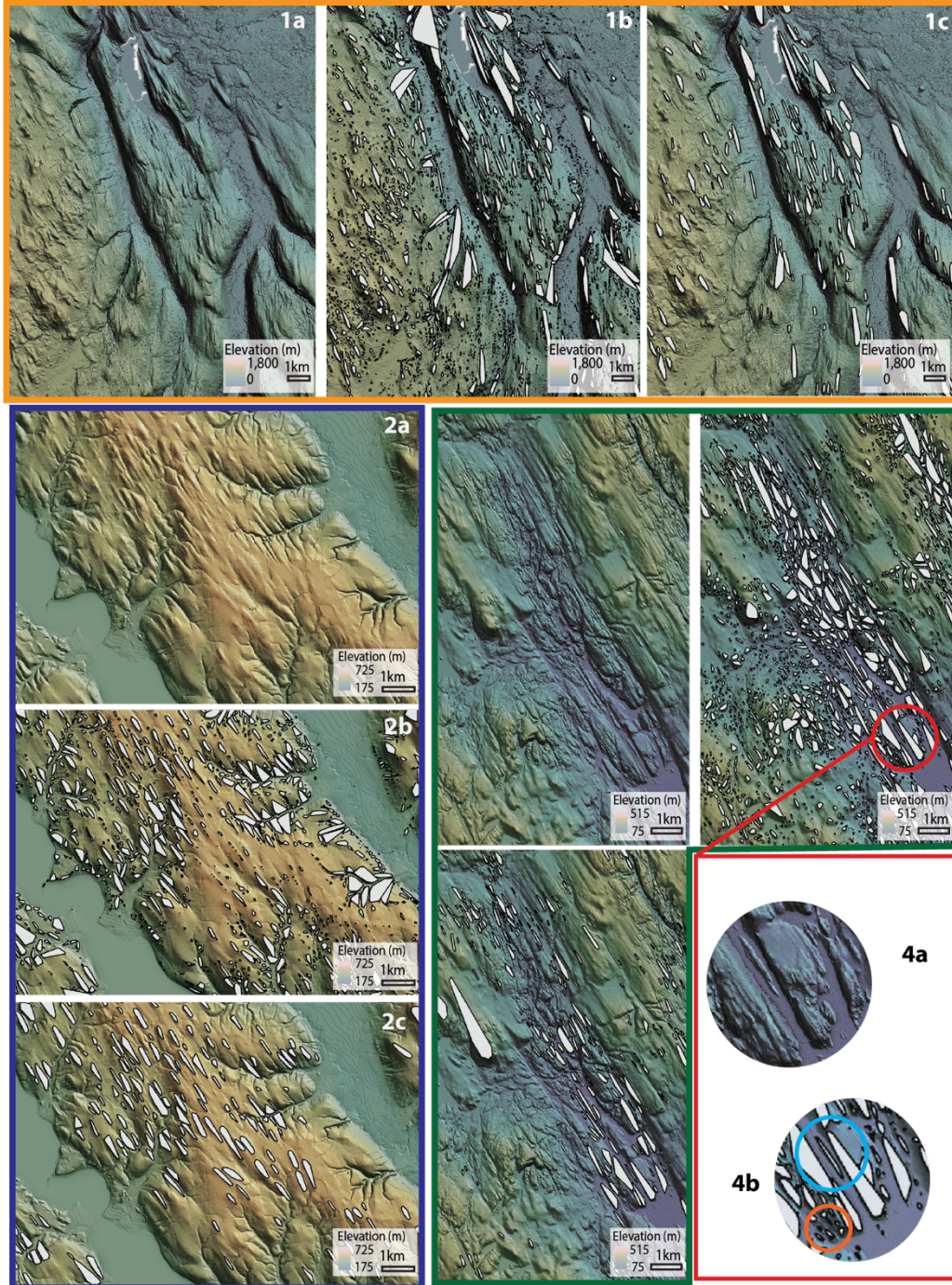


Figure A2.2. Examples of TPI applied to sites of each bed lithology, orange indicated volcanic bedrock at Site G, blue outline indicates sedimentary bedrock at Site C, green outline indicates crystalline bedrock at Site F. Images 1b, 2b, and 3b show TPI analysis before manual sorting: 1c, 2c, and 3c show final bedform mapping with both TPI and manual methods. Figure 4a Is the Site F DEM before mapping, the orange circle in 4b contains bedforms incorrectly identified by TPI due to under-identification, the blue circle in 4b contains one example of a bedform correctly identified by TPI.

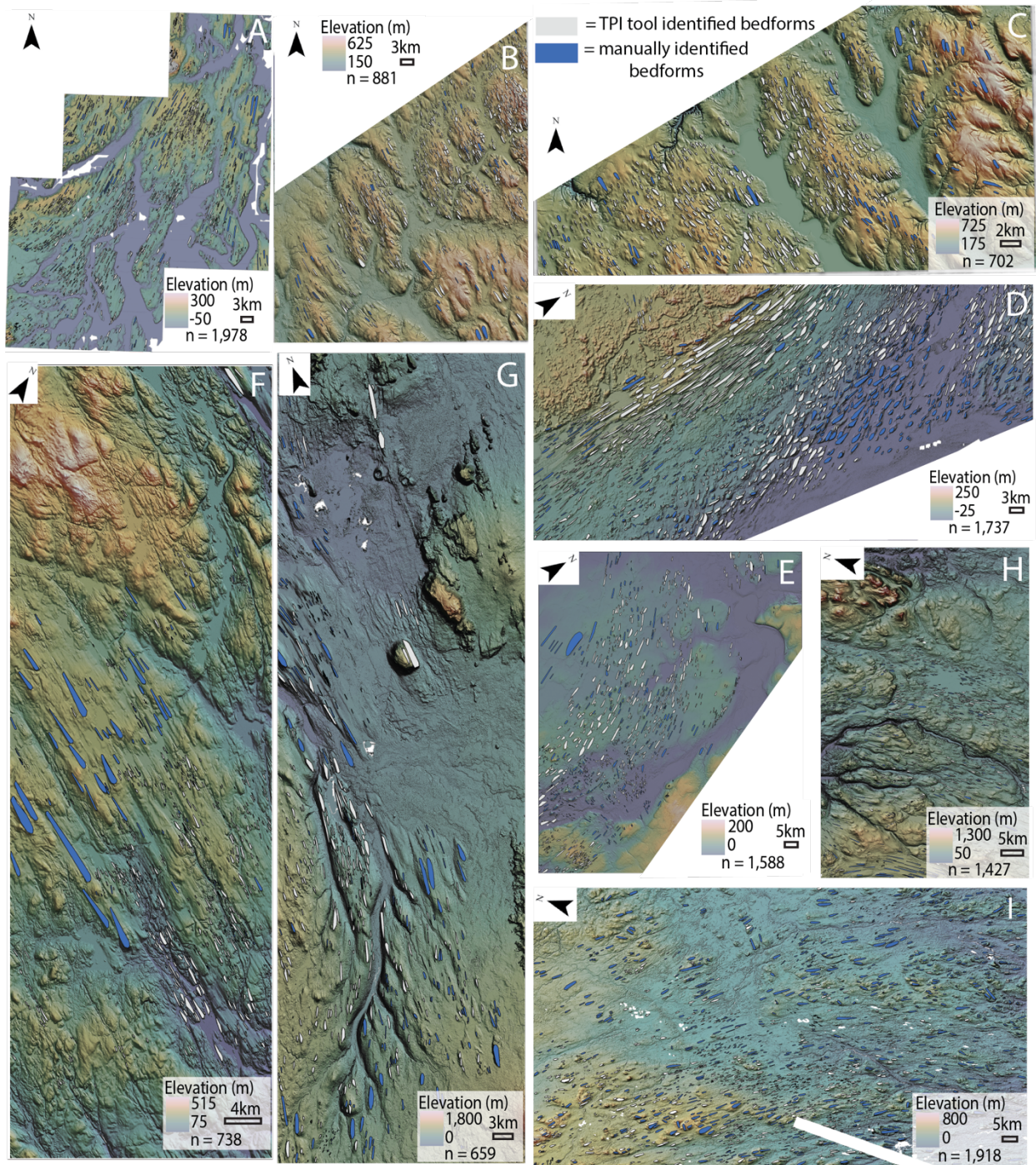


Figure A2.3. Streamlined subglacial bedforms identified by the TPI identification tool (gray polygons) and manually identified (blue polygons) at site (A) Puget Lowland, Washington, United States; (B) northwestern Pennsylvania, United States; (C) Chautauqua, New York, United States; (D) M'Clintock Channel, Canada; (E) Prince of Wales Island, Canada; (F) Nunavut, Canada; (G) Bárðardalur, Iceland; (H) Northern Norway; (I) Northern Sweden.

Appendix A4



Figure A4.1. A clay lamination seen in Unit 3 of Fort Casey Site 1 (left) and a silt lens seen in Unit 1 of Fort Casey Site 1(right). This distinction is maintained throughout all site stratigraphic descriptions.

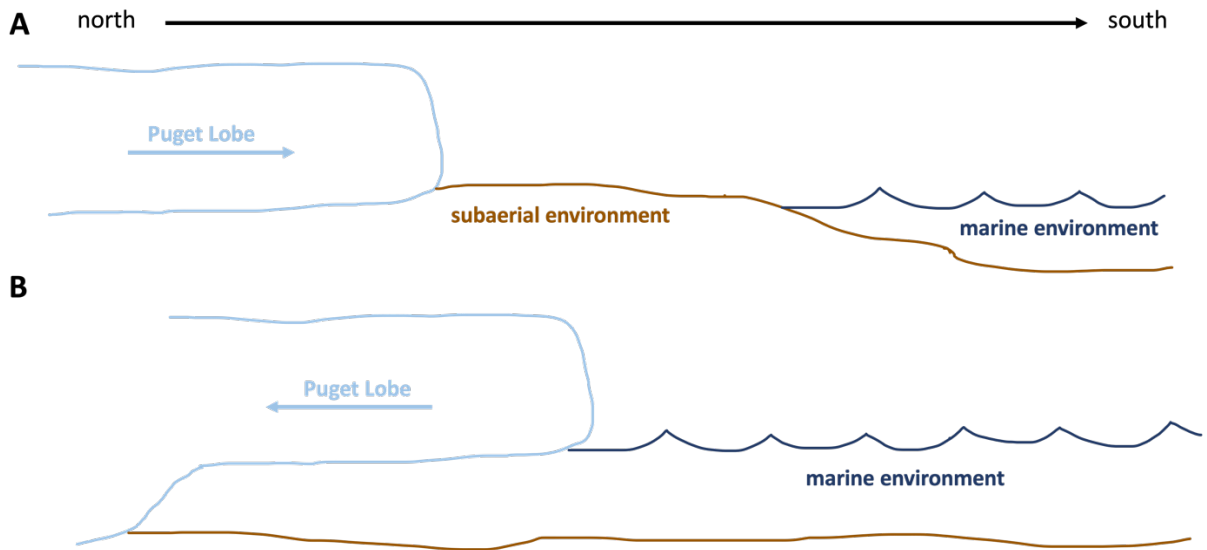


Figure A4.2. Schematic drawing of A) time 1 indicating Puget Lobe advance into subaerial Puget Lowland post landscape emergence (Figure 4.13). B) Indicates time 2 Puget Lobe ice retreat within a marine environment post landscape-submergence and marine-incurSION following time 1. Puget Lobe ice retreat in a marine environment only occurred at southernmost sites Double Bluff and Penn Cove (Figure 4.13).

References

- Alden, W.C. (1905) The drumlins of southeastern Wisconsin. United States Geological Survey Bulletin, 273, 1–46. Available from: <https://doi.org/10.3133/b273>
- Alley, R. B., Blankenship, D. D., Bentley, C. R., & Rooney, S. T. (1986). Deformation of till beneath ice stream B, West Antarctica. *Nature*, 322(6074), 57–59. <https://doi.org/10.1038/322057a0>
- Alley, R. B., Holschuh, N., MacAyeal, D. R., Parizek, B. R., Zoet, L., Riverman, K., Muto, A., Christianson, K., Clyne, E., Anandakrishnan, S., Stevens, N., & GHOST Collaboration. (2021). Bedforms of Thwaites Glacier, West Antarctica: Character and Origin. *Journal of Geophysical Research: Earth Surface*, 126(12). <https://doi.org/10.1029/2021JF006339>
- Anundsen, K., Abella, S., Leopold, E., Stuiver, M., & Turner, S. (1994). Late-Glacial and Early Holocene Sea-Level Fluctuations in the Central Puget Lowland, Washington, Inferred from Lake Sediments. *Quaternary Research*, 42(2), 149–161. <https://doi.org/10.1006/qres.1994.1064>
- Auclair, M., Lamothe, M., & Huot, S. (2003). Measurement of anomalous fading for feldspar IRSL using SAR. *Radiation Measurements*, 37(4), 487–492. [https://doi.org/10.1016/S1350-4487\(03\)00018-0](https://doi.org/10.1016/S1350-4487(03)00018-0)
- Bamber, J. L., Griggs, J. A., Hurkmans, R. T. W. L., Dowdeswell, J. A., Gogineni, S. P., Howat, I., Mouginot, J., Paden, J., Palmer, S., Rignot, E., & Steinhage, D. (2013). A new bed elevation dataset for Greenland. *The Cryosphere*, 7(2), 499–510. <https://doi.org/10.5194/tc-7-499-2013>
- Barbouti, A. I., & Rastin, B. C. (1983). A study of the absolute intensity of muons at sea level and under various thicknesses of absorber. *Journal of Physics G: Nuclear Physics*, 9(12), 1577. <https://doi.org/10.1088/0305-4616/9/12/018>
- Bassis, J. N., Petersen, S. V., & Mac Cathles, L. (2017). Heinrich events triggered by ocean forcing and modulated by isostatic adjustment. *Nature*, 542(7641), 332–334. <https://doi.org/10.1038/nature21069>
- Batchelor, C. L., & Dowdeswell, J. A. (2015). Ice-sheet grounding-zone wedges (GZWs) on high-latitude continental margins. *Marine Geology*, 363, 65–92. <https://doi.org/10.1016/j.margeo.2015.02.001>
- Benediktsson, Í. Ö., Aradóttir, N., Ingólfsson, Ó., & Brynjólfsson, S. (2022). Cross-cutting palaeo-ice streams in NE-Iceland reveal shifting Iceland Ice Sheet dynamics. *Geomorphology*, 396, 108009. <https://doi.org/10.1016/j.geomorph.2021.108009>
- Benediktsson, Í. Ö., Jónsson, S. A., Schomacker, A., Johnson, M. D., Ingólfsson, Ó., Zoet, L., Iverson, N. R., & Stötter, J. (2016). Progressive formation of modern drumlins at Múlajökull, Iceland: stratigraphical and morphological evidence. *Boreas*, 45(4), 567–583. <https://doi.org/10.1111/bor.12195>
- Benn, D. I., & Evans, D. J. A. (2010). *Glaciers & glaciation* (2nd ed). Hodder education.
- Booth, D. B. (1987). Timing and processes of deglaciation along the southern margin of the Cordilleran ice sheet. In W. F. Ruddiman & H. E. Wright (Eds.), *North America and Adjacent*

- Oceans During the Last Deglaciation* (pp. 71–90). Geological Society of America.
<https://doi.org/10.1130/DNAG-GNA-K3.71>
- Booth, D. B., & Hallet, B. (1993). Channel networks carved by subglacial water: Observations and reconstruction in the eastern Puget Lowland of Washington. *Geological Society of America Bulletin*, 105(5), 671–683. [https://doi.org/10.1130/0016-7606\(1993\)105<0671:CNCBSW>2.3.CO;2](https://doi.org/10.1130/0016-7606(1993)105<0671:CNCBSW>2.3.CO;2)
- Booth, D. B., Troost, K. G., Clague, J. J., & Waitt, R. B. (2003). The Cordilleran Ice Sheet. In *Developments in Quaternary Sciences* (Vol. 1, pp. 17–43). Elsevier.
[https://doi.org/10.1016/S1571-0866\(03\)01002-9](https://doi.org/10.1016/S1571-0866(03)01002-9)
- Booth, D. B., Troost, K. G., & Hagstrum, J. T. (2004). Deformation of Quaternary strata and its relationship to crustal folds and faults, south-central Puget Lowland, Washington State. *Geology*, 32(6), 505. <https://doi.org/10.1130/G20355.1>
- Bøtter-Jensen, L., & Murray, A. S. (1999). Developments in Optically Stimulated Luminescence Techniques for Dating and Retrospective Dosimetry. *Radiation Protection Dosimetry*, 84(1), 307–315. <https://doi.org/10.1093/oxfordjournals.rpd.a032745>
- Boulton, G. S., & Deynoux, M. (1981). Sedimentation in glacial environments and the identification of tills and tillites in ancient sedimentary sequences. *Precambrian Research*, 15(3–4), 397–422. [https://doi.org/10.1016/0301-9268\(81\)90059-0](https://doi.org/10.1016/0301-9268(81)90059-0)
- Bourgeois, O., Dauteuil, O., & Vliet-Lano, B. V. (2000). Geothermal control on flow patterns in the Last Glacial Maximum ice sheet of Iceland. *Earth Surface Processes and Landforms*, 25(1), 59–76. [https://doi.org/10.1002/\(SICI\)1096-9837\(200001\)25:1<59::AID-ESP48>3.0.CO;2-T](https://doi.org/10.1002/(SICI)1096-9837(200001)25:1<59::AID-ESP48>3.0.CO;2-T)
- Briner, J. P. (2007). Supporting evidence from the New York drumlin field that elongate subglacial bedforms indicate fast ice flow. *Boreas*, 36(2), 143–147.
<https://doi.org/10.1111/j.1502-3885.2007.tb01188.x>
- Cazenave, P. W., Lambkin, D. O., & Dix, J. K. (2008, September). Quantitative bedform analysis using decimetre resolution swath bathymetry. In *CARIS 2008 International User Group Conference*.
- Charlesworth, J.K. (1957) *The Quaternary Era: with special reference to its glaciation, vol. 1*. Edward Arnold Limited.
- Clallam County, Olympic Department of Natural Resources, Washington Department of Transportation. (2008). Puget Lowlands 2005 [data file]. Retrieved from <https://lidarportal.dnr.wa.gov/#47.85003:-122.92053:7>
- Clallam County, Olympic Department of Natural Resources, Washington Department of Transportation: Puget Lowlands 2005 [datafile]. Retrieved from <https://lidarportal.dnr.wa.gov/#47.85003:-122.92053:7>, 2008.
- Clark, C. D. (1993). Mega-scale glacial lineations and cross-cutting ice-flow landforms. *Earth Surface Processes and Landforms*, 18(1), 1–29. <https://doi.org/10.1002/esp.3290180102>

- Clark, C. D. (1997). Reconstructing the evolutionary dynamics of former ice sheets using multi-temporal evidence, remote sensing and GIS. *Quaternary Science Reviews*, 16(9), 1067–1092. [https://doi.org/10.1016/S0277-3791\(97\)00037-1](https://doi.org/10.1016/S0277-3791(97)00037-1)
- Clark, C. D. (1999). Glaciodynamic context of subglacial bedform generation and preservation. *Annals of Glaciology*, 28, 23–32. <https://doi.org/10.3189/172756499781821832>
- Clark, C. D. (2010). Emergent drumlins and their clones: from till dilatancy to flow instabilities. *Journal of Glaciology*, 56(200), 1011–1025. <https://doi.org/10.3189/002214311796406068>
- Clark, C. D., Ely, J. C., Spagnolo, M., Hahn, U., Hughes, A. L. C., & Stokes, C. R. (2018). Spatial organization of drumlins: Spatial organisation of drumlins. *Earth Surface Processes and Landforms*, 43(2), 499–513. <https://doi.org/10.1002/esp.4192>
- Clark, C. D., Evans, D. J. A., & Piotrowski, J. A. (2003). Palaeo-ice streams: an introduction. *Boreas*, 32(1), 1–3. <http://journalsonline.tandf.co.uk/openurl.asp?genre=article&id=doi:10.1080/03009480310001182>.
- Clark, C. D., Hughes, A. L. C., Greenwood, S. L., Spagnolo, M., & Ng, F. S. L. (2009). Size and shape characteristics of drumlins, derived from a large sample, and associated scaling laws. *Quaternary Science Reviews*, 28(7–8), 677–692. <https://doi.org/10.1016/j.quascirev.2008.08.035>
- Clark, P. U. (1994). Unstable Behavior of the Laurentide Ice Sheet over Deforming Sediment and Its Implications for Climate Change. *Quaternary Research*, 41(1), 19–25. <https://doi.org/10.1006/qres.1994.1002>
- Clarke, G. K. C., Nitsan, U., & Paterson, W. S. B. (1977). Strain heating and creep instability in glaciers and ice sheets. *Reviews of Geophysics*, 15(2), 235. <https://doi.org/10.1029/RG015i002p00235>
- Cuffey, K., & Paterson, W. S. B. (2010). *The physics of glaciers* (4th ed). Butterworth-Heinemann/Elsevier.
- De Rydt, J., Gudmundsson, G. H., Corr, H. F. J., & Christoffersen, P. (2013). Surface undulations of Antarctic ice streams tightly controlled by bedrock topography. *The Cryosphere*, 7(2), 407–417. <https://doi.org/10.5194/tc-7-407-2013>
- Demet, B. P., Nittrouer, J. A., Anderson, J. B., & Simkins, L. M. (2019). Sedimentary processes at ice sheet grounding-zone wedges revealed by outcrops, Washington State (USA). *Earth Surface Processes and Landforms*, 44(6), 1209–1220. <https://doi.org/10.1002/esp.4550>
- Dethier, D. P., Pessl, F., Keuler, R. F., Balzarini, M. A., & Pevear, D. R. (1995). Late Wisconsinan glaciomarine deposition and isostatic rebound, northern Puget Lowland, Washington. *Geological Society of America Bulletin*, 107(11), 1288–1303. [https://doi.org/10.1130/0016-7606\(1995\)107<1288:LWGD&I>2.3.CO;2](https://doi.org/10.1130/0016-7606(1995)107<1288:LWGD&I>2.3.CO;2)
- Dowling, T. P. F., Spagnolo, M., & Möller, P. (2015). Morphometry and core type of streamlined bedforms in southern Sweden from high resolution LiDAR. *Geomorphology*, 236, 54–63. <https://doi.org/10.1016/j.geomorph.2015.02.018>

- Duller, G. A. T. (2003). Distinguishing quartz and feldspar in single grain luminescence measurements. *Radiation Measurements*, 37(2), 161–165. [https://doi.org/10.1016/S1350-4487\(02\)00170-1](https://doi.org/10.1016/S1350-4487(02)00170-1)
- Duller G.A.T. (2013). Luminescence Analyst, 4.11 ed, Aberystwyth University.
- Duller, G.A.T. (2015). Luminescence dating. In W.J. Rink, & J.W. Thompson (Eds.), *Encyclopedia of Scientific Dating Methods* (pp. 390-404). (Encyclopedia of Earth Science Series). Springer Nature.
- Domack, E.W. (1984). Rhythmically Bedded Glaciomarine Sediments on Whidbey Island, Washington. *SEPM Journal of Sedimentary Research*, Vol. 54. <https://doi.org/10.1306/212F847C-2B24-11D7-8648000102C1865D>
- Durand, G., Gagliardini, O., Favier, L., Zwinger, T., & Le Meur, E. (2011). Impact of bedrock description on modeling ice sheet dynamics: BEDROCK DESCRIPTION TO MODEL ICE SHEET. *Geophysical Research Letters*, 38(20), n/a-n/a. <https://doi.org/10.1029/2011GL048892>
- Easterbrook, D. J. (1992). Advance and Retreat of Cordilleran Ice Sheets in Washington, U.S.A. *Géographie Physique et Quaternaire*, 46(1), 51–68. <https://doi.org/10.7202/032888ar>
- Ebert, K., Hall, A.M. & Hättestrand, C. (2012) Pre-glacial landforms on a glaciated shield: the inselberg plains of northern Sweden. *Norwegian Journal of Geology*, 92, 1–18.
- Ehlers, J., Gibbard, P. L., & Hughes, P. D. (2018). Quaternary Glaciations and Chronology. In *Past Glacial Environments* (pp. 77–101). Elsevier. <https://doi.org/10.1016/B978-0-08-100524-8.00003-8>
- Ely, J. C., Clark, C. D., Spagnolo, M., Stokes, C. R., Greenwood, S. L., Hughes, A. L. C., Dunlop, P., & Hess, D. (2016). Do subglacial bedforms comprise a size and shape continuum? *Geomorphology*, 257, 108–119. <https://doi.org/10.1016/j.geomorph.2016.01.001>
- Enderlin, E. M., Howat, I. M., Jeong, S., Noh, M., Van Angelen, J. H., & Van Den Broeke, M. R. (2014). An improved mass budget for the Greenland ice sheet. *Geophysical Research Letters*, 41(3), 866–872. <https://doi.org/10.1002/2013GL059010>
- Evans, D. J. A., Phillips, E. R., Hiemstra, J. F., & Auton, C. A. (2006). Subglacial till: Formation, sedimentary characteristics and classification. *Earth-Science Reviews*, 78(1–2), 115–176. <https://doi.org/10.1016/j.earscirev.2006.04.001>
- Eyles, N., Arbelaez Moreno, L., & Sookhan, S. (2018). Ice streams of the Late Wisconsin Cordilleran Ice Sheet in western North America. *Quaternary Science Reviews*, 179, 87–122. <https://doi.org/10.1016/j.quascirev.2017.10.027>
- Eyles, N., & Doughty, M. (2016). Glacially-streamlined hard and soft beds of the paleo- Ontario ice stream in Southern Ontario and New York state. *Sedimentary Geology*, 338, 51–71. <https://doi.org/10.1016/j.sedgeo.2016.01.019>
- Falcini, F. A. M., Rippin, D. M., Krabbendam, M., & Selby, K. A. (2018). Quantifying bed roughness beneath contemporary and palaeo-ice streams. *Journal of Glaciology*, 64(247), 822–834. <https://doi.org/10.1017/jog.2018.71>

- Favier, L., Pattyn, F., Berger, S., & Drews, R. (2016). Dynamic influence of pinning points on marine ice-sheet stability: a numerical study in Dronning Maud Land, East Antarctica. *The Cryosphere*, 10(6), 2623–2635. <https://doi.org/10.5194/tc-10-2623-2016>
- Fowler, A. C. (2010). The formation of subglacial streams and mega-scale glacial lineations. *Proceedings of the Royal Society A: Mathematical, Physical and Engineering Sciences*, 466(2123), 3181–3201. <https://doi.org/10.1098/rspa.2010.0009>
- Fürst, J. J., Durand, G., Gillet-Chaulet, F., Tavard, L., Rankl, M., Braun, M., & Gagliardini, O. (2016). The safety band of Antarctic ice shelves. *Nature Climate Change*, 6(5), 479–482. <https://doi.org/10.1038/nclimate2912>
- Galbraith, R. F., Roberts, R. G., Laslett, G. M., Yoshida, H., & Olley, J. M. (1999). Optical dating of single and multiple grains of quartz from Jinmium rock shelter, Northern Australia: Prt 1, Experimental design and statistical models. *Archaeometry*, 41(2), 339–364. <https://doi.org/10.1111/j.1475-4754.1999.tb00987.x>
- Goebel, T., Waters, M. R., & O'Rourke, D. H. (2008). The Late Pleistocene Dispersal of Modern Humans in the Americas. *Science*, 319(5869), 1497–1502. <https://doi.org/10.1126/science.1153569>
- Goehring, B. M., Wilson, J., & Nichols, K. (2019). A fully automated system for the extraction of in situ cosmogenic carbon-14 in the Tulane University cosmogenic nuclide laboratory. *Nuclear Instruments and Methods in Physics Research Section B: Beam Interactions with Materials and Atoms*, 455, 284–292. <https://doi.org/10.1016/j.nimb.2019.02.006>
- Gomez, N., Pollard, D., Mitrovica, J. X., Huybers, P., & Clark, P. U. (2012). Evolution of a coupled marine ice sheet-sea level model: COUPLED ICE SHEET, SEA LEVEL MODEL. *Journal of Geophysical Research: Earth Surface*, 117(F1), n/a-n/a. <https://doi.org/10.1029/2011JF002128>
- Greenwood, S. L., & Clark, C. D. (2010). The sensitivity of subglacial bedform size and distribution to substrate lithological control. *Sedimentary Geology*, 232(3), 130–144. <https://doi.org/10.1016/j.sedgeo.2010.01.009>
- Greenwood, S. L., Simkins, L. M., Halberstadt, A. R. W., Prothro, L. O., & Anderson, J. B. (2018). Holocene reconfiguration and readvance of the East Antarctic Ice Sheet. *Nature Communications*, 9(1), 3176. <https://doi.org/10.1038/s41467-018-05625-3>
- Greenwood, S. L., Simkins, L. M., Winsborrow, M. C. M., & Bjarnadóttir, L. R. (2021). Exceptions to bed-controlled ice sheet flow and retreat from glaciated continental margins worldwide. *Science Advances*, 7(3), eabb6291. <https://doi.org/10.1126/sciadv.abb6291>
- Guérin, G., Mercier, N., Adamiec, G., (2011). Dose-rate conversion factors: update. *Ancient TL* 29(1), 5-8.
- Halberstadt, A. R. W., Simkins, L. M., Greenwood, S. L., & Anderson, J. B. (2016). Past ice-sheet behaviour: retreat scenarios and changing controls in the Ross Sea, Antarctica. *The Cryosphere*, 10(3), 1003–1020. <https://doi.org/10.5194/tc-10-1003-2016>

- Hall, A. M., Ebert, K., & Hättestrand, C. (2013). Pre-glacial landform inheritance in a glaciated shield landscape. *Geografiska Annaler: Series A, Physical Geography*, 95(1), 33–49. <https://doi.org/10.1111/j.1468-0459.2012.00477.x>
- Hall, A. M., & Glasser, N. F. (2003). Reconstructing the basal thermal regime of an ice stream in a landscape of selective linear erosion: Glen Avon, Cairngorm Mountains, Scotland. *Boreas*, 32(1), 191–207. <https://doi.org/10.1111/j.1502-3885.2003.tb01437.x>
- Hatfield, R. G., Stoner, J. S., Reilly, B. T., Tepley, F. J., Wheeler, B. H., & Housen, B. A. (2017). Grain size dependent magnetic discrimination of Iceland and South Greenland terrestrial sediments in the northern North Atlantic sediment record. *Earth and Planetary Science Letters*, 474, 474–489. <https://doi.org/10.1016/j.epsl.2017.06.042>
- Hättestrand, C., Götz, S., Näslund, J., Fabel, D., & Stroeven, A. P. (2004). Drumlin formation time: evidence from northern and central Sweden. *Geografiska Annaler: Series A, Physical Geography*, 86(2), 155–167. <https://doi.org/10.1111/j.0435-3676.2004.00221.x>
- Heaton, T. J., Köhler, P., Butzin, M., Bard, E., Reimer, R. W., Austin, W. E. N., Bronk Ramsey, C., Grootes, P. M., Hughen, K. A., Kromer, B., Reimer, P. J., Adkins, J., Burke, A., Cook, M. S., Olsen, J., & Skinner, L. C. (2020). Marine20—The Marine Radiocarbon Age Calibration Curve (0–55,000 cal BP). *Radiocarbon*, 62(4), 779–820. <https://doi.org/10.1017/RDC.2020.68>
- Hindmarsh, R. C. A. (2001). Influence of channelling on heating in ice-sheet flows. *Geophysical Research Letters*, 28(19), 3681–3684. <https://doi.org/10.1029/2000GL012666>
- Hindmarsh, R. C. A., & Meur, E. L. (2001). Dynamical processes involved in the retreat of marine ice sheets. *Journal of Glaciology*, 47(157), 271–282. <https://doi.org/10.3189/172756501781832269>
- Hoffmann, H. (2015) violin.m - Simple violin plot using matlab default kernel density estimation. INRES (University of Bonn), Katzenburgweg 5, 53115 Germany. hhoffmann@uni-bonn.de
- Hollingworth, S. E. (1931). The Glaciation of Western Edenside and Adjoining Areas and the Drumlins of Edenside and the Solway Basin. *Quarterly Journal of the Geological Society*, 87(1–4), 281–359. <https://doi.org/10.1144/GSL.JGS.1931.087.01-04.12>
- Hughes, A. L. C., Clark, C. D., & Jordan, C. J. (2010). Subglacial bedforms of the last British Ice Sheet. *Journal of Maps*, 6(1), 543–563. <https://doi.org/10.4113/jom.2010.1111>
- Hughes, P. D., Gibbard, P. L., & Ehlers, J. (2013). Timing of glaciation during the last glacial cycle: evaluating the concept of a global ‘Last Glacial Maximum’ (LGM). *Earth-Science Reviews*, 125, 171–198. <https://doi.org/10.1016/j.earscirev.2013.07.003>
- Ignéczi, Á., Sole, A. J., Livingstone, S. J., Ng, F. S. L., & Yang, K. (2018). Greenland Ice Sheet Surface Topography and Drainage Structure Controlled by the Transfer of Basal Variability. *Frontiers in Earth Science*, 6. <https://www.frontiersin.org/articles/10.3389/feart.2018.00101>
- Jamieson, S. S. R., Vieli, A., Livingstone, S. J., Cofaigh, C. Ó., Stokes, C., Hillenbrand, C.-D., & Dowdeswell, J. A. (2012). Ice-stream stability on a reverse bed slope. *Nature Geoscience*, 5(11), 799–802. <https://doi.org/10.1038/ngeo1600>

- Jones, R. S., Whitmore, R. J., Mackintosh, A. N., Norton, K. P., Eaves, S. R., Stutz, J., & Christl, M. (2020). Regional-scale abrupt Mid-Holocene ice sheet thinning in the western Ross Sea, Antarctica. *Geology*, *49*(3), 278–282. <https://doi.org/10.1130/G48347.1>
- Khazaradze, G., Qamar, A., & Dragert, H. (1999). Tectonic deformation in western Washington from continuous GPS measurements. *Geophysical Research Letters*, *26*(20), 3153–3156. <https://doi.org/10.1029/1999GL010458>
- King, E. C., Hindmarsh, R. C. A., & Stokes, C. R. (2009). Formation of mega-scale glacial lineations observed beneath a West Antarctic ice stream. *Nature Geoscience*, *2*(8), 585–588. <https://doi.org/10.1038/ngeo581>
- King, G. E., Robinson, R. A. J., & Finch, A. A. (2014). Towards successful OSL sampling strategies in glacial environments: deciphering the influence of depositional processes on bleaching of modern glacial sediments from Jostedal, Southern Norway. *Quaternary Science Reviews*, *89*, 94–107. <https://doi.org/10.1016/j.quascirev.2014.02.001>
- Kleman, J., & Borgström, I. (1996). RECONSTRUCTION OF PALAEO-ICE SHEETS: THE USE OF GEOMORPHOLOGICAL DATA. *Earth Surface Processes and Landforms*, *21*(10), 893–909. [https://doi.org/10.1002/\(SICI\)1096-9837\(199610\)21:10<893::AID-ESP620>3.0.CO;2-U](https://doi.org/10.1002/(SICI)1096-9837(199610)21:10<893::AID-ESP620>3.0.CO;2-U)
- Kleman, J., Httestrand, C., Stroeven, A. P., Jansson, K. N., De Angelis, H., & Borgström, I. (2006). Reconstruction of Palaeo-Ice Sheets - Inversion of their Glacial Geomorphological Record. In P. G. Knight (Ed.), *Glacier Science and Environmental Change* (pp. 192–198). Blackwell Publishing. <https://doi.org/10.1002/9780470750636.ch38>
- Kleman, J., & Stroeven, A. P. (1997). Preglacial surface remnants and Quaternary glacial regimes in northwestern Sweden. *Geomorphology*, *19*(1), 35–54. [https://doi.org/10.1016/S0169-555X\(96\)00046-3](https://doi.org/10.1016/S0169-555X(96)00046-3)
- KOMAR, P. (1977). BEACH PROCESSES AND SEDIMENTATION. *BEACH PROCESSES AND SEDIMENTATION*.
- Kovanen, D. J., & Slaymaker, O. (2004). Relict Shorelines and Ice Flow Patterns of the Northern Puget Lowland from Lidar Data and Digital Terrain Modelling. *Geografiska Annaler. Series A, Physical Geography*, *86*(4), 385–400. <https://www.jstor.org/stable/3566155>
- Krabbendam, M., Eyles, N., Putkinen, N., Bradwell, T., & Arbelaez-Moreno, L. (2016). Streamlined hard beds formed by palaeo-ice streams: A review. *Sedimentary Geology*, *338*, 24–50. <https://doi.org/10.1016/j.sedgeo.2015.12.007>
- Leopold, E. B., Nickmann, R., Hedges, J. I., & Ertel, J. R. (1982). Pollen and Lignin Records of Late Quaternary Vegetation, Lake Washington. *Science*, *218*(4579), 1305–1307. <https://doi.org/10.1126/science.218.4579.1305>
- Lesnek, A. J., Briner, J. P., Lindqvist, C., Baichtal, J. F., & Heaton, T. H. (2018). Deglaciation of the Pacific coastal corridor directly preceded the human colonization of the Americas. *Science Advances*, *4*(5), eaar5040. <https://doi.org/10.1126/sciadv.aar5040>
- Linton, D. L. (1963). The Forms of Glacial Erosion. *Transactions and Papers (Institute of British Geographers)*, *33*, 1–28. <https://doi.org/10.2307/620998>

- Livingstone, S. J., Stokes, C. R., Cofaigh, C. Ó., Hillenbrand, C.-D., Vieli, A., Jamieson, S. S. R., Spagnolo, M., & Dowdeswell, J. A. (2016). Subglacial processes on an Antarctic ice stream bed. 1: Sediment transport and bedform genesis inferred from marine geophysical data. *Journal of Glaciology*, *62*(232), 270–284. <https://doi.org/10.1017/jog.2016.18>
- MacKie, E. J., Schroeder, D. M., Caers, J., Siegfried, M. R., & Scheidt, C. (2020). Antarctic Topographic Realizations and Geostatistical Modeling Used to Map Subglacial Lakes. *Journal of Geophysical Research: Earth Surface*, *125*(3). <https://doi.org/10.1029/2019JF005420>
- MacKie, E. J., Schroeder, D. M., Zuo, C., Yin, Z., & Caers, J. (2021). Stochastic modeling of subglacial topography exposes uncertainty in water routing at Jakobshavn Glacier. *Journal of Glaciology*, *67*(261), 75–83. <https://doi.org/10.1017/jog.2020.84>
- Maier, N., Humphrey, N., Harper, J., & Meierbachtol, T. (2019). Sliding dominates slow-flowing margin regions, Greenland Ice Sheet. *Science Advances*, *5*(7), eaaw5406. <https://doi.org/10.1126/sciadv.aaw5406>
- Mandryk, C. A. S., Josenhans, H., Fedje, D. W., & Mathewes, R. W. (2001). Late Quaternary paleoenvironments of Northwestern North America: implications for inland versus coastal migration routes. *Quaternary Science Reviews*, *20*(1), 301–314. [https://doi.org/10.1016/S0277-3791\(00\)00115-3](https://doi.org/10.1016/S0277-3791(00)00115-3)
- Margold, M., Stokes, C. R., & Clark, C. D. (2015). Ice streams in the Laurentide Ice Sheet: Identification, characteristics and comparison to modern ice sheets. *Earth-Science Reviews*, *143*, 117–146. <https://doi.org/10.1016/j.earscirev.2015.01.011>
- Margold, M., Stokes, C. R., & Clark, C. D. (2018). Reconciling records of ice streaming and ice margin retreat to produce a palaeogeographic reconstruction of the deglaciation of the Laurentide Ice Sheet. *Quaternary Science Reviews*, *189*, 1–30. <https://doi.org/10.1016/j.quascirev.2018.03.013>
- McIntyre, N. F. (1985). The Dynamics of Ice-Sheet Outlets. *Journal of Glaciology*, *31*(108), 99–107. <https://doi.org/10.3189/S0022143000006328>
- McKenzie, M. A., Simkins, L. M., Principato, S. M., & Munevar Garcia, S. (2022). Streamlined subglacial bedform sensitivity to bed characteristics across the deglaciated Northern Hemisphere. *Earth Surface Processes and Landforms*, *47*(9), 2341–2356. <https://doi.org/10.1002/esp.5382>
- McKenzie, M. A., Simkins, L. M., Slawson, J. S., MacKie, E. J., & Wang, S. (2022). *Differential impact of isolated topographic bumps on glacial ice flow and subglacial processes* [Preprint]. Glaciers/Subglacial Processes. <https://doi.org/10.5194/egusphere-2022-1220>
- McKenzie, Marion A, Simkins, Lauren M, & Principato, Sarah M. (2022). *Streamlined subglacial bedforms across the deglaciated Northern Hemisphere*. PANGAEA. <https://doi.org/10.1594/PANGAEA.939999>
- McKenzie, Marion A, Simkins, Lauren M, Slawson, Jacob S, & Wang, Shujie. (2023). *Streamlined subglacial bedforms across isolated topographic highs in the Puget Lowland, Washington state*. PANGAEA. <https://doi.org/10.1594/PANGAEA.954529>

- Menzies, J. (1979). A review of the literature on the formation and location of drumlins. *Earth-Science Reviews*, 14(4), 315–359. [https://doi.org/10.1016/0012-8252\(79\)90093-X](https://doi.org/10.1016/0012-8252(79)90093-X)
- Morlighem, M., Rignot, E., Binder, T., Blankenship, D., Drews, R., Eagles, G., Eisen, O., Ferraccioli, F., Forsberg, R., Fretwell, P., Goel, V., Greenbaum, J. S., Gudmundsson, H., Guo, J., Helm, V., Hofstede, C., Howat, I., Humbert, A., Jokat, W., ... Young, D. A. (2020). Deep glacial troughs and stabilizing ridges unveiled beneath the margins of the Antarctic ice sheet. *Nature Geoscience*, 13(2), 132–137. <https://doi.org/10.1038/s41561-019-0510-8>
- Morlighem, M., Rignot, E., Mouginit, J., Seroussi, H., & Larour, E. (2014). Deeply incised submarine glacial valleys beneath the Greenland ice sheet. *Nature Geoscience*, 7(6), 418–422. <https://doi.org/10.1038/ngeo2167>
- Murray, A. S., & Wintle, A. G. (2000). Luminescence dating of quartz using an improved single-aliquot regenerative-dose protocol. *Radiation Measurements*, 32(1), 57–73. [https://doi.org/10.1016/S1350-4487\(99\)00253-X](https://doi.org/10.1016/S1350-4487(99)00253-X)
- Ng, F. (1998). *Mathematical modelling of subglacial drainage and erosion*. <https://ora.ox.ac.uk/objects/uuid:346ee63c-a176-4381-aafb-980057dd6f5c>
- Nield, G. A., Barletta, V. R., Bordon, A., King, M. A., Whitehouse, P. L., Clarke, P. J., Domack, E., Scambos, T. A., & Berthier, E. (2014). Rapid bedrock uplift in the Antarctic Peninsula explained by viscoelastic response to recent ice unloading. *Earth and Planetary Science Letters*, 397, 32–41. <https://doi.org/10.1016/j.epsl.2014.04.019>
- Nienow, P. W., Sole, A. J., Slater, D. A., & Cowton, T. R. (2017). Recent Advances in Our Understanding of the Role of Meltwater in the Greenland Ice Sheet System. *Current Climate Change Reports*, 3(4), 330–344. <https://doi.org/10.1007/s40641-017-0083-9>
- Ó Cofaigh, C., Stokes, C. R., Lian, O. B., Clark, C. D., & Tulaczyk, S. (2013). Formation of mega-scale glacial lineations on the Dubawnt Lake Ice Stream bed: 2. Sedimentology and stratigraphy. *Quaternary Science Reviews*, 77, 210–227. <https://doi.org/10.1016/j.quascirev.2013.06.028>
- OCM Partners: 2017 USGS Lidar: Olympic Peninsula, WA from 2010-06-15 to 2010-08-15, NOAA National Centers for Environmental Information [datafile], <https://www.fisheries.noaa.gov/inport/item/59232>, 2019a.
- OCM Partners: 2019 WA DNR Lidar: San Juan County, WA from 2010-06-15 to 2010-08-15, NOAA National Centers for Environmental Information [datafile], <https://www.fisheries.noaa.gov/inport/item/67199>, 2019b.
- Ottesen, D., Stokes, C. R., Rise, L., & Olsen, L. (2008). Ice-sheet dynamics and ice streaming along the coastal parts of northern Norway. *Quaternary Science Reviews*, 27(9–10), 922–940. <https://doi.org/10.1016/j.quascirev.2008.01.014>
- Payne, A. J., & Dongelmans, P. W. (1997). Self-organization in the thermomechanical flow of ice sheets. *Journal of Geophysical Research: Solid Earth*, 102(B6), 12219–12233. <https://doi.org/10.1029/97JB00513>
- Pessl Jr., F., Dethier, D.P., Keuler, R.F., Minard, J.P., & Balzarini, M.A. (1981). Sedimentary facies and depositional environments of late Wisconsin glacial-marine deposits

- in the central Puget Lowland, Washington. American Association Petroleum Geologists, Abstracts, Ann. Meeting, San Francisco.
- Podolskiy, E. A., & Walter, F. (2016). Cryoseismology: CRYOSEISMOLOGY. *Reviews of Geophysics*, 54(4), 708–758. <https://doi.org/10.1002/2016RG000526>
- Pohjola, V. A., & Hedfors, J. (2003). Studying the effects of strain heating on glacial flow within outlet glaciers from the Heimefrontfjella Range, Dronning Maud Land, Antarctica. *Annals of Glaciology*, 37, 134–142. <https://doi.org/10.3189/172756403781815843>
- Porter, S. C., & Swanson, T. W. (1998). Radiocarbon Age Constraints on Rates of Advance and Retreat of the Puget Lobe of the Cordilleran Ice Sheet during the Last Glaciation. *Quaternary Research*, 50(3), 205–213. <https://doi.org/10.1006/qres.1998.2004>
- Powell, R.D. (1980). Holocene glacial marine deposition by tide-water glaciers in Glacier Bay, Alaska [unpublished Ph.D. thesis]. Ohio State University.
- Prescott, J. R., & Stephan, L. G. (1982). The contribution of cosmic radiation to the environmental dose for thermoluminescence dating. *PACT*, 6, 17–25. <https://cir.nii.ac.jp/crid/1573668924373277824>
- Prescott, J. R., & Hutton, J. T. (1994). Cosmic ray contributions to dose rates for luminescence and ESR dating: Large depths and long-term time variations. *Radiation Measurements*, 23(2), 497–500. [https://doi.org/10.1016/1350-4487\(94\)90086-8](https://doi.org/10.1016/1350-4487(94)90086-8)
- Principato, S. M., Moyer, A. N., Hampsch, A. G., & Ipsen, H. A. (2016). Using GIS and streamlined landforms to interpret palaeo-ice flow in northern Iceland. *Boreas*, 45(3), 470–482. <https://doi.org/10.1111/bor.12164>
- Quantum Spatial, Inc. (2017). Western Washington 3DEP LiDAR, United States Geological Survey [datafile], https://gismaps.snoco.org/metadata/topography/Western_Washington_3DEP_Technical_Data_Report.pdf.
- Quantum Spatial, Inc. (2019). Olympic Peninsula, Washington 3DEP LiDAR, United States Geological Survey [datafile], https://coast.noaa.gov/htdata/lidar3_z/geoid18/data/9072/supplemental/Olympic_Peninsula_3DEP_Area_1_LiDAR_Technical_Data_Report_revised_110419.pdf.
- Reilly, B. T., Stoner, J. S., Mix, A. C., Walczak, M. H., Jennings, A., Jakobsson, M., Dyke, L., Glueder, A., Nicholls, K., Hogan, K. A., Mayer, L. A., Hatfield, R. G., Albert, S., Marcott, S., Fallon, S., & Cheseby, M. (2019). Holocene break-up and reestablishment of the Petermann Ice Tongue, Northwest Greenland. *Quaternary Science Reviews*, 218, 322–342. <https://doi.org/10.1016/j.quascirev.2019.06.023>
- Rhodes, E. J. (2011). Optically Stimulated Luminescence Dating of Sediments over the Past 200,000 Years. *Annual Review of Earth and Planetary Sciences*, 39(1), 461–488. <https://doi.org/10.1146/annurev-earth-040610-133425>
- Rigg, G. B., & Gould, H. R. (1957). Age of Glacier Peak eruption and chronology of post-glacial peat deposits in Washington and surrounding areas. *American Journal of Science*, 255(5), 341–363. <https://doi.org/10.2475/ajs.255.5.341>

- Rippin, D. M. (2013). Bed roughness beneath the Greenland ice sheet. *Journal of Glaciology*, 59(216), 724–732. <https://doi.org/10.3189/2013JoG12J212>
- Riverman, K. L., Anandakrishnan, S., Alley, R. B., Holschuh, N., Dow, C. F., Muto, A., Parizek, B. R., Christianson, K., & Peters, L. E. (2019). Wet subglacial bedforms of the NE Greenland Ice Stream shear margins. *Annals of Glaciology*, 60(80), 91–99. <https://doi.org/10.1017/aog.2019.43>
- Robel, A. A., Pegler, S. S., Catania, G., Felikson, D., & Simkins, L. M. (2022). Ambiguous stability of glaciers at bed peaks. *Journal of Glaciology*, 68(272), 1177–1184. <https://doi.org/10.1017/jog.2022.31>
- Robel, A. A., Seroussi, H., & Roe, G. H. (2019). Marine ice sheet instability amplifies and skews uncertainty in projections of future sea-level rise. *Proceedings of the National Academy of Sciences*, 116(30), 14887–14892. <https://doi.org/10.1073/pnas.1904822116>
- Roberts, M. L., Elder, K. L., Jenkins, W. J., Gagnon, A. R., Xu, L., Hlavenka, J. D., & Longworth, B. E. (2019). ¹⁴C Blank Corrections for 25–100 µg Samples at the National Ocean Sciences AMS Laboratory. *Radiocarbon*, 61(5), 1403–1411. <https://doi.org/10.1017/RDC.2019.74>
- Rosenbaum, J. G. (2005). Magnetic properties of sediments in cores BL96-1,-2, and-3 from Bear Lake, Utah and Idaho. *US Geological Survey Open-File Report, 2005(1203)*, 13p.
- Rosenheim, B. E., Santoro, J. A., Gunter, M., & Domack, E. W. (2013). Improving Antarctic Sediment 14C Dating Using Ramped Pyrolysis: An Example from the Hugo Island Trough. *Radiocarbon*, 55(1), 115–126. https://doi.org/10.2458/azu_js_rc.v55i1.16234
- Rothwell, R. G., & Croudace, I. W. (2015). Twenty Years of XRF Core Scanning Marine Sediments: What Do Geochemical Proxies Tell Us? In I. W. Croudace & R. G. Rothwell (Eds.), *Micro-XRF Studies of Sediment Cores: Applications of a non-destructive tool for the environmental sciences* (pp. 25–102). Springer Netherlands. https://doi.org/10.1007/978-94-017-9849-5_2
- Schoof, C. G., & Clarke, G. K. C. (2008). A model for spiral flows in basal ice and the formation of subglacial flutes based on a Reiner-Rivlin rheology for glacial ice. *Journal of Geophysical Research*, 113(B5), B05204. <https://doi.org/10.1029/2007JB004957>
- Seguinot, J., Khroulev, C., Rogozhina, I., Stroeven, A. P., & Zhang, Q. (2014). The effect of climate forcing on numerical simulations of the Cordilleran ice sheet at the Last Glacial Maximum. *The Cryosphere*, 8(3), 1087–1103. <https://doi.org/10.5194/tc-8-1087-2014>
- Seguinot, J., Rogozhina, I., Stroeven, A. P., Margold, M., & Kleman, J. (2016). Numerical simulations of the Cordilleran ice sheet through the last glacial cycle. *The Cryosphere*, 10(2), 639–664. <https://doi.org/10.5194/tc-10-639-2016>
- Sengupta, S. (2017). *Introduction to Sedimentology* (1st ed.). Routledge. <https://doi.org/10.1201/9780203749883>
- Sergienko, O. V., & Wingham, D. J. (2019). Grounding line stability in a regime of low driving and basal stresses. *Journal of Glaciology*, 65(253), 833–849. <https://doi.org/10.1017/jog.2019.53>

- Seroussi, H., Nakayama, Y., Larour, E., Menemenlis, D., Morlighem, M., Rignot, E., & Khazendar, A. (2017). Continued retreat of Thwaites Glacier, West Antarctica, controlled by bed topography and ocean circulation. *Geophysical Research Letters*, *44*(12), 6191–6199. <https://doi.org/10.1002/2017GL072910>
- Shaw, J., Kvill, D., & Rains, B. (1989). Drumlins and catastrophic subglacial floods. *Sedimentary Geology*, *62*(2–4), 177–202. [https://doi.org/10.1016/0037-0738\(89\)90114-0](https://doi.org/10.1016/0037-0738(89)90114-0)
- Sherrod, B. L., Blakely, R. J., Weaver, C. S., Kelsey, H. M., Barnett, E., Liberty, L., Meagher, K. L., & Pape, K. (2008). Finding concealed active faults: Extending the southern Whidbey Island fault across the Puget Lowland, Washington. *Journal of Geophysical Research*, *113*(B5), B05313. <https://doi.org/10.1029/2007JB005060>
- Shugar, D. H., Walker, I. J., Lian, O. B., Eamer, J. B. R., Neudorf, C., McLaren, D., & Fedje, D. (2014). Post-glacial sea-level change along the Pacific coast of North America. *Quaternary Science Reviews*, *97*, 170–192. <https://doi.org/10.1016/j.quascirev.2014.05.022>
- Simkins, L. M., Anderson, J. B., & Demet, B. P. (2017). Grounding line processes of the southern Cordilleran Ice Sheet in the Puget Lowland. In R. A. Haugerud & H. M. Kelsey, *From the Puget Lowland to East of the Cascade Range* _{title>Geologic Excursions in the Pacific Northwest}. Geological Society of America. [https://doi.org/10.1130/2017.0049\(03\)](https://doi.org/10.1130/2017.0049(03))
- Simkins, L. M., Greenwood, S. L., & Anderson, J. B. (2018). Diagnosing ice sheet grounding line stability from landform morphology. *The Cryosphere*, *12*(8), 2707–2726. <https://doi.org/10.5194/tc-12-2707-2018>
- Spagnolo, M., Bartholomaeus, T. C., Clark, C. D., Stokes, C. R., Atkinson, N., Dowdeswell, J. A., Ely, J. C., Graham, A. G. C., Hogan, K. A., King, E. C., Larter, R. D., Livingstone, S. J., & Pritchard, H. D. (2017). The periodic topography of ice stream beds: Insights from the Fourier spectra of mega-scale glacial lineations: Periodic Topography of Ice Stream Beds. *Journal of Geophysical Research: Earth Surface*, *122*(7), 1355–1373. <https://doi.org/10.1002/2016JF004154>
- Spagnolo, M., Clark, C. D., Ely, J. C., Stokes, C. R., Anderson, J. B., Andreassen, K., Graham, A. G. C., & King, E. C. (2014). Size, shape and spatial arrangement of mega-scale glacial lineations from a large and diverse dataset: MEGA SCALE GLACIAL LINEATIONS METRICS. *Earth Surface Processes and Landforms*, n/a-n/a. <https://doi.org/10.1002/esp.3532>
- Spagnolo, M., Clark, C. D., & Hughes, A. L. C. (2012). Drumlin relief. *Geomorphology*, *153–154*, 179–191. <https://doi.org/10.1016/j.geomorph.2012.02.023>
- Spagnolo, M., Clark, C. D., Hughes, A. L. C., & Dunlop, P. (2011). The topography of drumlins; assessing their long profile shape. *Earth Surface Processes and Landforms*, *36*(6), 790–804. <https://doi.org/10.1002/esp.2107>
- Spagnolo, M., Clark, C. D., Hughes, A. L. C., Dunlop, P., & Stokes, C. R. (2010). The planar shape of drumlins. *Sedimentary Geology*, *232*(3–4), 119–129. <https://doi.org/10.1016/j.sedgeo.2010.01.008>

- Stokes, C. R., & Clark, C. D. (2001). Palaeo-ice streams. *Quaternary Science Reviews*, 20(13), 1437–1457. [https://doi.org/10.1016/S0277-3791\(01\)00003-8](https://doi.org/10.1016/S0277-3791(01)00003-8)
- Stokes, C. R., & Clark, C. D. (2002). Are long subglacial bedforms indicative of fast ice flow? *Boreas*, 31(3), 239–249. <https://doi.org/10.1080/030094802760260355>
- Stokes, C. R., & Clark, C. D. (2003). The Dubawnt Lake palaeo-ice stream: evidence for dynamic ice sheet behaviour on the Canadian Shield and insights regarding the controls on ice-stream location and vigour. *Boreas*, 32(1), 263–279. <https://doi.org/10.1111/j.1502-3885.2003.tb01442.x>
- Stokes, C. R., Spagnolo, M., Clark, C. D., Ó Cofaigh, C., Lian, O. B., & Dunstone, R. B. (2013). Formation of mega-scale glacial lineations on the Dubawnt Lake Ice Stream bed: 1. size, shape and spacing from a large remote sensing dataset. *Quaternary Science Reviews*, 77, 190–209. <https://doi.org/10.1016/j.quascirev.2013.06.003>
- Stuiver, M. (1980). Workshop On ¹⁴C Data Reporting. *Radiocarbon*, 22(3), 964–966. <https://doi.org/10.1017/S0033822200010389>
- Stuiver, M., & Polach, H. A. (1977). Discussion Reporting of ¹⁴C Data. *Radiocarbon*, 19(3), 355–363. <https://doi.org/10.1017/S0033822200003672>
- Swanson, T. W., & Caffee, M. L. (2001). Determination of ³⁶Cl Production Rates Derived from the Well-Dated Deglaciation Surfaces of Whidbey and Fidalgo Islands, Washington. *Quaternary Research*, 56(3), 366–382. <https://doi.org/10.1006/qres.2001.2278>
- Taglı, S., & Jenness, J. (2008). *GIS-based automated landform classification and topographic, landcover and geologic attributes of landforms around the Yazoren Polje, Turkey*. <http://dspace.balikesir.edu.tr/xmlui/handle/20.500.12462/9638>
- Thompson, R., & Oldfield, F. (1986). *Environmental Magnetism*. London, Allen & Unwin.
- Thorson, R. M. (1980). Ice-Sheet Glaciation of the Puget Lowland, Washington, during the Vashon Stade (Late Pleistocene)1. *Quaternary Research*, 13(3), 303–321. [https://doi.org/10.1016/0033-5894\(80\)90059-9](https://doi.org/10.1016/0033-5894(80)90059-9)
- Thorson, R.M. (1981). Isostatic effects of the last glaciation in the Puget lowland, Washington. U.S. Geological Survey Open-File Report, 81-370, 100.
- Tulaczyk, S., Kamb, W. B., & Engelhardt, H. F. (2000). Basal mechanics of Ice Stream B, west Antarctica: 1. Till mechanics. *Journal of Geophysical Research: Solid Earth*, 105(B1), 463–481. <https://doi.org/10.1029/1999JB900329>
- United States Geological Survey (USGS). (1999). 7.5 minute Digital Elevation Model (10 meter resolution) [data file]. Retrieved from [https:// apps.nationalmap.gov/viewer/](https://apps.nationalmap.gov/viewer/)
- Vaughan, D.G., J.C. Comiso, I. Allison, J. Carrasco, G. Kaser, R. Kwok, P. Mote, T. Murray, F. Paul, J. Ren, E. Rignot, O. Solomina, K. Steffen and T. Zhang. (2013). Observations: Cryosphere. In: *Climate Change, 2013: The Physical Science Basis*. Contribution of Working Group I to the Fifth Assessment Report of the Intergovernmental Panel on Climate Change [Stocker, T.F., D. Qin, G.-K. Plattner, M. Tignor, S.K. Allen, J. Boschung, A. Nauels, Y. Xia, V. Bex and P.M. Midgley (eds.)]. Cambridge University Press, Cambridge, United Kingdom and New York, NY, USA.

- Verosub, K. L., & Roberts, A. P. (1995). Environmental magnetism: Past, present, and future. *Journal of Geophysical Research: Solid Earth*, *100*(B2), 2175–2192. <https://doi.org/10.1029/94JB02713>
- Waitt Jr., R.B., & Thorson, R.M. (1983). The Cordilleran ice sheet in Washington, Idaho, and Montana. Late-quaternary environments of the United States, 1, 53-70.
- Wallinga, J., & Cunningham, A. C. (2015). Luminescence dating, uncertainties and age range. *Encyclopedia of Scientific Dating Methods*, 440–445. https://doi.org/10.1007/978-94-007-6304-3_197
- Wallinga, J., S. Murray, A., & Btter-Jensen, L. (2002). Measurement of the Dose in Quartz in the Presence of Feldspar Contamination. *Radiation Protection Dosimetry*, *101*(1), 367–370. <https://doi.org/10.1093/oxfordjournals.rpd.a006003>
- Wang, S., Wu, Q., & Ward, D. (2017). Automated delineation and characterization of drumlins using a localized contour tree approach. *International Journal of Applied Earth Observation and Geoinformation*, *62*, 144–156. <https://doi.org/10.1016/j.jag.2017.06.006>
- Weertman, J. (1957). On the Sliding of Glaciers. *Journal of Glaciology*, *3*(21), 33–38. <https://doi.org/10.3189/S0022143000024709>
- Weertman, J. (1974). Stability of the Junction of an Ice Sheet and an Ice Shelf. *Journal of Glaciology*, *13*(67), 3–11. <https://doi.org/10.3189/S0022143000023327>
- Weidick, A. (1988). Surging glaciers in Greenland – a status. *Rapport Grønlands Geologiske Undersøgelse*, *140*, 106–110. <https://doi.org/10.34194/rapgg.u.v140.8047>
- Weiss, A.D. (2001) Topographic Position and Landforms Analysis. In Poster Presentation, ESRI User Conference, San Diego, CA (Vol. 200), accessible online at http://www.jennessent.com/downloads/TPI-poster-TNC_18x22.pdf
- Wellner, J. S., Lowe, A. L., Shipp, S. S., & Anderson, J. B. (2001). Distribution of glacial geomorphic features on the Antarctic continental shelf and correlation with substrate: implications for ice behavior. *Journal of Glaciology*, *47*(158), 397–411. <https://doi.org/10.3189/172756501781832043>
- Whillans, I. M., & Van Der Veen, C. J. (1997). The role of lateral drag in the dynamics of Ice Stream B, Antarctica. *Journal of Glaciology*, *43*(144), 231–237. <https://doi.org/10.3189/S0022143000003178>
- Whitehouse, P. L., Gomez, N., King, M. A., & Wiens, D. A. (2019). Solid Earth change and the evolution of the Antarctic Ice Sheet. *Nature Communications*, *10*(1), 503. <https://doi.org/10.1038/s41467-018-08068-y>
- Winsborrow, M. C. M., Clark, C. D., & Stokes, C. R. (2010). What controls the location of ice streams? *Earth-Science Reviews*, *103*(1–2), 45–59. <https://doi.org/10.1016/j.earscirev.2010.07.003>
- Wintle, A. G., & Murray, A. S. (2006). A review of quartz optically stimulated luminescence characteristics and their relevance in single-aliquot regeneration dating protocols. *Radiation Measurements*, *41*(4), 369–391. <https://doi.org/10.1016/j.radmeas.2005.11.001>

Wright, W. B. (1912). III.—The Drumlin Topography of South Donegal. *Geological Magazine*, 9(4), 153–159. <https://doi.org/10.1017/S0016756800114141>

Yokoyama, Y., & Purcell, A. (2021). On the geophysical processes impacting palaeo-sea-level observations. *Geoscience Letters*, 8(1), 13. <https://doi.org/10.1186/s40562-021-00184-w>

Zoet, L. K., Rawling, J. E., Woodard, J. B., Barrette, N., & Mickelson, D. M. (2021). Factors that contribute to the elongation of drumlins beneath the Green Bay Lobe, Laurentide Ice Sheet. *Earth Surface Processes and Landforms*, 46(13), 2540–2550. <https://doi.org/10.1002/esp.5192>